RHIC Beam Use Request
For Runs 16 and 17

The STAR Collaboration

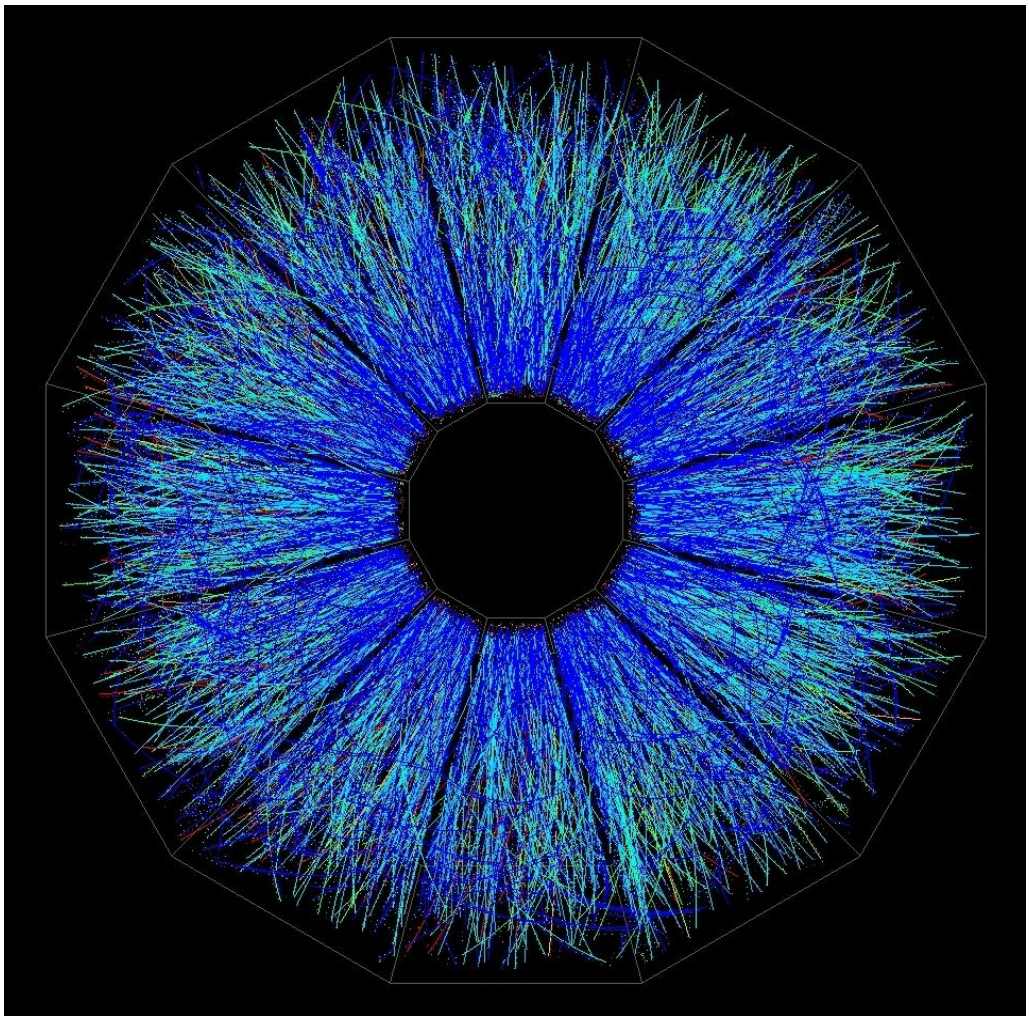

May 19, 2015

1 Executive Summary

The STAR Collaboration makes the following two-year beam-use proposal, in order to achieve its spin and relativistic heavy ion physics goals on a timescale consistent with intense international interest and competition in these areas, as well as to utilize RHIC beams effectively, taking full advantage of recent improvements in machine and detector capability.

Run	Energy	Duration	System	Goals	priority	Sequence
16	$\sqrt{s_{NN}}$=200 GeV	13-wk	Au+Au	Λ_c, D v_2, R_{AA}, Υ R_{AA} 10nb^{-1}, 2billion MB	1	1
	$\sqrt{s_{NN}}$=62 GeV	4-wk	Au+Au	1.5B MB (1B w/ HFT)	4	2
	$\sqrt{s_{NN}}$=19.6 GeV	1-wk	d+Au	100M MB	4	3
17	$\sqrt{s}$ = 510 GeV	11 wk	Transverse p+p	A_N of $W^{\pm}$, γ, Drell-Yan, $\mathcal{L}$=360 pb^{-1}, 55% pol	2	1
	$\sqrt{s_{NN}}$=19.6 GeV	1-wk	p+p	400M MB	4	2
	$\sqrt{s_{NN}}$ =200 GeV	3-wk	Ru+Ru	1.2billion MB	3	3
	$\sqrt{s_{NN}}$=200 GeV	3-wk	Zr+Zr	1.2billion MB	3	4

Table 1-1: Scenario I-A: 22 cryoweeks for Run 17 with Isobar sources (Zr, Ru). We assume most of the TPC bandwidth (1800Hz) is for the minbias event rate for isobar data-taking with 90 hours per week of DAQ time. For Au+Au at 62 GeV, the driving factor of the required weeks is 1 billion minbias events within the HFT vertex cut with maximum of 700Hz delivered by the available luminosity. All luminosities requested are actual sampled luminosity. See text for details of HFT and pp510 run conditions and optimizations.

STAR's top scientific priority is to capitalize on the existing investments in the Heavy Flavor Tracker (HFT) and Muon Telescope Detector (MTD) in run 16. The HFT and MTD were installed prior to run 14 and successfully operated in runs 14 and 15. We request 13 weeks of Au+Au collsions at $\sqrt{s_{NN}}$ = 200 GeV in run 16 to collect rare triggers for Upsilon states, gamma-jet correlations, B→ J/ψ and J/ψ production, as well as 2 billion minbias events for Λ_c and differential studies of charm flow and correlations. The combination of the run 14 and 16 data will allow for measurements of each of the three Upsilon states. The heavy flavor and quarkonium programs are of high priority for fulfilling STAR's scientific program with the HFT and MTD upgrades before Phase II of the Beam Energy Scan (BES II).

STAR's second highest scientific priority is the first significant measurement of the sign change of the Sivers' function, when compared to the value measured in SIDIS, and evolution effects in transverse momentum distributions through measurements of single spin asymmetries in $W^{+/-}$, Z, direct photon and Drell-Yan production in transversely polarized $\sqrt{s}$ = 500 GeV p+p collisions. The sign change measurement is a fundamental test of QCD and is being pursued by other experiments, making a timely measurement imperative.

STAR's third scientific priority is to clarify the interpretation of the observed signatures of the chiral magnetic effect, chiral magnetic wave and chiral vortical effect by making measurements that disentangle signal from background v_2 effects. We request a 3 week run each for Ruthenium-96 (Ru+Ru) and Zirconium-96 (Zr+Zr) collisions in run 17. This choice of nuclei is ideal as it allows for a variation in magnetic field at a maximum of 10%, while keeping nearly all other parameters the same. This decisive measurement of the ratio of charge separation in the isobar reduces the flow background dramatically, and will greatly advance our understanding of the chiral magnetic effect, which has fundamental impact beyond the field of high-temperature QCD. The availability of the Ru-96 source precludes running this program as part of run 16 and uncertainty remains also for run 17. If this source cannot be secured in time, STAR proposes the 22-cryoweek scenario in Table 1-2. In the case that only 15 cryoweeks are available in run 17, STAR proposes the scenario given in Table 1-3.

Run	Energy	Duration	System	Goals	priority	Sequence
16	$\sqrt{s_{NN}}$=200 GeV	13-wk	Au+Au	Λ_c, D v_2, R_{AA}, Υ R_{AA} 10nb^{-1}, 2billion MB	1	1
	$\sqrt{s_{NN}}$=62 GeV	5-wk	Au+Au	1.5B MB, HT	4	2
17	$\sqrt{s_{NN}}$=510 GeV	12-wk	Transverse p+p	A_N of $W^{\pm}$, γ, Drell-Yan, $\mathcal{L}$=400 pb^{-1}, 55% pol	2	1
	$\sqrt{s_{NN}}$ = 14.5	1-wk	d+Au	80M MB	4	5
	$\sqrt{s_{NN}}$ = 19.6	1-wk	d+Au	100M MB	4	4
	$\sqrt{s_{NN}}$ = 39.0	1-wk	d+Au	400M MB	4	3
	$\sqrt{s}$ = 19.6	1-wk	p+p	400M MB	4	2

Table 1-2: Scenario I-B: 22 cryoweeks for Run 17 without Isobar (Ru-96 source)

Our next scientific priority is to take data at beam energies that are lower than the nominal energies, but are not part of STAR's proposed Beam-Energy-Scan Phase-II program. There are two programs in our requests in this category:

a) Au+Au collisions at 62 GeV for measurements of inclusive jets and charm spectrum at low energy. With newly developed analysis techniques, inclusive jet measurements are possible with minimum-bias data in Au+Au collisions. We have recently extended the measurement to Au+Au at 62 GeV with limited statistics from run 10. We request 4 (5) weeks of Au+Au collisions at this energy for an inclusive jet R_{CP} measurement. This will also provide a measurement of D^0 spectrum from HFT.

b) d+Au and p+p collisions at low energies for study of onset of high-p_T hadron nuclear modification due to jet quenching. STAR has produced a systematic measurement of R_{CP} of inclusive hadrons as a function of momentum from all the beam energies taken at RHIC. The data has shown a systematic increase of R_{CP} from less than unity to significantly above unity when the beam energy varies from top energy of 200 GeV to 7.7 GeV. A combination

of d+Au collisions and p+p collisions at energies where R_{CP} is around unity will help us address the onset of final-state hadron suppression.

Run	Energy	Duration	System	Goals	priority	Sequence
16	$\sqrt{s_{NN}}$=200 GeV	13-wk	Au+Au	Λ_c, D v_2, R_{AA}, Υ R_{AA} 10nb^{-1}, 2billion MB	1	1
	$\sqrt{s_{NN}}$=62 GeV	4-wk	Au+Au	1.5B MB, HT	4	2
	$\sqrt{s_{NN}}$=19.6 GeV	1-wk	d+Au	100M MB	4	3
17	$\sqrt{s}$=510 GeV	11-wk	Transverse p+p	A_N of $W^{\pm}$, γ, Drell-Yan, $\mathcal{L}$=360 pb^{-1}, 55% pol	2	2
	$\sqrt{s_{NN}}$=19.6 GeV	1-wk	p+p	400M MB	4	1

Table 1-3: Scenario II: 15 cryoweeks for Run 17 (assume Isobar sources not possible in run16)

The STAR Collaboration presents in this BUR five compelling and prioritized scientific programs for the 2016 and 2017 RHIC runs, prior to the start of BES-II [1]. Taking into account uncertainty in the availability of the Ru-96 source and the duration of run 17, we present three running scenarios (Tables 1-1 through 1-3). In each scenario, the data requirements for STAR's two top priority scientific goals will be met. In no scenario can all the data needs for all programs be met in runs 16 and 17, and STAR may thus propose to return to the data taking for these programs concurrent with that for BES-II. In this BUR we furthermore discuss the highlights from the scientific publications, on-going analyses and detector performance from recent runs. We also outline the planned upgrades in the next few years in preparation for Run 17 and the Beam Energy Scan II.

2 Highlights from STAR Science Programs

2.1 STAR Heavy Ion Program

STAR has launched a comprehensive heavy-flavor program with the two newly installed novel detectors: the Heavy-Flavor Tracker (HFT) for open heavy-flavor measurements and the Muon Telescope Detector (MTD) for quarkonium measurements. While data taken with these systems in run 14 is being processed STAR continues to successfully run, accumulate additional data and anticipate exciting new results from these detectors. We have published four papers since the last PAC meeting on Observation of D^0 meson nuclear modifications in Au+Au collisions using TPC and TOF [2], shown in Figure 2-1, J/ψ production at low pT in Au+Au and Cu+Cu collisions[3], J/ψ polarization in p+p collisions at 200 GeV[4] and Suppression of Upsilon Production in d+Au and Au+Au Collisions at 200 GeV[5]. The quarkonium measurements have used a combination of triggers and electron identification from barrel EMC, TPC and TOF.

Dileptons are crucial probes for studying the properties of the strongly interacting, hot and dense matter, which is created in ultra-relativistic heavy-ion collisions at the Relativistic Heavy-Ion Collider (RHIC). STAR has continued to explore how dilepton measurements can be used as a sensitive probe of chiral symmetry restoration effects. STAR has been very fruitful in presenting and publishing the dilepton results in the last two years. Two papers have been published on dielectron mass spectra and anisotropic flow in Au+Au collisions at 200GeV[6,7], and three new submissions on the Energy dependence of acceptance-corrected dielectron excess mass spectrum at mid-rapidity in Au+Au collisions at 19.6 and 200GeV[8] (shown in Figure 2-2), on Leptonic decay of the phi(1020) meson in Au+Au collisions at 200 GeV[9] (Figure 2-3), and a detailed paper on dielectron production in different centrality and p_T bins[10] (Figure 2-4). New studies show that there is a consistent dielectron excess from 200 down to 19.6 GeV, in agreement with SPS results. The excess yields at low mass range are consistent with a continuous thermal radiation from the entire lifetime of the hot and dense matter. Studies of the phi meson show no significant difference in the reconstructed phi(1020) p_T spectrum, dN/dy , or $< p_T >$ between the leptonic and hadronic decay channels.

We have presented several results in recent papers on small-system collisions and the study of hadron correlations in d+Au collisions[11,12,13]. Di-hadron correlations with particle identified leading hadrons show that No statistically significant ridge is found associated with either pion or non-pion trigger type in minimum bias d+Au data [11]. We have carried out a detailed study of the effects of the event selection in jet-like correlation measurements in d+Au collisions, and conclude that the jetlike correlated yield increases with the event multiplicity [12]. After taking into account this dependence, the non-jet contribution on the away side is minimal, leaving little room for a back-to-back ridge in these collisions. On the other hand, a finite correlated yield is observed at large relative pseudorapidity on the near side. This correlated yield as a function of eta appears to scale with the dominant, primarily jet-related, away-side yield. The Fourier coefficients of the $d\phi$ correlation (Vn), have a strong $d\eta$ dependence [13] (shown in Figure 2-5).

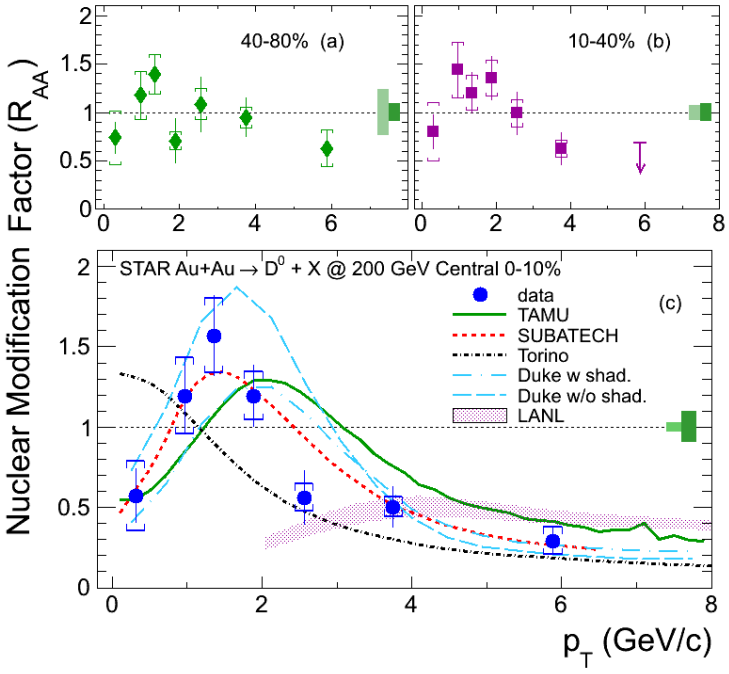

Figure 2-1 Panels (a,b): D^0 RAA for peripheral 40%–80% and semicentral 10%–40% collisions. Panel (c): D^0 RAA for 0%–10% most-central events (blue circles) compared with model calculations from the TAMU (solid curve), SUBATECH (dashed curve), Torino (dot-dashed curve), Duke (long-dashed and long-dot-dashed curves), and LANL groups (filled band). The vertical lines and boxes around the data points denote the statistical and systematic uncertainties. The vertical bars around unity denote the overall normalization uncertainties in the Au+Au and p+p data, respectively.

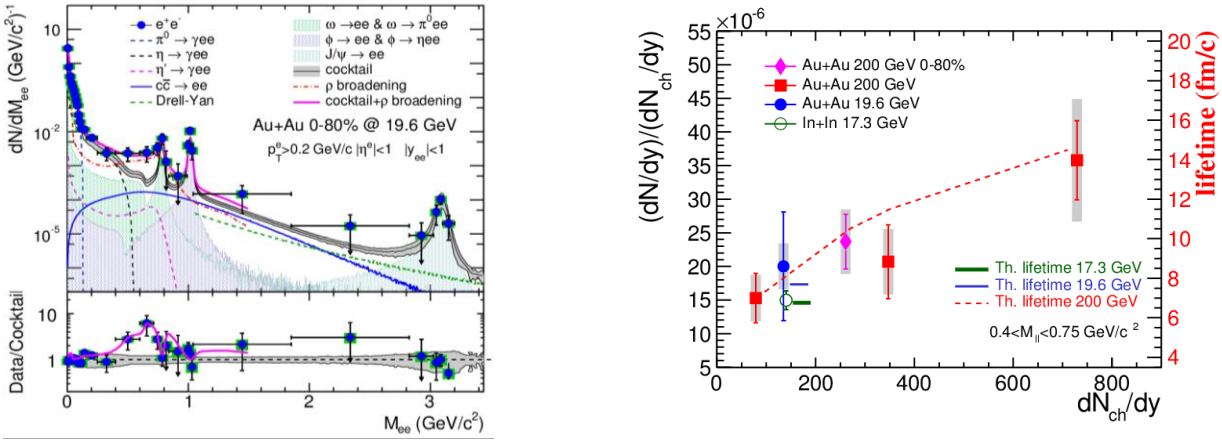

Figure 2-2 Left: Dielectron invariant mass spectrum in STAR after efficiency corrections, compared with the hadronic cocktail consisting of the decays and correlated decays of charm in Au+Au collisions at 19.6GeV. The data to cocktail ratio is shown in the bottom panel. Theoretical calculations of a broadened rho spectral function are shown up to 1.5 GeV/c2 for comparison. Systematic uncertainties for the data points are shown as green boxes, and the grey band represents the uncertainties for the cocktail simulation. Right: Integrated yields of the normalized dilepton excesses for $0.4 < M_{ll} < 0.75$ GeV/c2 as a function of dNch/dy. The solid circle and diamond represent the results in 0-80% Au+Au collisions at 19.6 and 200GeV, respectively. The squares are the results for 40-80%, 10-40%, and 0-10% Au+Au at 200 GeV. The open circle represents the dimuon result from the NA60 measurement with dNch/deta > 30. Bars are statistical uncertainties, and systematic uncertainties are shown as grey boxes. The theoretical lifetimes for 200 GeV Au+Au as a function of dNch/dy in the model calculations are shown as a dashed curve. The lifetimes for 17.3 GeV In+In and 19.6 GeV Au+Au in the same model calculations are shown as the two horizontal bars. The dNch/dy values for the horizontal bars are shifted for clarity.

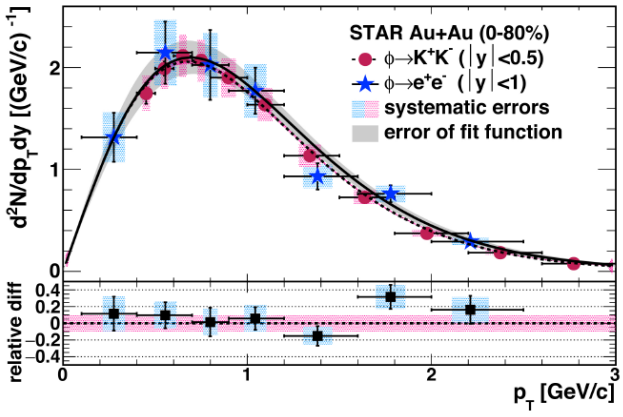

Figure 2-3 The corrected phi(1020) →e^+e^- (blue star) and phi(1020) →K^+K^- (red circle) yields for the 0-80% centrality events from Au + Au collisions at 200GeV. The vertical bars are statistical errors and the boxes are systematic uncertainties. Systematic errors for the K^+K^- channel are fixed at 10% for all p_T. The dashed and solid lines are m_T-exponential fit functions to the hadronic and leptonic decay channel results, respectively. The gray band represents errors of the fit function to the leptonic result. Data are plotted at the mean p_T in each p_T bin estimated from the fit function.

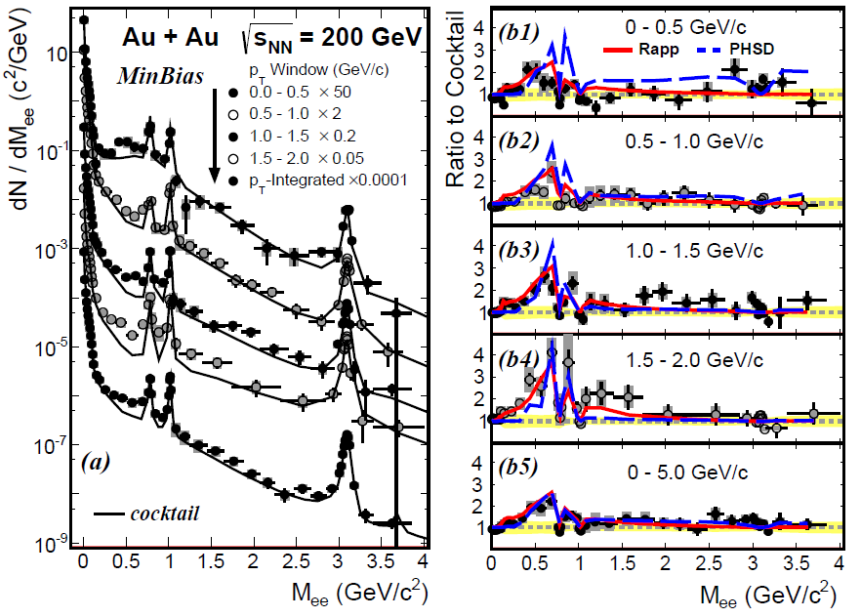

Figure 2-4 Left panel: Invariant mass spectra from $\sqrt{s_{NN}}$ = 200GeV Au+Au minimum-bias collisions in different p_T ranges. The solid curves represent the cocktail of hadronic sources and include the charm-decayed dielectron contribution calculated by Pythia scaled by N_{bin}. Right panels: The ratio of dielectron yield over cocktail for different p_T bins, and the comparison with model calculations. The gray boxes show the systematic uncertainties of the data. Yellow bands depict systematic uncertainties on the cocktail.

Searches for the quantum chromodynamics (QCD) critical point were performed by STAR, using higher moments of net-charge multiplicity[14], net-proton yields, and dynamical fluctuations of unlike particle pairs[15]. Details of these results and preliminary results are presented in a separate section on Beam Energy Scan. In addition, event-by-event fluctuations of the ratio of inclusive charged hadrons to photon multiplicities at forward rapidity in Au+Au collisions using the Forward TPC and Photon Multiplicity Detector (PMD) have been studied [16]. The dominant contribution to such fluctuations is expected to come from correlated production of charged and neutral pions. We search for evidences of dynamical fluctuations of different physical origins. A non-zero statistically significant signal of dynamical fluctuations is observed in excess to the model prediction when charged particles and photons are measured in the same acceptance, shown in Figure 2-6. We find that, unlike dynamical net-charge fluctuation, charge-neutral fluctuation is not dominated by correlation due to particle decay.

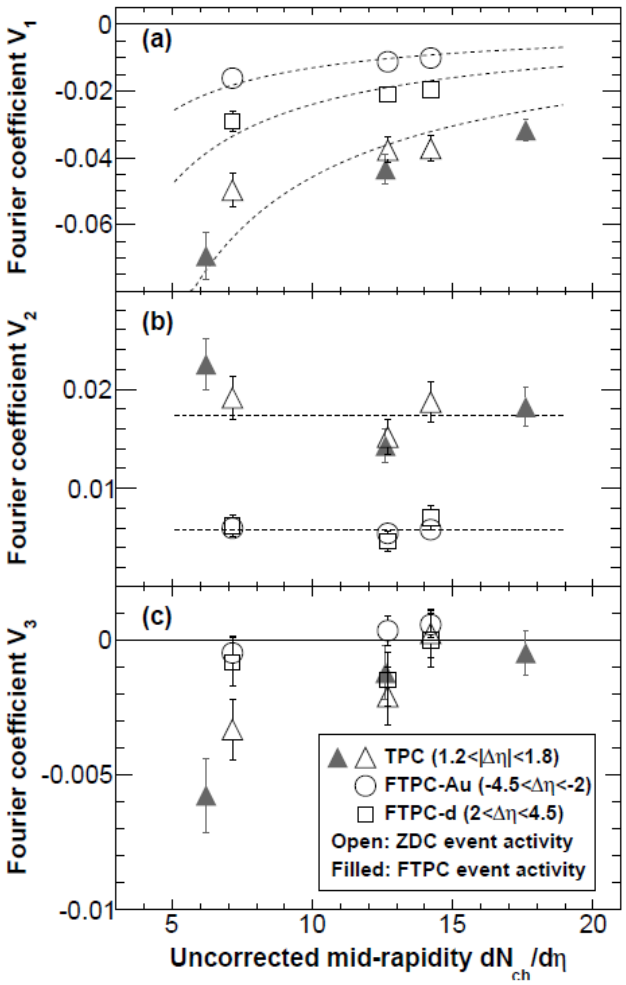

Figure 2-5 Fourier coefficients (a) V_1, (b) V_2, and (c) V_3 versus the measured mid-rapidity charged particle $dN_{ch}/deta$. Event activity selections by both ZDC-Au and FTPC-Au are shown. Trigger particles are from TPC, and associated particles from TPC (triangles), FTPC-Au (circles), and FTPC-d (squares), respectively. Systematic uncertainties are estimated to be10% on V_1 and V_2, and smaller than statistical errors for V_3. Errors shown are the quadratic sum of statistical and systematic errors. The dashed curves are to guide the eye.

The STAR Collaboration published in Physical Review Letters [17], the first high statistics measurement of the ΛΛ correlation function in Au+Au collisions at $\sqrt{s_{NN}}$ = 200 GeV and it is also highlighted as PRL editors' suggestion. This research pioneered the venue of using RHIC as a hyperon factory to investigate hyperon-hyperon interactions. The STAR measurement can provide precious data for the understanding of hyperon-hyperon interaction which is an important input to various baryon-baryon interaction potential models as well as for the study of equation of state for neutron stars. The ΛΛ interaction is also closely related to the existence of the H dibaryon, one of the most searched for exotic hadrons in nuclear collisions. The Lednicky and Lyuboshitz analytical model is used to fit the experimental correlation function and the resulting parameters suggest that the strength of the ΛΛ interaction is weak, shown in Figure 2-7. The measured ΛΛ correlation shows deviation from unity as well as the free correlation expected from Fermi statistics. The correlation measurement also allowed extraction of an upper limit for possible production of the H dibaryon in Au+Au collisions at 200 GeV, which is significantly lower than theoretical predictions based on coalescence calculations.

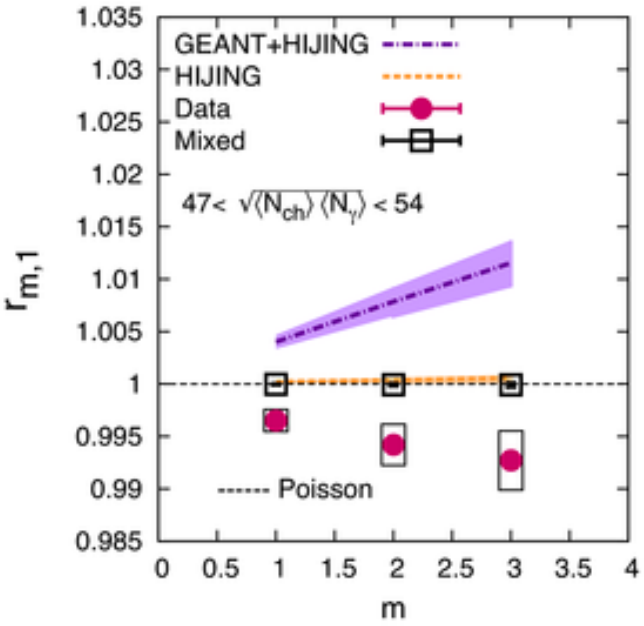

Figure 2-6 The moments for real and mixed events as a function of order m in a fixed multiplicity bin of 47<sqrt(N_{ch}/ Nγ)<54. hijing, hijing+geant results are represented by curves. For data the statistical uncertainties are shown by vertical lines and the systematic uncertainties are shown by boxes. For model curves statistical uncertainties are shown by bands.

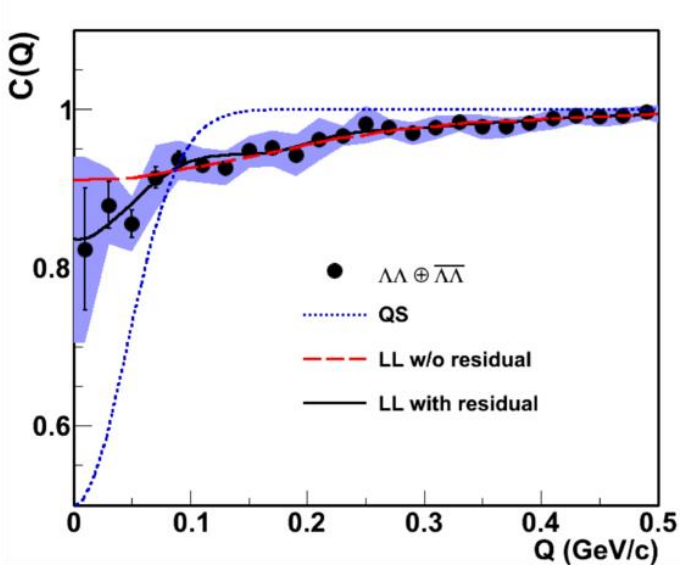

Figure 2-7 The combined ΛΛ and anti-Λ anti-Λ correlation function for 0-80% centrality Au+Au collisions at √sNN = 200 GeV. Curves correspond to fits using the Lednicky and Lyuboshitz analytical model with and without a residual correlation term. The dotted line corresponds to Fermi statistics with a source size of 3.13 fm. The shaded band corresponds to the systematic error.

2.2 STAR Spin Program

The STAR spin physics program seeks to advance our understanding of the spin and flavor structure of the proton in terms of its constituent quarks and gluons, exploiting the unique capability of RHIC to provide longitudinally and transversely polarized p+p collisions at multiple collision energies. Using longitudinally polarized beams, one can probe the helicity preferences of the gluons and up and down antiquarks, to determine the contribution of each to the total spin of the proton. With spins transverse to their momentum direction, the p+p collisions exhibit kinematic and dynamical effects that are directly sensitive to quark transversity and partonic motion within the proton. This program is complemented by studies of polarized p+p elastic scattering and central exclusive production, in which a far-forward proton is detected intact.

Since 2009 RHIC has completed several very successful polarized p+p runs both at $\sqrt{s}$ = 200 GeV and $\sqrt{s}$ = 510 GeV. The STAR recorded luminosity and the average beam polarization as measured by the H-jet polarimeter are summarized in Table 2-1. These data sets formed the basis for papers and new preliminary results, which are highlighted in the following sections.

Year	√s (GeV)	Recorded Luminosity for Transverse p+p	Recorded Luminosity for Longitudinal p+p	<P> B / Y
2009	200 500		25 pb^{-1} 10 pb^{-1}	56/55 39
2011	500	25 pb^{-1}	12 pb^{-1}	48
2012	200 510	22 pb^{-1}	 82 pb^{-1}	61/56 50/53
2013	510		300 pb^{-1}	51/52
2015	200	53 pb^{-1}	54 pb^{-1}	53/57

Table 2-1: Recorded luminosity at STAR and average beam polarization from the H-jet polarimeter.

2.2.1 Transverse Spin Program

Since the last PAC the STAR spin-working group has submitted one paper to PRL [18]. This paper reports the first Interference Fragmentation Function (IFF) analysis completed at STAR and the first transverse single spin asymmetry (A_{UT}) to ever show a significant transversity signal in hadronic collisions. This analysis, like the first Collins asymmetry measurement, was exploratory and therefore utilized the small 200 GeV transversely polarized proton data set taken in 2006. These initial IFF and Collins results motivated additional exploratory analyses in the run 2011 √s= 500 GeV dataset and further transverse running at 200 GeV. During the past year STAR has capitalized on this promising new transverse mid-rapidity program by releasing a suite of IFF, Collins and Collins-like asymmetry measurements at 200 and 500 GeV center of mass energies.

The √s = 200 GeV results shown in the left panel of Figure 2-8 display the same invariant mass and transverse momentum dependence seen in the 2006 analysis, but with significantly increased precision. These large asymmetries are also observed at √s = 500 GeV, as shown in the right panel of the same figure. In Figure 2-9 the Collins asymmetries vs. z for charged pions in jets are plotted. Kinematic cuts are set so that both the √s = 200 (blue) and 500 (red) GeV asymmetries sample approximately the same parton momentum fraction (x) and the same average pion transverse momentum with respect to the jet axis (j_T). The agreement between the 200 and 500 asymmetries suggest simple x_T scaling is driving the differences and that evolution effects may be small. The evolution of transverse momentum dependent (TMD) distributions, like the Collins and Sivers functions, is largely unknown and is a subject of vigorous debate in the hadronic spin physics community. The data in Figure 2-9 represent the first significant asymmetries sensitive in the Collins channel in hadronic collisions.

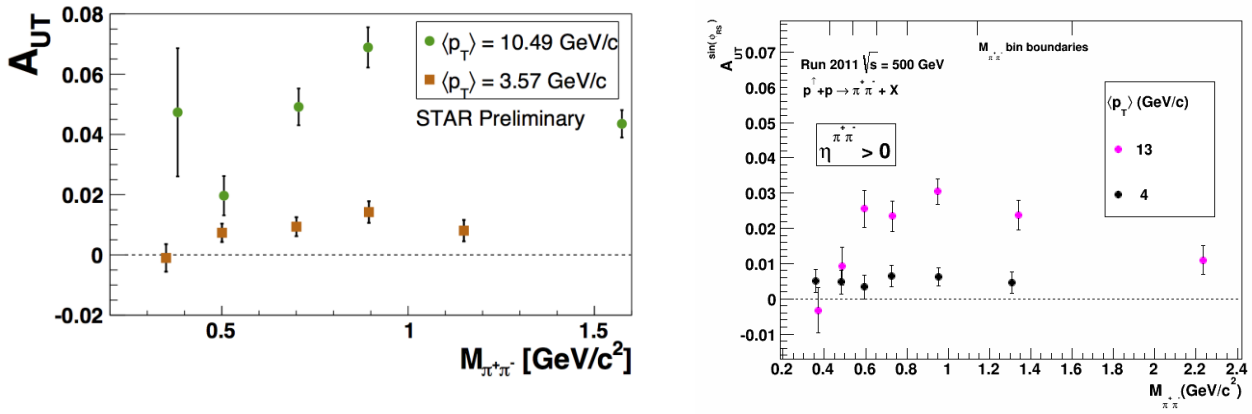

Figure 2-8 The IFF AUT at √s=200 GeV (left) and at √s=500 GeV (right) as a function of the invariant mass of the π+-π- dihadron pair. The asymmetries show the expected enhancement at the ρ mass and increase with di-hadron p_T.

STAR's ability to simultaneously measure the IFF and Collins asymmetries provides a unique opportunity to study the universality and evolution of the transversity distributions, interference and Collins fragmentation functions. Previously these distributions have been accessed only in semi-inclusive deep inelastic lepton-nucleon scattering (SIDIS) and e^+e^- scattering experiments, inviting questions of how they change when measured in hadronic collision and how they evolve with momentum transfer scales. The fact that these asymmetries are measured in the same system, at both √s = 200 and 500 GeV, will allow theorists to untangle universality and evolution effects.

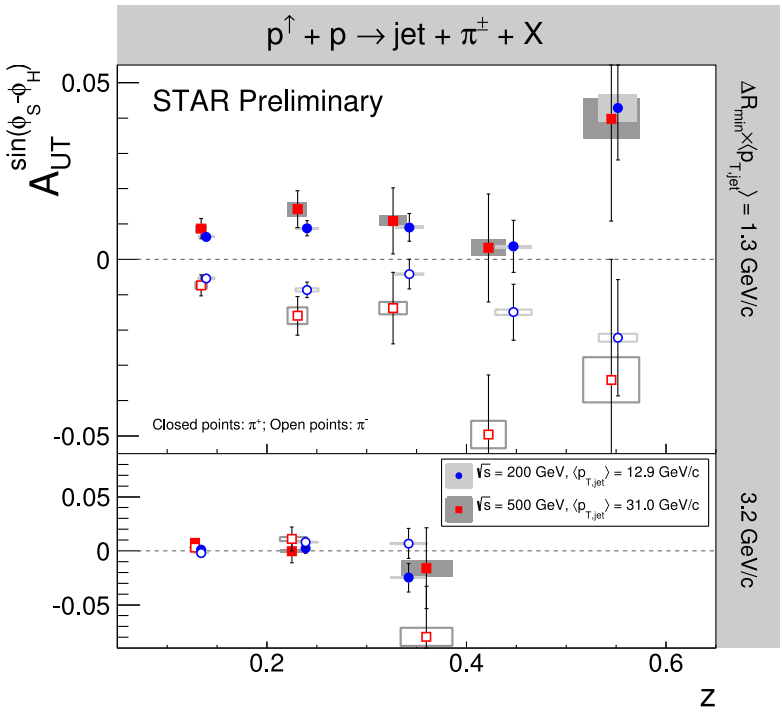

Figure 2-9 Collins A_{UT} as a function of z for √s = 200 (blue) and 500 (red) GeV p+p collisions. The jet p_T ranges have been chosen to sample the same parton x values for both beam energies. The angular cuts, characterized by the minimum distance of the charged pion from the jet thrust axis, have been chosen to sample the same jT values (~ΔR × z × p_T^{jet}). The fact the asymmetries change significantly with the average jT selected indicates a significant jT dependence. These data show for the first time a nonzero asymmetry in p+p collisions sensitive to transversity x Collins FF.

Finally, these asymmetries will provide insights into the size and nature of factorization breaking effects that are expected to affect the Collins asymmetries in hadronic collisons. In the IFF channel the transversity distributions and fragmentation functions are collinear, for which factorization is in general better understood. The Collins channel accesses the same physics from the same events, only formulated with the TMD framework needed to describe the Collins functions. This duality will allow

theorists to further study and develop the TMD framework within hadronic collisions. The transversely polarized data taken at √s=500 GeV in run 11 also provides enhanced sensitivity to lower x partons and therefore distributions such as the gluon Sivers' (via the twist-3 correlation functions) and the linearly polarized gluon Collins-like distributions. The Sivers' function, which encapsulates the correlation between the transverse motion of the partons and the spin of the parent nucleon, may be accessed via the azimuthal asymmetries of inclusive jets. These asymmetries, shown in Figure 2-10, are presented as a function of particle-jet p_T for four bins of jet η relative to the polarized beam. No large asymmetries are observed, consistent with expectation from measurements at $\sqrt{s}$ = 200 GeV [19] and model predictions [20].

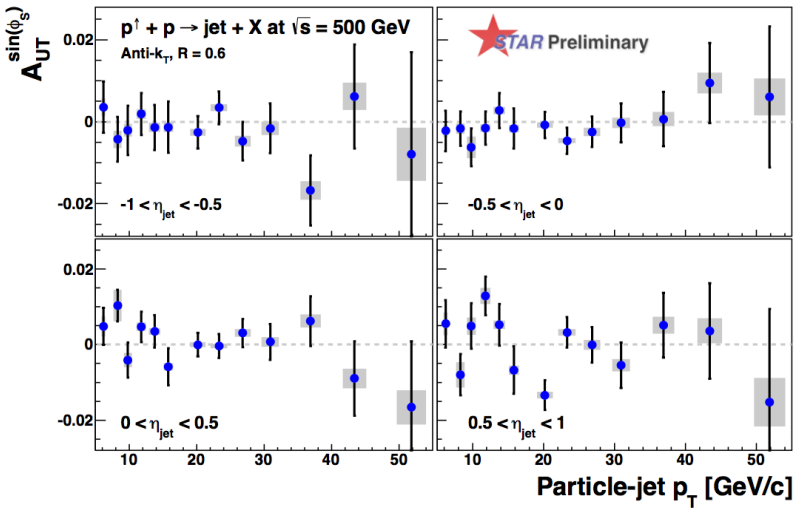

Figure 2-10: Inclusive jet azimuthal transverse single-spin asymmetries as a function of particle jet pT for four bins of jet η relative to the polarized beam. The measurements show no sign of large asymmetries and may suggest further constraints on the gluon Sivers function through the sensitivity of the twist-3 parton distribution function.

Figure 2-11 shows the "Collins-like" asymmetries as a function of z for three bins of jet p_T and two bins of jet η relative to the polarized beam. Existing model predictions are unconstrained by measurement and suggest a maximum possible upper limit of ≈ 2%. The present data fall well below this maximum with the best precision at lower values of z, where models suggest the largest effects may occur. Thus, the present data should allow for the first experimental constraints beyond the positivity bounds.

The large inclusive π^0 single spin asymmetries measured in the Forward Meson Spectrometer (FMS) at $\sqrt{s}$ = 200 GeV and 2.8 < η < 4.0 have been shown to persist at $\sqrt{s}$ = 500 GeV. Although the mechanism behind these asymmetries is unknown, the cause has often been attributed to initial state effects, such as the Sivers' function, or final state effects like the Collins function. STAR has developed the ability to reconstruct neutral "jet-like" events in the FMS, paving the way for the measurement of inclusive jet asymmetries that are sensitive to the Sivers' functions, as well as the Collins angle between the π^0 and the neutral jet axis. Figure 2-12 shows the Collins asymmetry A_{UT} as a function of z_{EM}, the fraction of the neutral jet carried by the pion. While the asymmetries lie systematically above zero, they are much smaller than the inclusive π^0 seen in Figure 2-12. Likewise, the azimuthal asymmetries of inclusive electromagnetic jets in the FMS have also been shown to be systematically suppressed compared to the inclusive A_{UT} [21]. Together these results demonstrate that neither the Sivers nor the Collins mechanism, individually or combined, can account for the large inclusive π^0 A_{UT} at $\sqrt{s}$ = 500 GeV!

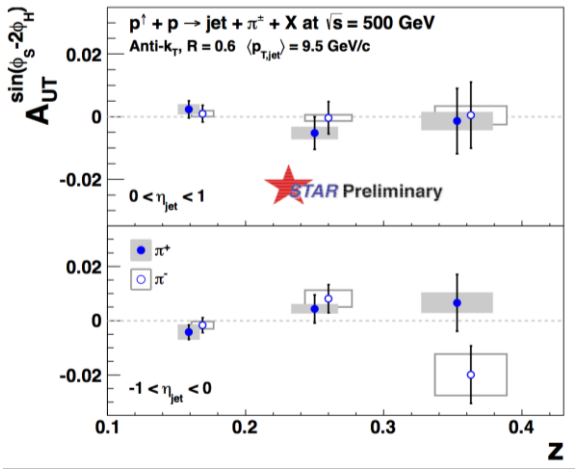

Figure 2-11 "Collins-like" asymmetries as a function of pion z for three bins of jet p_T and two bins of jet η relative to the polarized beam. The present "Collins-like" asymmetries will provide the first experimental constraints on model predictions utilizing linearly polarized gluons.

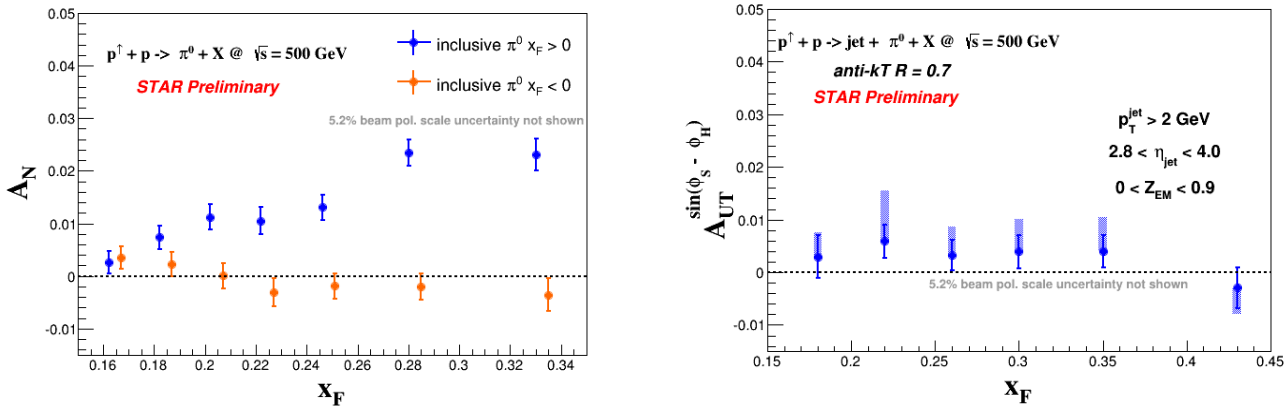

Figure 2-12 Left: the inclusive π^0 A_{UT} vs xF for forward (blue) and backwards (orange) scattered particles. Right: the Collins A_{UT} vs xF for π^0 in neutral jet-like events. Both asymmetries are constructed from particles reconstructed in the FMS.

2.2.2 Longitudinal Spin Program

Investigations into the origin of the proton spin have provided a long-standing motivation for colliding longitudinally polarized protons at RHIC. The analysis of inclusive jet double spin asymmetries (A_{LL}) from data taken at $\sqrt{s}$ = 200 GeV during the 2009 run provided the first conclusive evidence of a significant gluon contribution to the proton spin. The impact of these measurements, along with similar results from PHENIX, on the integral of the gluon helicity distribution $\Delta g(x)$ from x_{MIN} to one is shown in Figure 2-13. The red line indicates the best fit from the DSSV global analysis and the sky blue curve represents the uncertainty associated with this analysis. Note that the tightest constraints to date come from the RHIC $\sqrt{s}$=200 GeV data in the region of $0.05 < x < 1$. This curve expands rapidly at lower x values, motivating the need for additional A_{LL} measurements at higher center of mass energies.

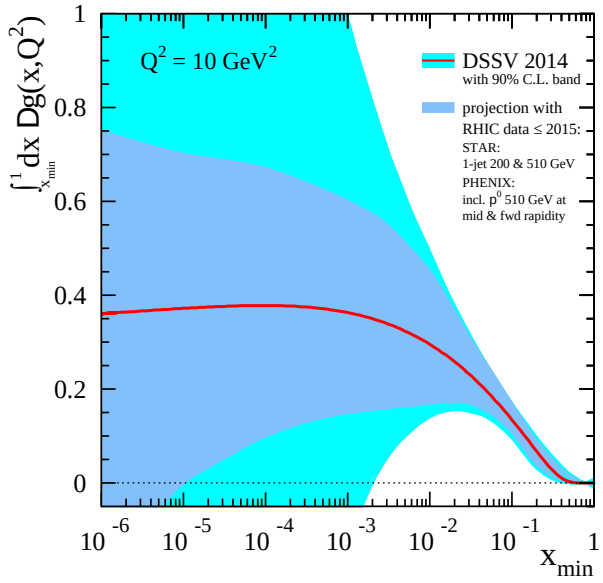

Figure 2-13 The running integral for Δg as a function of x_{MIN} at Q^2 = 10 GeV^2 as obtained in the DSSV global analysis framework. The inner and outer uncertainty bands at 90% C.L. are estimated with and without including the combined set of projected pseudo-data for preliminary and future RHIC measurements up to Run-2015 respectively.

Since the last PAC meeting STAR has released two new A_{LL} results from data taken at √s = 510 GeV. The first, shown in Figure 2-14, is the mid-rapidity inclusive jet A_{LL} plotted as a function of $x_T = 2p_T/\sqrt{s}$. The new asymmetries (red points) agree well with the results from the run 2009 √s = 200 data (blue points) in the region of overlap and will push the constraints on Δg(x) into a new lower x regime.

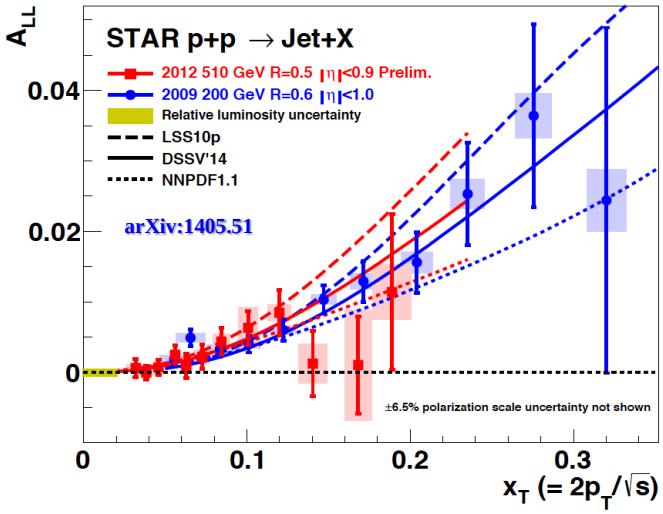

Figure 2-14 ALL vs. xT for inclusive jet production at midrapidity in 200 GeV (blue circles) [7] and 510 GeV (red squares) p+p collisions, compared to predictions from three recent NLO global analyses [4,8,9] (blue curves for 200 GeV and red curves for 510 GeV).

The second result is the double spin asymmetry of neutral pions reconstructed in the FMS (shown in Figure 2-15). Although the pion A_{LL} in this kinematic region ($2.8 < \eta < 4.0$) is expected to be small, it is also sensitive to gluons at $x \sim 10^{-3}$. The successful release of the mid-rapidity inclusive jet and the forward rapidity neutral pion A_{LL} has launched STAR into a new era of lower x gluon helicity measurements.

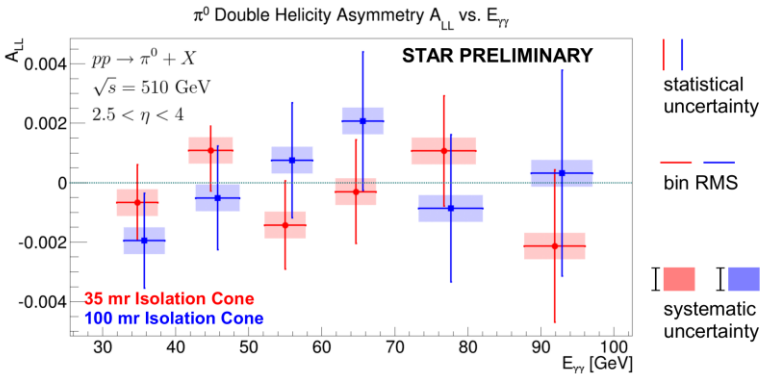

Figure 2-15: The π^0 A_{LL} in Eγγ bins for two isolation cones. The vertical error bars are statistical uncertainties, while the horizontal error bars indicate the RMS of each Eγγ bin. The blue points are offset by 1 GeV for visibility.

Since the last PAC the STAR spin working group has published in PRL the high statistics $W^{+/-}$ longitudinal single spin (A_L) analysis from the combined 2011 and 2012 $\sqrt{s}$ = 500 (510) GeV data. The value and precision of these results significantly impact our understanding of the light sea quark polarizations. In the case of the W^- asymmetry, the STAR data lie above the central curve based on DSSV fits to semi-inclusive and inclusive data, reflecting a shift of the anti-up quark spin distribution away from the previous mean value. As a result these measurements provide the first clear evidence of flavor symmetry breaking in the polarized sea. The green shaded curve in Figure 2-16 demonstrates the current best fit and associated errors on the polarized light sea asymmetry $x(\Delta\bar{u} - \Delta\bar{d})$ from the NNPDF global analysis. The red curves indicate the precision once all of the RHIC data from run 2013 is included.

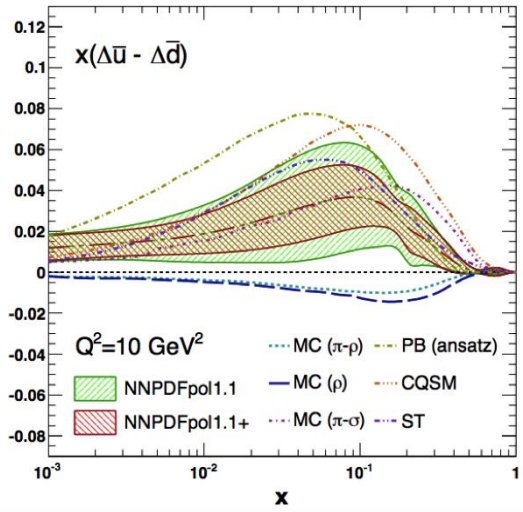

Figure 2-16 The polarized light sea-quark asymmetry $x(\Delta\bar{u} - \Delta\bar{d})$ computed with NNPDFpol1.1 and NNPDFpol1.1+ PDFs [22]. Chiral quark soliton and Pauli blocking models are favored while several cloud based models are disfavored. A review of the models may be found in [23].

STAR's ability to identify $W^{+/-}$, either through $e^{+/-}$ decay or by recoil jet techniques, provides a unique opportunity to measure the ratio ($R^{W+/W-}$) of the W^+ and W^- cross-sections. $R^{W+/W-}$ is sensitive to the unpolarized light sea quark distributions in the region of x > 0.05 and is free of the corrections and systematic errors associated with the nuclear targets typically used in experiments that probe these distributions. Utilizing the same data as in the $W^{+/-}$ A_L result above, STAR has measured $R^{W+/W-}$ as a function of both lepton and W pseudorapidity. Figure 2-17 shows the preliminary measurements released for the recent DIS2015 conference. The yellow curves represent the current uncertainties in $R^{W+/W-}$ solely due to uncertainties in the light sea parton distribution functions.

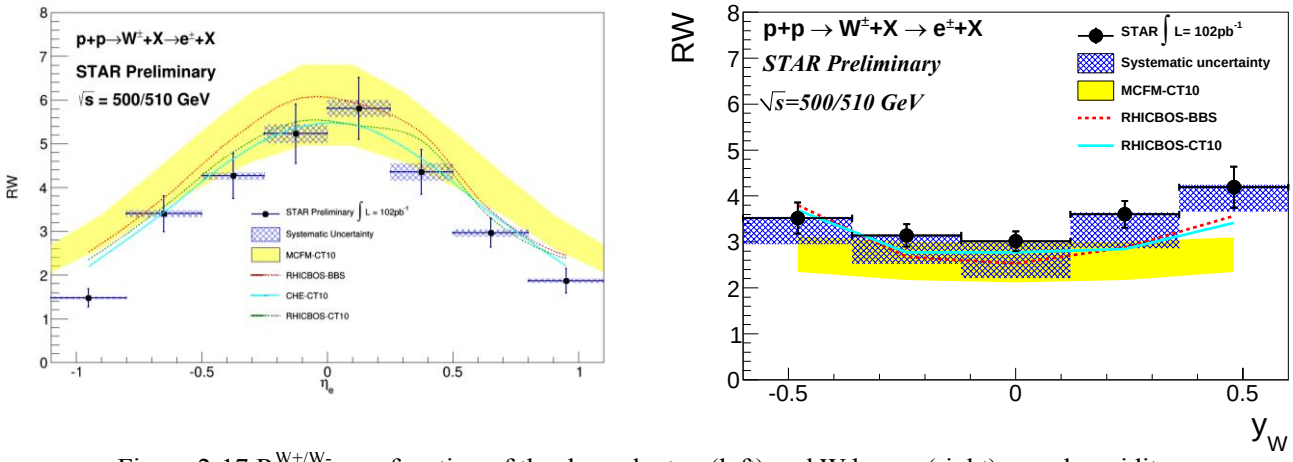

Figure 2-17 $R^{W+/W-}$ as a function of the decay lepton (left) and W boson (right) pseudorapidity.

2.3 Summary of experimental search for the Chiral Magnetic Effect

Signals of chiral effects have been sought by STAR for the past decade, and thus far the measured experimental observables support pictures of the chiral magnetic effect, the chiral magnetic wave and the chiral vortical effect. However, to draw firm conclusions an effective technique to disentangle the signal from the background contributions, the latter of which is intertwined with collective flow, is still needed. To this end, collisions of isobaric nuclei, i.e. ${}_{44}{}^{96}\mathrm{Ru}$ + ${}_{44}{}^{96}\mathrm{Ru}$ and ${}_{40}{}^{96}\mathrm{Zr}$+${}_{40}{}^{96}\mathrm{Zr}$, present a unique opportunity. Such collisions allow the initial magnetic field to be significantly varied whilst keeping all other conditions essentially the same. In addition, the deformation of the Zr nucleus affects elliptic flow such that separation between the signal and background is slightly favored. We request 1.2B events for each collision system at $\sqrt{s}$ = 200 GeV in order to reach a 5σ significance. 400M events may still yield a 3σ effect.

2.3.1 Chiral magnetic effect

For decades, scientific models of our universe have included the possibility that we live in a long-lived, but not completely stable, domain of space. Such a state can potentially be destroyed at any time by ``toppling" into a more stable vacuum state. While our universe, created via the Big Bang, has only one life to live, the billions of Little Bangs at RHIC can illuminate our ultimate destination. It is theoretically possible that metastable domains of topologically twisted gluon fields inside the QGP vacuum transition resulting in violations of the space and time reflection symmetry, such as a chirality imbalance.

The experimental search for such local parity violation in the strong interaction was greatly intensified once it was realized [24,25] that evidence of this effect could be observed in non-central nuclear collisions. A charge separation, known as the chiral magnetic effect, manifests out of the chirality imbalance of massless quarks with the help of the strong magnetic field (~10^{15} T) produced in a non-central collision. This signal is known as the chiral magnetic effect (CME) [24,26] and results in an asymmetry in the emission of positively and negatively charged particles along the direction of the angular momentum of the collision.

A three-point correlator, $\gamma = < \cos(\Phi_\alpha + \Phi_\beta - 2\Psi_{RP}) >$, sensitive to the CME was proposed [27], where Φ is the azimuthal angle, the subscripts α and β denote the particle charge (positive or negative), and Ψ_{RP} is the angle of each event's reaction plane. The observable γ represents the difference between azimuthal correlations projected onto the direction of the angular momentum vector and correlations projected onto the collision event plane. STAR's measurements of this correlator for Au+Au collisions at $\sqrt{s}$ = 200 GeV [28,29,30] shown in Figure 2-18 (b) demonstrate the expected ordering of the opposite charge (γ_{OS}) and the same charge (γ_{SS}) correlations. This is consistent with the formation of deconfined and chirally-symmetric restored matter in high-energy heavy-ion collisions. The signal is robust to various techniques of determination of the reaction plane, and persists when the collision system changes to Cu+Cu, Pb+Pb or U+U. No known event generators can reproduce the experimental signal. Figure 2-18 presents γ_{OS} and γ_{SS} correlators for Au+Au collisions at $\sqrt{s_{NN}}$ = 7.7 - 200 GeV as a function of centrality [31]. In addition, the ALICE measurements for 2.76 TeV Pb+Pb collisions are also shown [32]. An ordering of γ_{OS} and γ_{SS} is present at higher energies. This is consistent with extra charge-separation fluctuations along the magnetic field due to the CME. At lower beam energies, both γ_{OS} and γ_{SS} tend to rise for peripheral collisions. This feature seems to be charge independent, and is explained by momentum conservation and elliptic flow [30].

An ambiguity in the interpretation of experimental results comes from possible background correlations not related to the CME. The background sources, if coupled with collective flow, will contribute to γ. In order to study impact of the background contributions on the signal associated with the CME, we can express the experimental observables in the following forms, where the unknown parameter κ is of the order of unity [33].

$$\gamma \equiv < cos(\phi_\alpha + \phi_\beta - 2\psi_{RP}) >= \kappa v_2 F - \mathrm{H}$$
$$\delta \equiv < cos(\phi_\alpha - \phi_\beta) >= \mathrm{F} + \mathrm{H}$$

where H and F are the CME and background contributions, respectively. For the STAR acceptance $\kappa \approx 1.2$. Figure 2-19 shows (H_{SS} -H_{OS}) as a function of beam energy for three centrality bins in Au+Au collisions [30]. The default values (dotted curves) are from $H^{\kappa=1}$, and the solid curves are obtained with κ = 1.5. For comparison, the results for 10-60% Pb+Pb collisions at 2.76 TeV are also shown [32]. With increased κ, ΔH decreases for all beam energies. For both κ values, ΔH demonstrates a weak energy dependency above 19.6 GeV, and tends towards zero at the lowest beam energy, although the statistical errors are large for 7.7 GeV. Recent STAR preliminary ΔH results for 14.5 GeV collisions further confirm the trend established by other beam energies. This trend may be explained by the dominance of hadronic interactions over partonic ones at the lowest energies. The energy for which ΔH=0 will be determined quantitatively with higher statistics in the BES Phase-II.

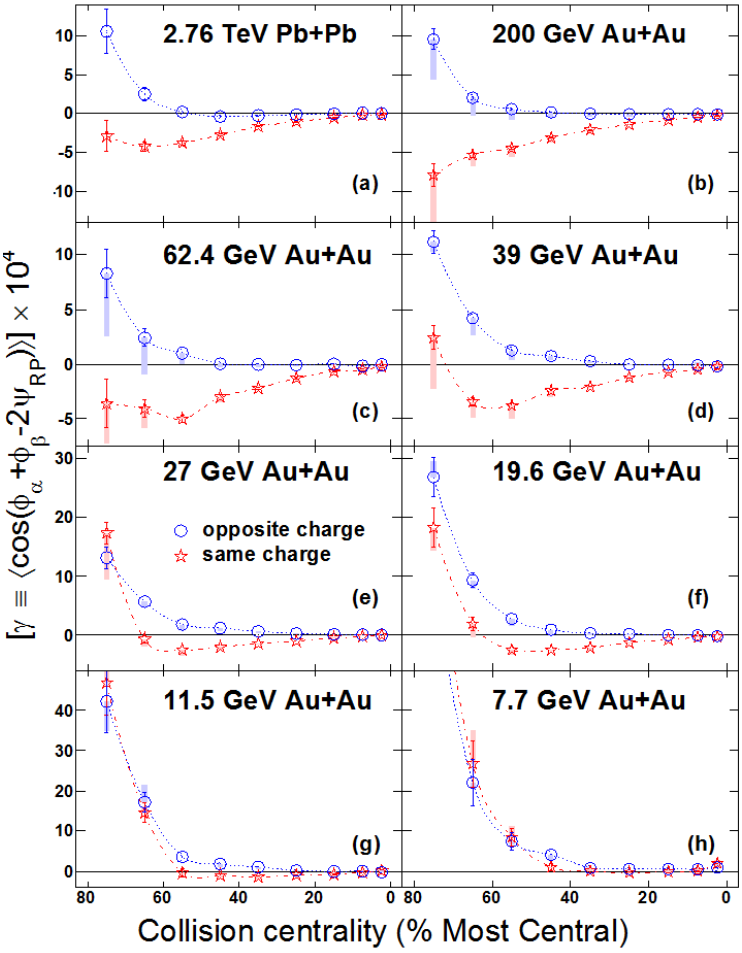

Figure 2-18 The three-point correlator, γ, as a function of centrality for Au+Au collisions at $\sqrt{s}$ = 7.7-200 GeV [30]. Note that the vertical scales are different for different rows. The systematic errors (filled boxes) reflect the extra conditions of $\Delta p_T > 0.15$ GeV/c and $\Delta\eta > 0.15$ to suppress HBT + Coulomb effects.

To further probe how flow-related backgrounds affect our experimental CME signals the prolate shape of the uranium nuclei ($\beta_2 = 0.29$) [34] was utilized. We collected 0-1% most central events from U+U collisions at 193 GeV during the 2012 RHIC run and the preliminary results [35] (Figure 2-20) show a charge-separation signal consistent with zero despite a sizeable measured elliptic flow, v_2 ~2.5%. This is consistent with the picture of the CME since the magnetic field is minimal in very central collisions. These results also demonstrate that flow-related backgrounds are very small in those events. However, a model-dependent extrapolation has to be employed to estimate the background contributions for non-central collisions where the charge separation is more prominent. On the other hand, the mid-central/mid-peripheral events in U+U and Au+Au collisions seem to be qualitatively similar due to a great deal of mixed geometry configuration in given centrality. Collisions of Isobar as proposed will provide a necessary discrimination power for such a centrality and system size.

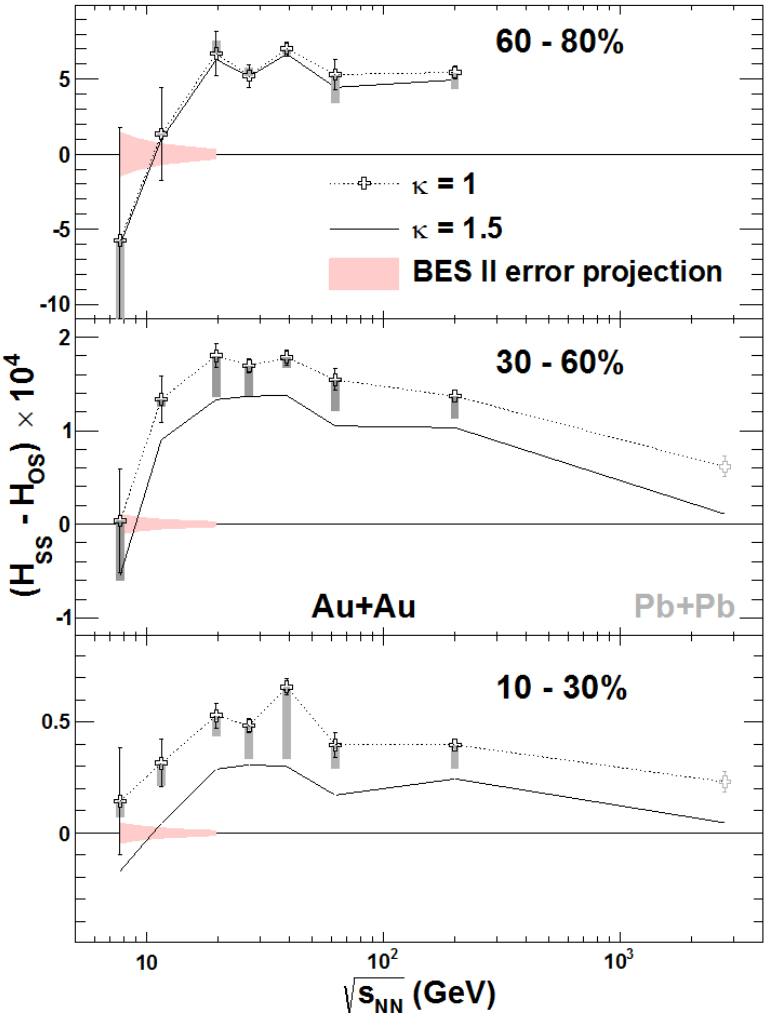

Figure 2-19 shows (H_{SS}-H_{OS}) as a function of beam energy for three centrality bins [31]. The default values (dotted curves) are from $H^{\kappa=1}$, and the solid curves are obtained with κ=1.5. For comparison, the results for Pb+Pb collisions at 2.76 TeV are also shown [32]. The systematic errors have the same meaning as in Figure 2-18.

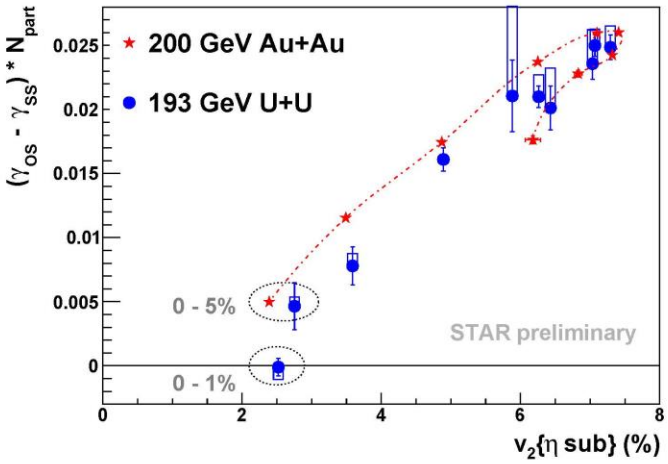

Figure 2-20 (γ_{OS}-γ_{SS})× Npart vs v2 for Au+Au collisions at 200 GeV and U+U collisions at 193 GeV [35].

2.3.2 Chiral Magnetic Wave

Besides the chiral magnetic effect, the chiral separation effect (CSE) has also been proposed. The CSE refers to the separation of chiral charge along the axis of the magnetic field at finite density of vector charge (e.g. electric charge) [36,37]. In a chirally-symmetric phase, the CME and CSE form a collective excitation, a Chiral Magnetic Wave (CMW); a long-wavelength hydrodynamic mode of chiral charge densities [38,37]. The CMW is a signature of chiral symmetry restoration in the QGP, and manifests itself in a finite electric quadrupole moment of the collision system, where the "poles" ("equator") of the produced fireball acquire additional positive (negative) charge. This effect, if it exists, will be reflected in the measurement of charge-dependent elliptic flow. Taking pions as an example, on top of the baseline v_2^{base} ($\pi^{\pm}$), the CMW will lead to [38]:

$$v_2(\pi^{\pm}) = v_2^{base}(\pi^{\pm}) \mp \left(\frac{q_e}{\overline{\rho_e}}\right) A_{ch}$$

where q_e, $\overline{\rho_e}$ and $A_{ch} = (N^+-N^-)/(N^++N^-)$ are the quadrupole moment, the net charge density, and the charge asymmetry of the collision event, respectively. Since v_2^{base} may differ for π^+ and π^- due to several other physics mechanisms, it is less ambiguous to study the CMW via the A_{ch} dependence of the pion's v_2.

Taking 30-40% 200 GeV Au+Au as an example, the pion v_2 is shown as a function of A_{ch} in panel (a) of Figure 2-21 [39]. The $v_2(\pi^-)$ increases with A_{ch} while the $v_2(\pi^+)$ decreases at a similar rate. The v_2 difference between π^- and π^+ is fit to a straight line in panel (b). The slope parameter r, or presumably $2q_e/\overline{\rho_e}$ from $v_2(\pi^{\pm}) = v_2^{base}(\pi^{\pm}) \mp \left(\frac{q_e}{\overline{\rho_e}}\right) A_{ch}$), is positive and qualitatively consistent with the expectation of the CMW picture.

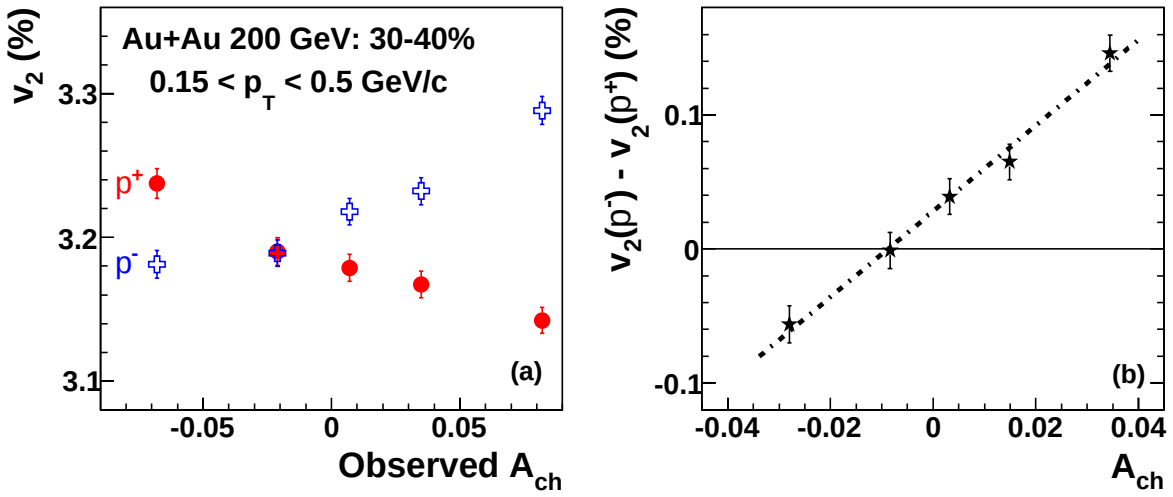

Figure 2-21 (a) pion v_2 as a function of observed charge asymmetry and (b) v_2 difference between π^- and π^+ as a function of charge asymmetry with the tracking efficiency correction, for 30-40% Au+Au collisions at 200 GeV [39].

Figure 2-22 shows the extracted slope parameter r for all measured centrality bins [39]. The grey bands include the systematic errors due to the DCA cut, the tracking efficiency and the p_T range of particles involved in the event plane determination. A similar trend and magnitude of the slopes for Au+Au collisions from 200 GeV to 19.6 GeV is observed. The slopes are consistent with zero for the most central and most peripheral collisions, and are positive and reach a maximum in mid-central/mid-

peripheral collisions. Below 19.6 GeV large statistical errors prevent firm conclusions. The high statistics expected from BES Phase-II will significantly reduce these statistical errors, and enable the extension of this search for the CMW to lower energies. The disappearance of the CMW at lower energies would signify chiral symmetry breaking.

For comparison we also show in Figure 2-22 UrQMD calculations [40] and simplified CMW calculations with different duration times [41]. For the 10-70% centrality range in Au+Au collisions at 200 GeV, where the signal from the real data is most prominent, the slopes extracted from UrQMD events and the AMPT event generator [42] (not shown in figure) are consistent with zero. On the other hand, the simplified CMW calculations demonstrate a similar centrality dependence of the slope parameter [41].

Finally, STAR preliminary results with kaons in Au+Au collisions at 200 GeV and U+U collisions at 193 GeV, studying v_3 instead of v_2, also favor the CMW interpretation [43].

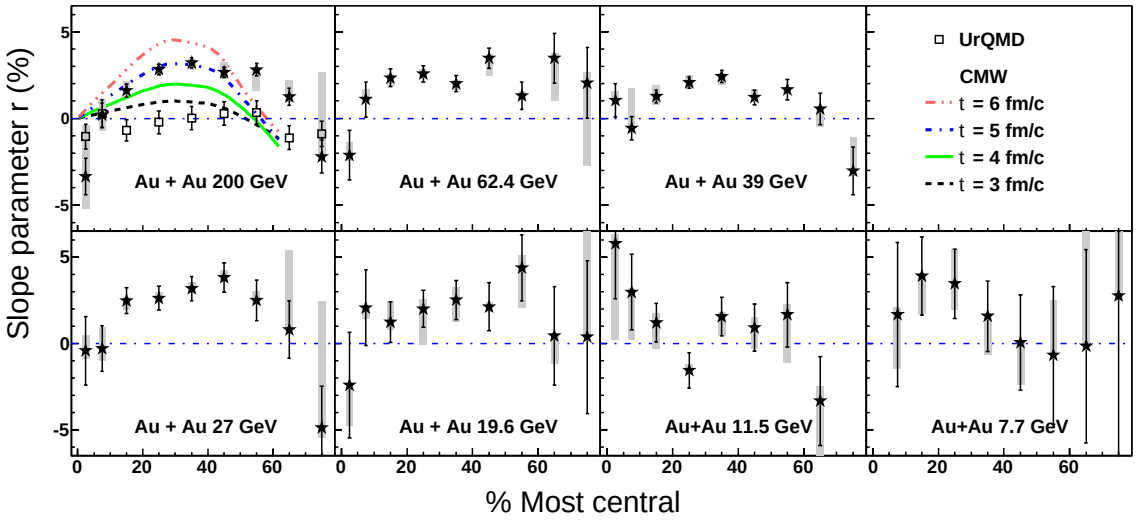

Figure 2-22 The slope parameter r as a function of centrality for all the collision systems under study [39].

2.3.3 Chiral Vortical Effect

In addition to the chiral magnetic effect, a chiral vortical effect (CVE) has been predicted [44]. In this case the role of a field is played by vorticity, instead of the magnetic field in the CME, and baryon number density replaces the electric charge as the vector field. Vorticity in heavy-ion collisions is a natural consequence of angular momentum conservation. Baryon number separation due to the CVE will occur in analogy with the electric charge separation due to the CME. Indeed, recent STAR preliminary results for Λ-proton correlations [45] show a separation between opposite- and same-baryon number correlators (γ) in Au+Au collisions at 200 GeV. The statistics requested for BES Phase-II will enable such an analysis at lower energies, where the relative importance of baryon number separation increases with decreased beam energy of collisions since μ_B is larger.

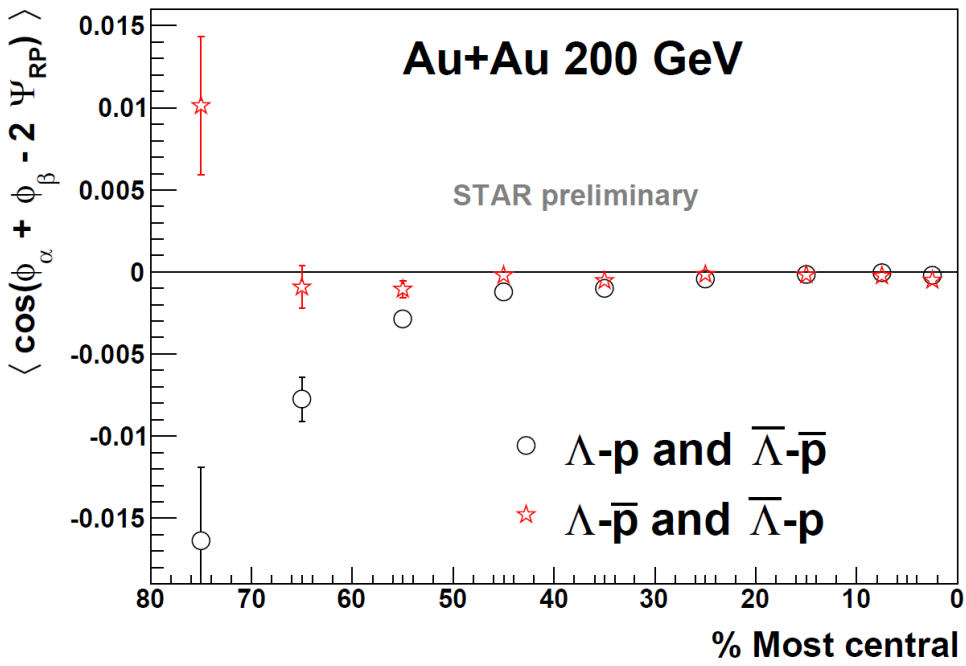

Figure 2-23 γ correlation of Λ-p (same baryon number) and Λ- $\bar{p}$ (opposite baryon number) vs centrality in Au+Au collisions at 200 GeV [43].

2.4 Progress on tracking with the Heavy Flavor Tracker

During the run-14 the HFT was fully commissioned in the Au-Au run. In particular both the PXL and the IST detector subsystems were included in all of the physics runs for 200 GeV Au+Au. As part of the close-out of the HFT project preliminary tracking was utilized to demonstrate that the performance of the HFT detector met the project goals. This is shown in the figures below, Figure 2-24 shows that the efficiency for tracking with IST and PXL alone reached 65%, while Figure 2-25 shows that the production tracking software results in excellent pointing resolution for the two ladders that were Al-based ladder cables. For the detectors as a whole better than 50 microns was achieved.

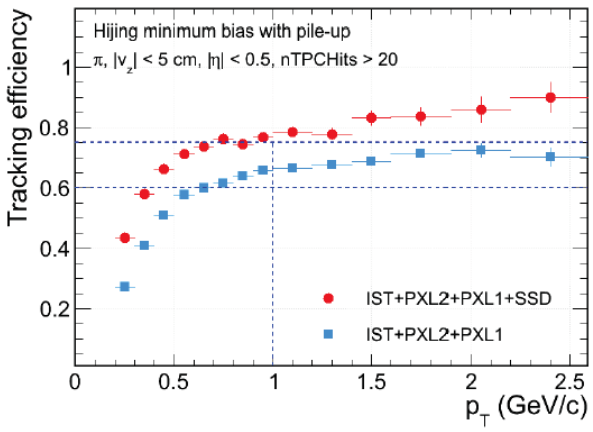

Figure 2-24: Tracking efficiency for pion in full simulation vs. p_T for full HFT (red) and PXL+IST only

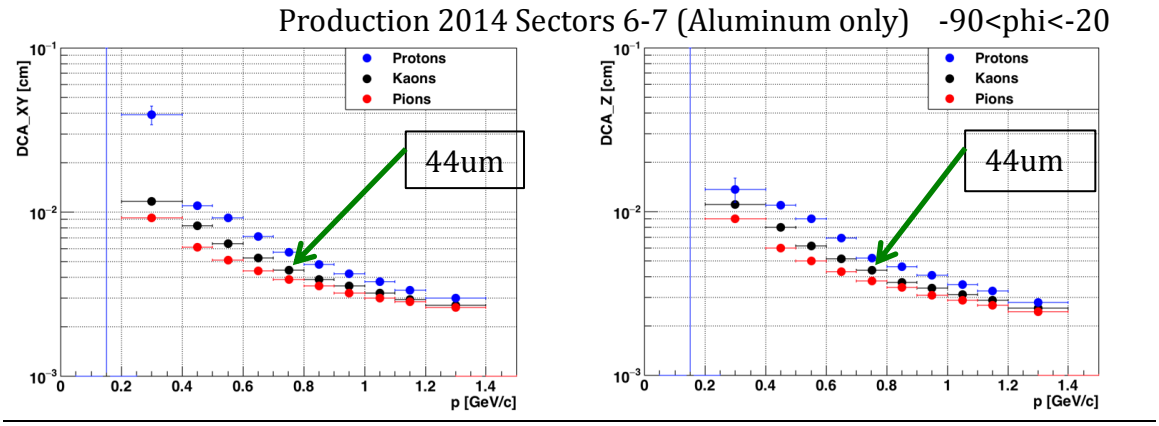

Figure 2-25 DCA resolution in current Production of 2014 data for the two sectors with Aluminum cables. The left/right panel shows the XY/Z directions respectively. The numbers are for 750 MeV/c Kaons.

The tracking software was integrated into the offline software library, and the full Run14 dataset were under-going the production processing. Figure 2-26 shows the invariant mass distribution of kaon-pion candidate pairs from 125M minimum bias Au+Au 200 GeV production data taken in Run 14 after applying the topological cuts enabled by the HFT. The significance of the clear D^0 signal is about 18σ in this sample. The kaon and pion candidate tracks were identified using the dE/dx in the TPC and required to have at least one hit in each layer of PXL and IST. The topological cuts on the daughter tracks as well as the pairs enabled by the HFT performance were imposed to obtain this distribution. The K-pi invariant mass distribution without the HFT topological cuts is shown in the inserted panel. The background reduction due to the HFT cuts is more than 4 orders of magnitude.

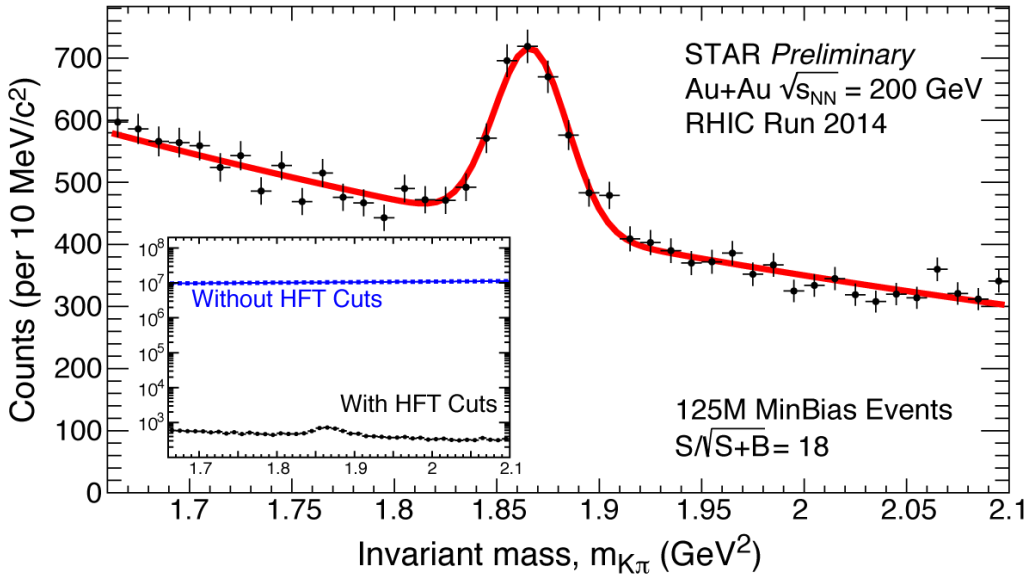

Figure 2-26: Invariant mass distribution of K-pi pairs from 125M minimum bias 200 GeV Au+Au data taken from Run14 with the HFT topological cuts applied. The D^0 signal significance is about 18σ in this sample. The insert panel shows the distributions without and with the HFT cuts. The combinatorial background level is reduced by more than 4 orders of magnitude.

2.5 Progress on production with the Muon Telescope

The MTD calibration for Run 2014 data was done using the cosmic ray data taken during Run 2014. The calibration results indicate that the timing and spatial resolutions are as good as expected, 100 ps and 1-2 cm, respectively. The calibration tables were in the STAR standard database before Run 2014 200 GeV Au+Au data were produced.

In Run 2014, in addition to the large data set of the MTD triggered events, STAR took more than 1 billion minimum-bias triggered events with the Heavy Flavor Trigger (HFT). On Mar 26th, 2015, the official data production for the HFT physics was started. The MTD group is using this dataset to check the MTD performance. With the calibration parameters implemented, we observed a narrow muon-peak contribution in the timing distribution. Figure 2-27 shows the difference of the time of flight between the measured MTD hits and the expected muon tracks. The black histogram represents the case for all the matched tracks. The red represents the case with more strict matching conditions, namely, by cutting the position difference along the beam line direction between the measured hits and the expected muon tracks within 20 cm. With a stricter matching cut, muon contribution becomes more prominent as the long tail on the right side, mainly from hadrons, is significantly suppressed. By adding additional cuts on the normalized ionization energy loss ($n\sigma\pi$), as indicated by the blue histogram, the tail on the right side gets even more suppressed. More detailed study is ongoing to disentangle the contributions from muons and different hadron species.

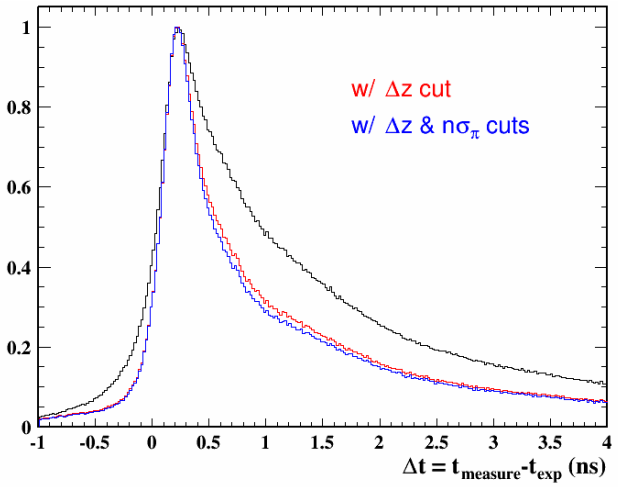

Figure 2-27: The difference of the time of flight between the measured MTD hits and the expected muon tracks with different cuts. The details are in the text.

With the muon identification from the MTD, we observe the ω, ϕ, and J/ψ peaks in minimum-bias Au+Au collisions at 200 GeV. Figure 2-28 shows the dimuon invariant mass distributions. The circled symbol and red histogram represent the unlike-sign and like-sign distributions, respectively. The unlike-sign distribution contains both the dimuon signal and background while the like-sign is used to describe the background. One can observe that there is a signal excess in the ω, ϕ, and J/ψ peak regions. We note that MTD triggered data have a factor of 50 more statistics compared to what we show here. The dimuon continuum analysis should be very promising.

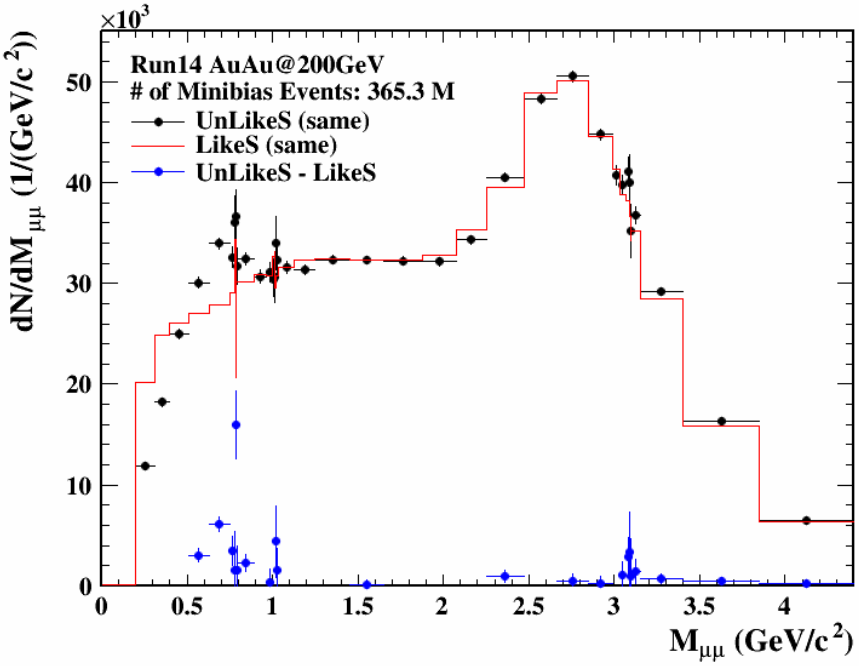

Figure 2-28, Dimuon invariant mass distributions from 365 million minimm-bias triggered events in Au+Au collisions at $\sqrt{s_{NN}}$ = 200 GeV. Details are in the text.

For the MTD dimuon triggered data production, we proposed to the STAR Collaboration that we use a two-iteration production approach. In the first iteration, we do not do a full tracking for all the 24 TPC sectors. Instead, we only perform tracking to those TPC sectors in which the tracks can match to the MTD hits. For the second iteration, we do a full tracking for all the 24 TPC sectors for those events with two matched tracks. The idea was accepted by STAR and the outcome of this approach is that we will save 50% of the production time compared to the normal production procedure. The filtering code for the first interaction was passed to the Software & Computing (SC) group on Feb. 16th, 2015. The review was completed on April 7th, 2015. Integration efforts from the SC group are ongoing and data production for dimuon triggered events will start after integration is completed. We expect enough data will be produced so that quarkonium results would be ready for Quark Matter 2015 conference.

MTD data analysis status in 510 GeV p+p collisions from Run 2013:

In Run 2013, 63% of the full MTD system was installed and took data smoothly. Figure 2-29 shows the dimuon invariant mass distributions from 98 million dimuon triggered events in p+p collisions at 510 GeV. The circled symbol and red histogram represent the unlike-sign and like-sign distributions, respectively. One can observe that there is a clear signal excess in the ω, ϕ, and J/ψ peak regions with the like-sign background subtracted. We note with negligible Bremsstrahlung radiation effect for muons, the J/ψ signal reconstructed though dimuon channel is symmetric. We expect to show the efficiency corrected invariant cross section of J/ψ in 500 GeV p+p collisions at Hard Probes 2015 conference.

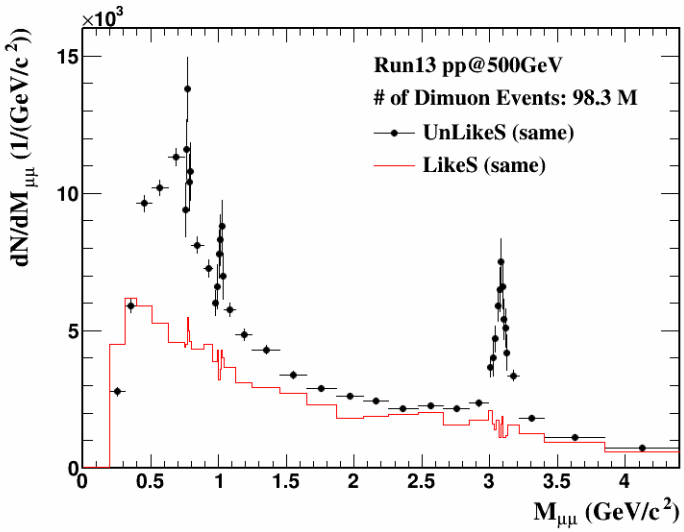

Figure 2-29: Dimuon invariant mass distributions from 98 million dimuon triggered events in p+p collisions at $\sqrt{s}$ = 500 GeV. Details are in the text.

2.6 Au+Au 14.5 GeV and Beam Energy Scan Program

The first collisions for the 14.5 GeV Au+Au system were established on February 13th, 2014. After some initial beam development, physics data taking started on February 17th and continued through March 11th for a total of 22 days of collisions for physics. Over 420M triggered events were recorded, however most were random background; the figure of merit was the number of VPD minimum bias triggers, of which 21M were recorded. The estimate at the time was that this would yield 12M good events within 30 cm of the center of the detector. Post production analysis confirms that there are between 11 million good Au+Au events in the data set using the most stringent event quality cuts ($|V_Z| < 30$ cm). More relaxed cuts ($|V_Z| < 70$ cm) yield up to 27M good events. These event yields meet the goals of the 14.5 GeV run, which was to achieve event statistics for this energy that are comparable to the other BES energies.

An initial offline pre-production of these data was run in March of 2014. Results for all of the key analyses were generated to verify that we had sufficient statistics, however the calibrations had not been completed and the software had not been updated to account for the added material of the HFT. Therefore these results were not presented at conferences. The fully calibrated and updated production of the 14.5 GeV data was completed in January of 2015. Analysis of these final data has taken place. Preliminary results are now available for all of the key analyses and plans have been developed for presentation and publication of these new results. The physics goals of the BES program breakdown into three broad areas: disappearance of QGP signatures, evidence of a softening of the equation of state consistent with a first-order phase transition, and evidence of fluctuations consistent with crossing a critical point.

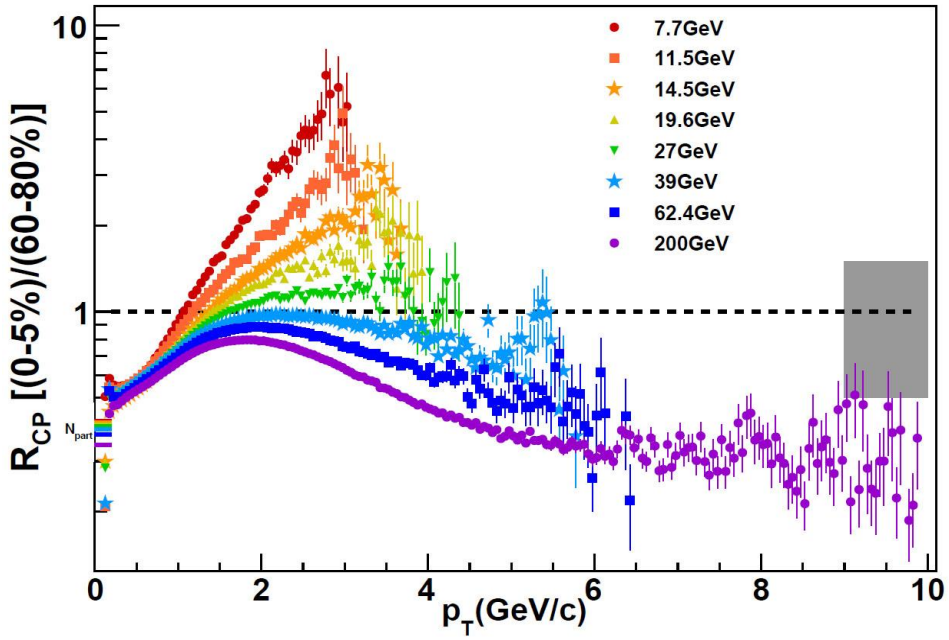

Figure 2-30. The R_{CP} of charged hadrons for all BES energies, including the new 14.5 GeV data.

Several QGP signatures have been shown to disappear in the lower energies of the BES range. Results for the R_{CP} of hadrons show that the high p_T suppression disappears at the lower energies. As shown in Figure 2-30, the new results are available at 14.5 GeV and are consistent with the trends of the other energies. These new results will be included in paper, which is currently in preparation, covering all the BES energies. The elliptic flow of the phi meson is possibly inconsistent with that of other particles at 11.5 GeV. Performance data for the phi analysis are shown in the left panel of Figure 2-31. Preliminary results from 14.5 GeV show the flow of the phi meson to exhibit the constituent quark scaling. New results for the asymmetry between the flow of particles and anti-particles are now available for the 14.5 GeV data. These data are consistent with the trends of the other energies. These new flow results will be included in a long BES elliptic flow paper, which is in preparation. Flow measurements are also available for other identified hadrons. The yields of strange particles are expected to be enhanced in a QGP. In order to study this strangeness enhancement, the p_T spectra and yields of strange hadrons (K^+, K^-, K^0_S, ϕ, Λ, Ξ, and Ω) have been measured. Performance data for the Ω^+ baryon are shown in the right panel of Figure 2-31. These strange hadron yields are then compared to the spectra and yields for the π^+, π^-, p, and $\bar{p}$. Combining these spectra results allows one to determine the *T* and μ_B of chemical freeze out and the strangeness enhancement. The new 14.5 GeV results will be included in papers that address the other BES energies and are currently in collaboration review.

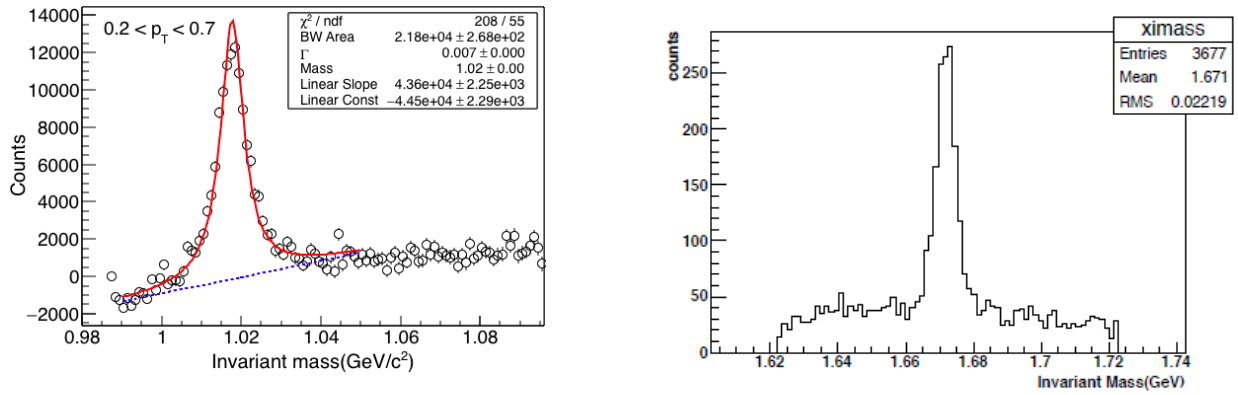

Figure 2-31. The Invariant mass peaks are shown for the ϕ meson on the left and the Ω+ baryon on the right.

Some of the most suggestive results from the BES data from 2010 and 2011 concerned evidence for a softening of the equation of state. The most compelling evidence of a softening of the equation of state comes from the directed flow of the protons. The participating protons recoil off of the interaction zone. Thus the magnitude and sign of the directed flow is indicative of the incompressibility of the created matter. This flow signature was seen to be negative for the 11.5 and 19.6 GeV energies. Analysis of the 14.5 GeV system shows an even more negative v_1 result, which may help define the location of the softest point. These results will be included in a kaon directed flow paper which is currently in preparation. Although signatures have been identified which appear to be consistent with a softening of the equation of state of QCD matter, a softening is expected for all types of phase transitions and only quantitative comparisons to models will determine whether the observed results conclusively demonstrate evidence of a first order phase transition.

The clearest indication of understanding the phase diagram of QCD matter would be the identification of a critical point. One expects to see evidence of critical fluctuations in the final state distributions of particles for reaction trajectories, which pass near this critical point. For trajectories approaching the critical point from the low μ_B side, we now expect a reduction in the kurtosis signals, while trajectories approaching from the high μ_B will exhibit an increased kurtosis signal. Analyses of the higher moments signals for net-charge (net-Q), net-kaons (proxy for net-S), net-protons (proxy for net-B) have been completed. These results are under careful collaboration review and will be presented first at QM2015 and then included in papers currently in preparation. The net-proton result will be included in a paper which uses wider acceptance cuts ($0.4 < p_T < 2.0$ GeV/c) and uses all BES energies including the new 14.5 GeV point. The net-kaon results will be included in a paper that shows all the BES energies. These precision of these fluctuation measurements are limited by the available statistics. New results from particle ratio fluctuations are also available. These are consistent the trends demonstrated by the other BES energies. The new results at 14.5 GeV confirm the trends of the other BES energies and provide further evidence to support the need for a higher luminosity BES-II phase program focusing on the energy region from 5-20 GeV. Additional studies possibly showing a minimum of incompressibility are available using the higher order flow measurements (v_n). These results will be included in a paper, which is in preparation, addressing all the BES energies.

RHIC completed the first phase of such an energy scan in 2014, taking Au+Au collision data at a series of beam energies (200, 62.4, 39, 27, 19.6, 14.5, 11.5 and 7.7 GeV) corresponding to values of baryonic chemical potential that range from 20 to 400 MeV. During 2014-15, the STAR experiment has made significant progress in its data analysis efforts including studies of (1) the energy dependence of the mid-rapidity kaon v_1 slopes [46,47,48], see Figure 2-32; (2) Event-by-event identified particle ratios [15]; (3) the beam energy dependence of moments of the net-charge multiplicity distributions,

published in [14] and (4) the beam energy dependence of moments of the net-proton multiplicity distributions [49,50] in a much wider transverse momentum window with the aid of the time-of-flight detector, see Figure 2-33. In addition, the analysis of the 14.5 GeV Au+Au collision data over a wide range of observables is also close to completion.

As examples, we discuss two recent results from the RHIC BES program. Shown in Figure 2-32 are STAR preliminary results on energy dependence of the mid-rapidity kaon v_1 slopes (triangles) from mid-central 10-40% Au+Au collisions at RHIC. Results of the mid-rapidity slopes of pion (squares) and proton (circles) have been published [46]. As one can see in the figure, while proton's v_1 slope changes sign between 11.5 and 7.7 GeV, the values of the mid-rapidity v_1 slope for all produced hadrons are all remaining to be negative over the measured energy range. This result points to the difference between the quarks brought in by the incoming nuclei and the produced quarks at the high net-baryon density region. Model calculations by UrQMD (yellow bands) [47] and HSD (green bands) [48] show qualitative agreement with data but differ in details. More high statistics data, especially at the lower collision energy region, are needed in order to understand the dynamics in the high net-baryon density region.

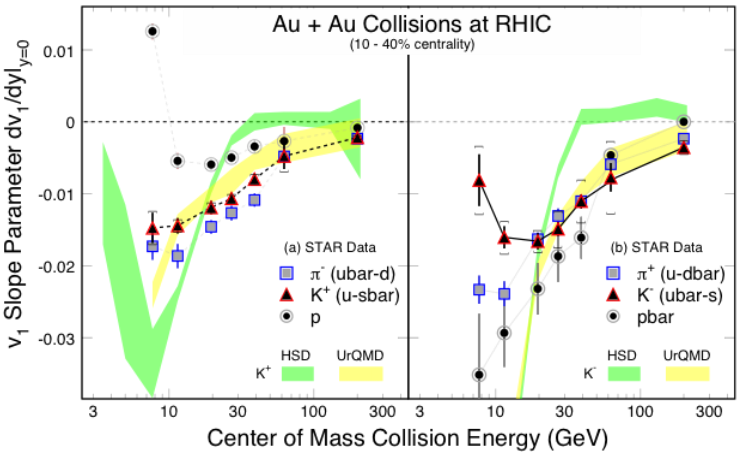

Figure 2-32: STAR preliminary results on energy dependence of the mid-rapidity kaon v_1 slopes (triangles) from mid-central 10-40% Au+Au collisions at RHIC. Results of the mid-rapidity slopes of pion (squares) and proton (circles) have been published [46]. All error bars are statistical and the systematic errors are shown as caps. The yellow and green bands are the results of model calculations from UrQMD [47] and HSD [48], respectively.

The next example is the beam energy dependence of the net-proton multiplicity distributions [49,50] shown in Figure 2-33. The data is from the top 5% central Au+Au collisions at RHIC. Data points on kurtosis and skewness are shown in panels (a) and (b), respectively. The published results (triangles) are all from $0.4 < p_T < 0.8$ GeV/c, limited by the PID of TPC. With the aid of the TOF detector in the STAR experiment, the analysis has been extended to the high transverse momentum region: ($0.4 < p_T < 2$ GeV/c). The new results (filled circles), observed in a wider p_T window, clearly show a non-monotonic behavior when the collision energy is below 39 GeV. Such an oscillation in high moments was predicted as signal for the possible critical point [51]. More high statistics data are needed, especially for energy below 20 GeV, in order to pin down the physics of the QCD critical point.

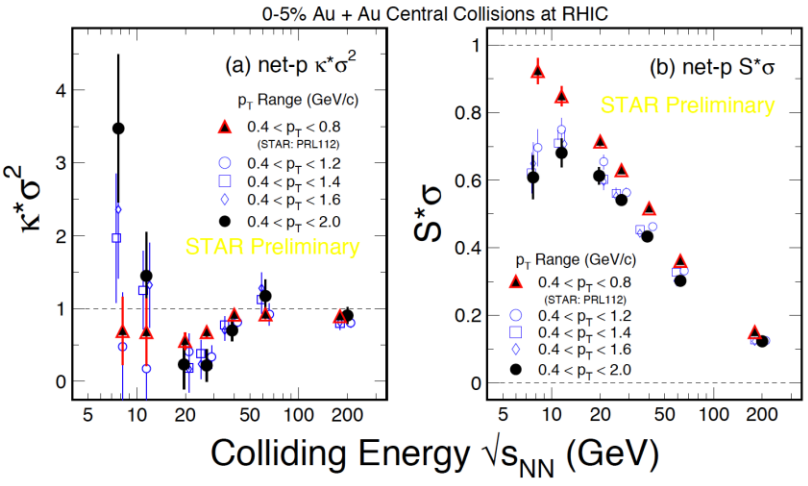

Figure 2-33: STAR preliminary results on energy and p_T dependence of mid-rapidity net-proton multiplicity distributions from top 5% central Au+Au collisions at RHIC. Data points on kurtosis and skewness are shown in plots (a) and (b), respectively [6]. All errors are statistical only. The results from a narrow transverse momentum region ($0.4 < p_T < 0.8$ GeV/c), shown as triangles, have been published earlier in Ref. [7].

It is worth noting that collisions at energies below 7.7 GeV will be important in order to fully cover the possible critical region. In this case, a high rate fixed-target experiment with clean particle identification will be more effective.

3 Run 15 Performance Report

3.1 Forward Meson Spectrometer and Preshower Performance

Determining the underlying physics process responsible for the large transverse single spin asymmetry at forward rapidities was one of the physics goals for the transversely polarized p+p run in 2015. The measurement of the direct photons A_N with the FMS will be extremely crucial to understand the Sivers-mechanism has any significant contribution to the forward A_N. Direct photons are a rare process. Therefore it is important to suppress backgrounds from leptons, hadrons and π^0 as much as possible. Therefore STAR instrumented the newly refurbished forward meson spectrometer (FMS), a lead glass electromagnetic calorimeter, with a preshower detector (FPS). (see Figure 3-1).

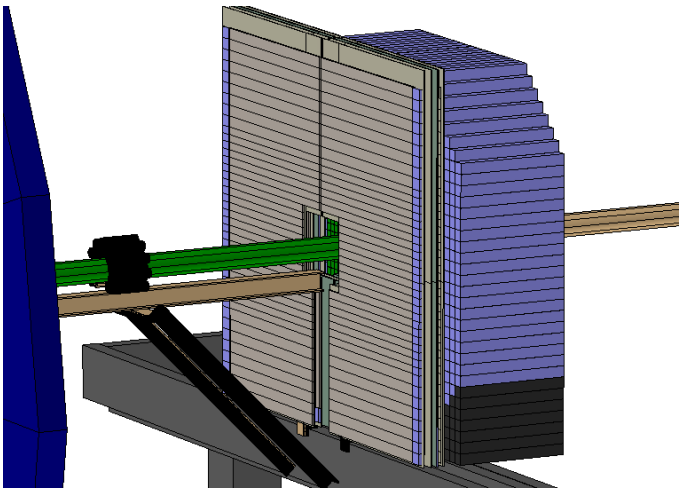

Figure 3-1: Sideview of the FMS and FPS as implemented in the STAR Geant detector model.

FMS:

Immediately after the run in 2013, the FMS lead glass was unstacked and the detector refurbished. Examination of the lead glass blocks revealed extensive damage by the beam, with a severe loss of light transmission in the glass. All lead glass cells were exposed to more than 40 hours of sunlight to "cure" the f-centers and bleach the glass to its original condition. Additionally, the phototube bases for 684 of the 788 large cells were experiencing gain jumps due to short circuits in a set of zener diodes in the last three stages of the amplification chain. Since these bases were integral with the PMTs themselves, this necessitated the removal of the original large cell PMTs, magnetic shields and mounting fixtures. These were replaced with new mounting fixtures and bases/PMTs (type EMI 9954) recovered from the decommissioned CDF barrel calorimeter at Fermilab. This work was completed in time for the polarized proton run in 2015. Figure 3-2 shows the performance of the calorimeter in reconstructing neutral pions over different regions of pseudorapidity for the p+p system. Although an isolation cone of 100 mrad has been imposed in the reconstruction, there is remarkably low background under the pion peak, as well as a clear eta signal for some pseudorapidity bins. It is worthwhile to note that these data were taken approximately 2/3 of the way through the 2015 run, after a significant amount of damage to the transparency of the lead glass had already accumulated.

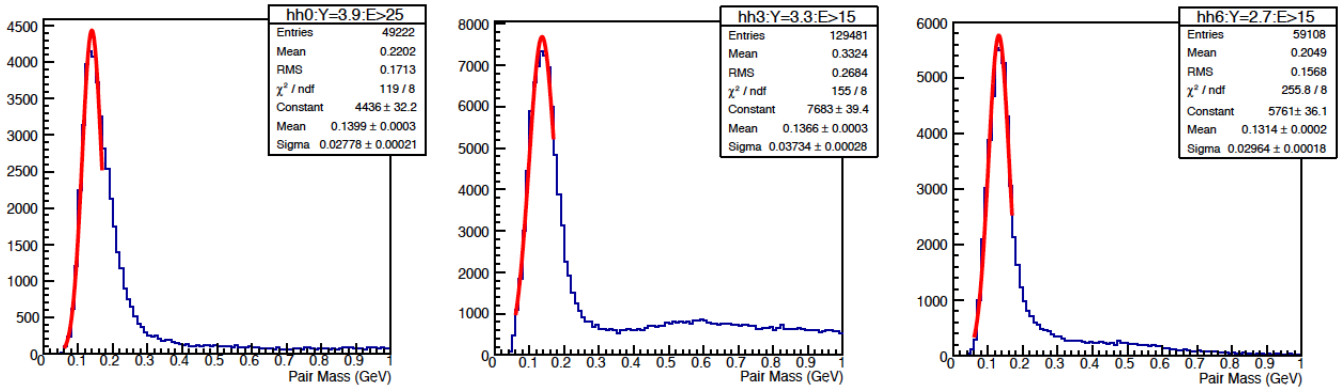

Figure 3-2: Reconstructed π^0 invariant mass for different rapidities reconstructed in the FMS during the polarized p+p run

Figure 3-3 shows the loss of gain in the FMS lead glass, as monitored by the LED system, as a function of pseudorapidity for three different integrated luminosity values. One can clearly see the effect of damage increasing for cells closer to the beamline. The expected damage due to all running in 2015 would correspond to approximately 200 pb^{-1} of delivered luminosity, which would give about 4 times the damage of the curve at 47 pb^{-1}. However, this method greatly overestimates the effect of the damage due to the fact that it integrates the loss of signal over the entire length of the lead glass bar, whereas photons from electromagnetic showers are generated most likely at positions closer to the shower maximum, which is 10-20 cm closer to the PMT. Again, the damage itself is distributed along the length of the lead glass according to the longitudinal shower profile; a fact verified by visual inspection of the damage from previous years.

At the end of the longitudinal p+p running, but before the beginning of the pAu running, it was determined that the effective loss of trigger rate in the FMS (for fixed energy thresholds) was approximately 50-70% in the worse areas, closest to the beamline. This corresponded to a change of gain in these cells of about 10-20%. For the p-Au running, this we increased the voltages in this region by approximately 1-2% in order to correct for the change in gain and the reduction in trigger rate. All indications are that the trigger rate/gain has been completely restored and that there is only a small effect (thus far) on the resolution of the pion mass peak, estimated at an increase of about 5% (absolute).

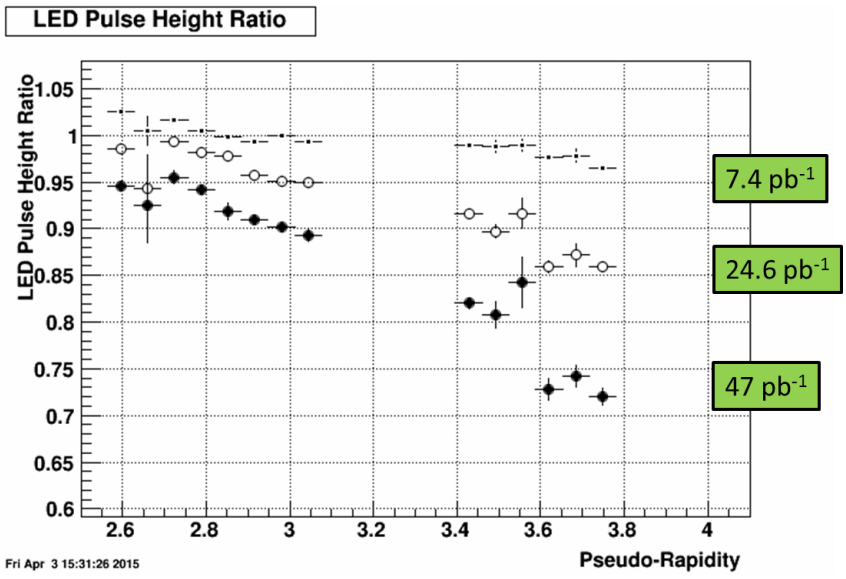

Figure 3-3: loss of gain in the FMS lead glass, as monitored by the LED system, as a function of pseudorapidity for three different integrated luminosity values.

FPS:

The STAR preshower detector in front of the FMSaim is to distinguish photons, electrons/positrons and charged hadrons. This detector is comprised of two layers of perpendicularly arranged scintillator slats (PS1 and PS2), followed by a lead converter and a subsequent third layer of scintillator slats (PS3). PS1 and PS2 are used to identify neutral particles (photons) from charged particles (hadrons and electrons), while PS3 after the converter is separating electromagnetic showers (photons and electrons) from charged hadrons. The preshower detector is located in front of the FMS at a little less than 7 m downstream of the nominal interaction point in STAR and covers a transverse area of about 2x2 m^2 with a 40x40 cm^2 cutout in the center for the beam pipe. The preshower layers are divided into quadrants. The detector is segmented to ~80 scintillator slats per layer, and the granularity of the array is matching that of the FMS. Figure 3-4 shows first correlations of a high tower in the FMS with individual scintillator strips in quadrant 1 of layer-3 in the preshower.

Due to up to 400 gauss of magnetic field from the STAR solenoid magnet, SiPMs (MPPC) were chosen for the readout instead of conventional PMT. The scintillation light from a scintillator slat was read out by two 3x3mm Hamamatsu S12572-050P (PS1 & PS2) and S12572-025P (PS3) MPPC (SiPM), which are mounted on a FEE board and attached to light guides at the end of the scintillator slat. Figure 3-5 shows a MIP peak for one scintillator strip 4 in quadrant 1 layer-1 at the beginning of Run-15 (blue) and close to the end of the polarized p+p run (red). The separation between the pedestal and the MIP peak is excellent.

As expected the leakage current of the SiPMs has been rising from the beginning to the end of the polarized p+p run as clear sign for radiation damage of the SiPMs through low energetic (~MeV) neutrons. The online monitoring has not shown any strong degradation of the performance of the SiPMs. Detailed offline studies of the detector performance will allow to learn much more about the long term behavior of SiPMs, critical knowledge for future RHIC detector upgrades and EIC detector studies.

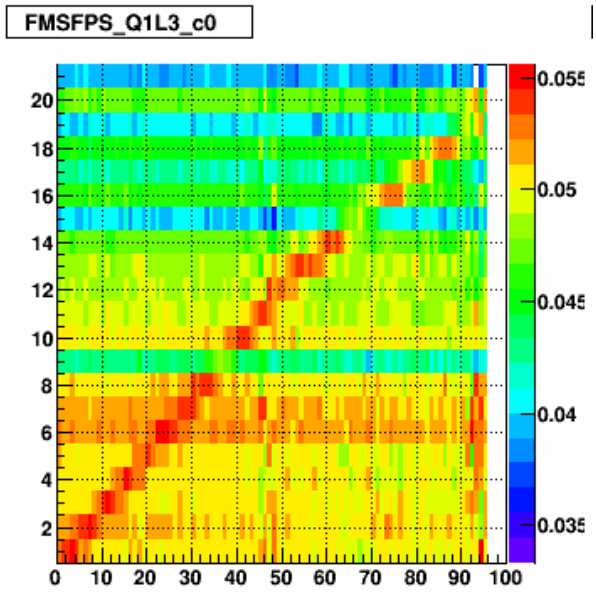

Figure 3-4: Correlation of a high tower in the FMS

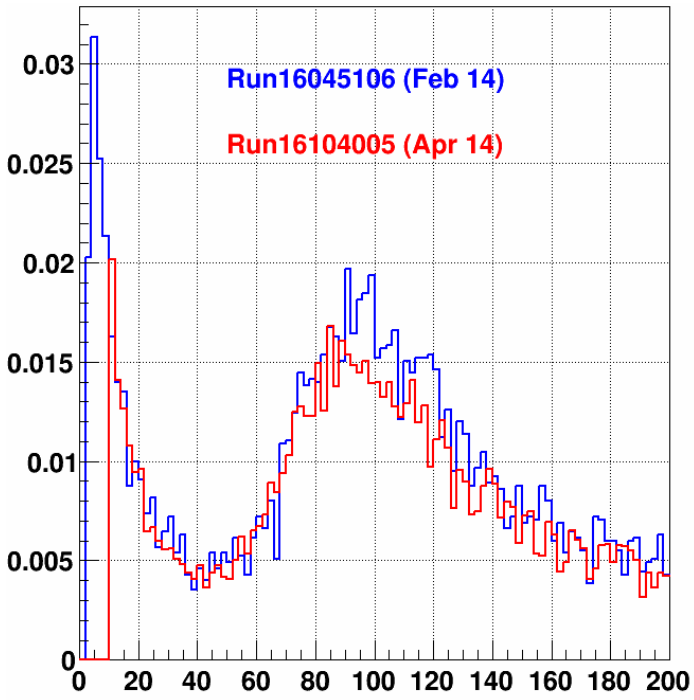

Figure 3-5: MIP peak in scintillator strip 4 in quadrant 1

with individual scintillator strips in quadrant 1 of layer-3 in the preshower. A clear correlation is observed.

layer-1 at the beginning of Run-15 (blue) and close to the end of the polarized p+p run (red). An excellent separation to the pedestal is seen.

The excellent detector performance of the FMS and FPS was paired with an excellent performance of RHIC, which allowed to reach all the transverse luminosity and figure-of-merit goals for Run-15 (see Figure 3-6).

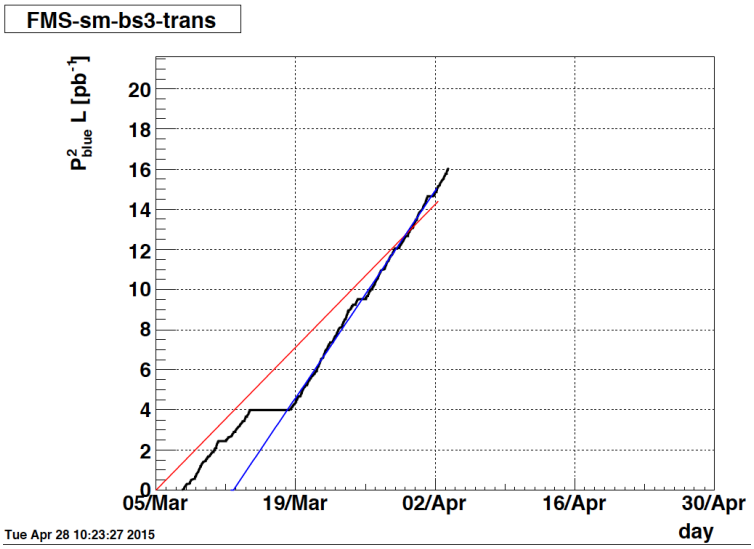

Figure 3-6: The accumulated luminosity weighted by the beam polarisation squared (shown by the black curve) sampled by the FMS.

3.2 Dataset for inclusive jet and dijet A_{LL}

The final results, obtained in Run-9, on the double-spin asymmetry A_{LL} in inclusive jet production at $\sqrt{s}$ = 200 GeV from 20 pb^{-1} sampled with 58% average beam polarization are shown in Figure 3-7 bottom panel. Although these data provides the strongest constraints to date on $\Delta G(Q^2)$, they are still statistically limited, motivating additional running at sqrt(s) = 200 GeV. The solid dark lines indicate the statistical power of the data collected during the 2015 longitudinal polarized pp run.

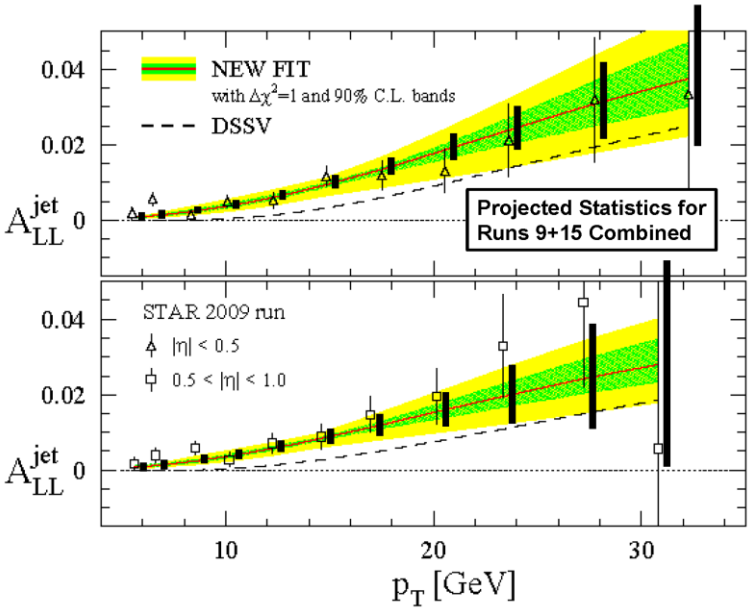

Figure 3-7 Double Spin Asymmetry measurement from inclusive jets with projected statistics for run 9 and run 15 combined.

We have completed the longitudinal spin run in run 15. Figure 3-8 shows the actual achieved integrated luminosity and figure of merit (FOM) for the inclusive jet double spin asymmetry measurement (A_{LL}). The integrated luminosity exceeds our request while the FOM is about 60% of our target goal. Figure 3-7 top panel shows the updated projection of A_{LL} measurement for the combined run 9 and run 15.

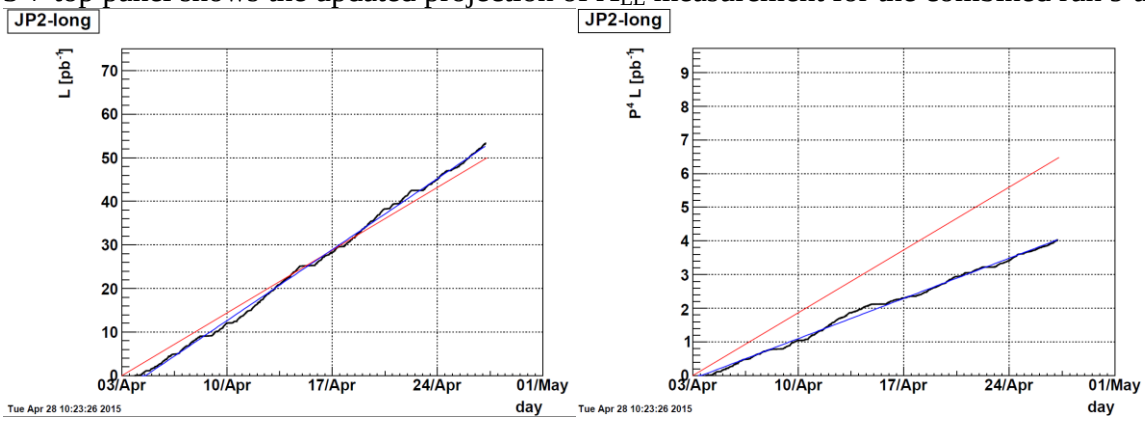

Figure 3-8 Left: Integrated luminosity as a function of RHIC operation days during the longitudinal p+p run. Right: the integrated FOM (figure of merit) for the inclusive jet double spin asymmetry (A_{LL}) measurements. Red line is the linear projection to targeted goals; blue line is that for the actual achievement; black histogram is the actual daily performance.

3.3 Roman Pot Performance

The Roman Pot (RP) system is the main detector system used to identify and characterize diffractive process at STAR through a detection of the forward protons, which stay intact after the collision took place.

The RP system at STAR was utilized for successful data taking in Run9 and then reconfigured and moved to a new location, closer to the interaction region between DX and D0 magnets, to allow concurrent running with the rest of the RHIC program. To accomplish that a new vacuum chamber at that new location had been designed and fabricated to accommodate the RP system.

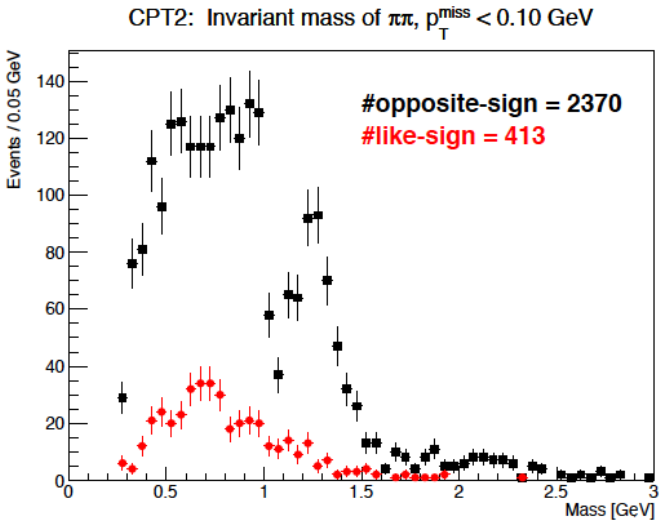

Figure 3-9: Invariant mass of the p+p- system in the CEP process, the cut on pt^{Miss} < 0.1 GeV/c

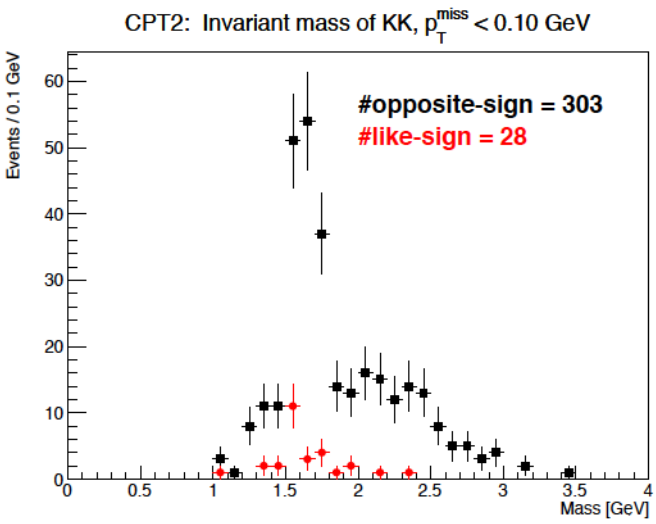

Figure 3-10: Invariant mass of the KK system in the CEP process, the cut on ptMiss < 0.1 GeV/c

The new system (RP Phase-II*) has been successfully commissioned in Run 15 and is being used for data taking. This gave the STAR experiment the unique opportunity to detect the protons scattered at small angles in the elastic scattering process and a diffractive Central Production (CP) process p+p=>p+X+p, where the system X is measured in the STAR TPC. Tagging on those protons, detected in the Roman Pots, selects processes in which the protons stay intact and the exchange has the quantum numbers of the color singlet, thus enhancing the probability of measuring reactions where colorless gluonic matter (Pomeron) dominates the exchange. Two of the gluons in the Double Pomeron Exchange (DPE) process could merge into a mesonic bound state without a constituent quark, a glueball, in the CP process. Detecting forward protons allows determining exclusivity of the process by balancing the momentum of the protons and the systems X measured in the STAR TPC.

Given this new RP setup, it is possible to acquire large data samples of central production events, which are necessary for the searches for the glueball and exotic particle production. The new RP system has been used to collect over 800M triggers including 600M CP trigger events in p+p at $\sqrt{s}$=200 GeV. The data sample is expected to yield a high statistics sample of exclusive centrally produced system decaying into $\pi^+\pi^-$, K^+K^- and $\pi^+\pi^+\pi^-\pi^-$. The preliminary study shows clearly identified scalar and tensor f mesons in the CEP process in $\pi^+\pi^-$, K^+K as shown in the invariant mass distribution (Figure 3-9 and Figure 3-10), confirming the detector system and triggers perform as designed. The preliminary estimates are that we should have about 80K events in into $\pi^+\pi^-$ mass distribution in the region of interest with M_X > 1 GeV/c^2 for partial wave analysis to determine quantum numbers of the resonant states.

The other data samples collected utilizing the RP systems in p+p collisions include spin-dependent elastic, single diffractive, exclusive vector meson production and searching for an exotic charmonium-like meson state in photo-production.

The 5 weeks of p+Au running in Run15 is expected to give a data sample with tagged protons in diffractive photo-production (Au+p or p+Au) to study GPD and t-dependent source size with exclusive vector meson production.

3.4 The Heavy Flavor Tracker and Muon Telescope reference data performance and projections

The HFT sub detectors of the IST and the SSD were prepared for run-15 in the fall of 2014. The status of IST sensor is that more than 94% of the sensors are active, and with essentially the same performance as in run-14. The PXL detector was installed in January. The detector was the run-14 refurbished detector with Aluminum cable ladders on the inner layer for improved pointing resolution over run-14. The Mass Termination Boards were modified for stable ADC reading allowing lower Latch-Up (LU) thresholds. The protection against latch-up damage was improved reducing the level to - adjust thresholds and supply voltages. New alarms were added to protect the PXL detector from potential beam injection failures, and a new temperature interlock was added in case of high temperature or low airflow in cooling ducts.

The environment under which PXL was operated was quite similar to the Au+Au in terms of the hit multiplicity per sensor which was 300-400 for inner sensors and 60-70 for outer at maximum luminosity. The additional LU protection added about 3% dead-time at the highest luminosity where HFT was included in the runs. A small number of sensors were damaged and was at the end of the pp run about 4 sensors in the inner layer, and 4 which were damaged in run-14 and one complete ladder in the outer layer (10 out of 300 sensors). The SSD was operated in a mode that reduces the noise seen at high rates by introducing a fixed dead time of 1 msec. This still allows to take minimum bias data with all 3 HFT detectors, PXL, IST and SSD at the rates required to achieve the physics goal for the minimum bias program.

The HFT was typically not included in the first couple of runs until ‘safe’ luminosity levels were reached but then allocated bandwidth that allowed for running up to 800 Hz of the total available bandwidth of ~1800 Hz possible for data events where the TPC is read out. A typical distribution of rates vs. time in store is shown in Figure 3-11.

The goal for run-15 was to record 500 M minimum bias events with a vertex of $|V_z| < 5$ cm. The purity of the trigger was about 50% so the number of triggers to be collected was 1,000M. As illustrated in the Figure 3-12 this was achieved and the goal exceeded which compensated for the loss of sensors i.e acceptance during the run.

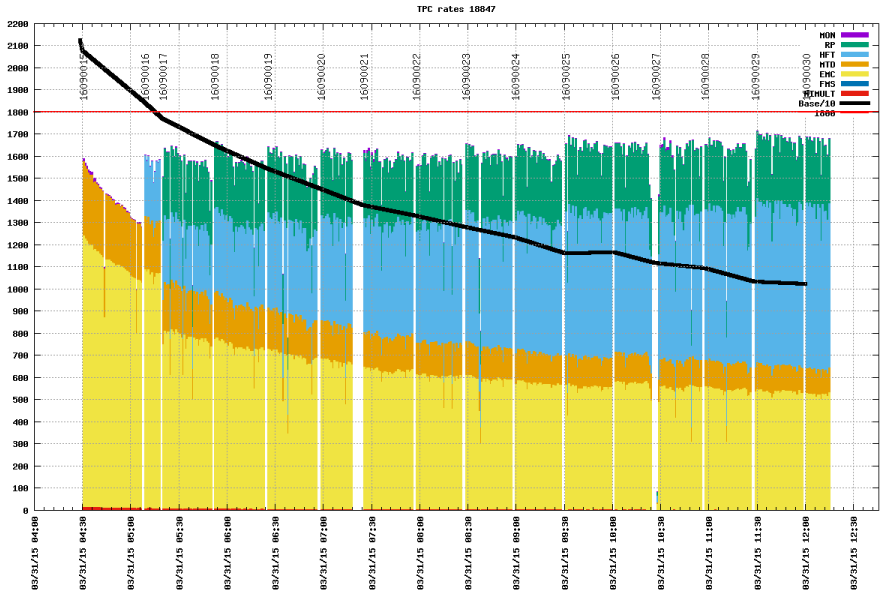

Figure 3-11: Typical distribution of trigger rates throughout a normal store. The minimum bias HFT data are shown in light blue.

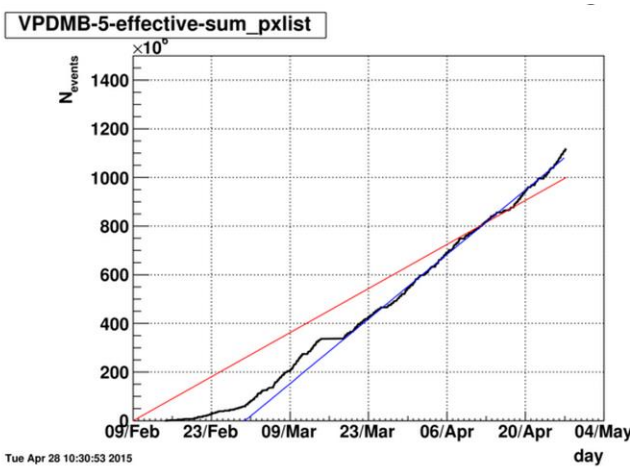

Figure 3-12: Accumulated number of trigger for the HFT minimum bias dataset in the pp 200 run.

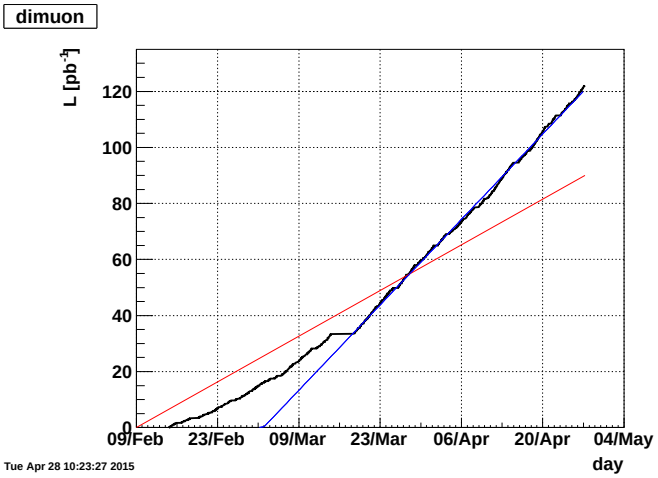

Figure 3-13: The accumulated luminosity (shown by the black curve) sampled by dimoun trigger for quarkonium versus time.

The Muon Telescope Detector system ran very smoothly this year. We took single-muon, dimuon and μ-e triggers in p+p collisions at 200 GeV. With the same trigger algorithms in place, we successfully limited our data acquisition rate for these three triggers combined around 200 Hz. The luminosity sampled by the dimuon trigger exceeded our Run 2015 goal for 200 GeV p+p collisions. Figure 3-13 shows the accumulated luminosity (shown by the black curve) sampled by dimoun trigger for quarkonium versus time. By the end of the p+p 200 GeV run, we exceeded our Run 2015 goal for quarkonium measurement, as indicated by the blue curve compared to the red one.

4 Run 16 Request

4.1 Au+Au $\sqrt{s_{NN}}$= 200 GeV

4.1.1 D^0 and Λ_c request Au+Au $\sqrt{s_{NN}}$= 200 GeV

In Run16, we request a long Au+Au 200 GeV run to carry out the systematic measurements of heavy flavor hadrons with HFT and MTD. In particular, we are aiming for measurements of Λ_c baryon and bottom hadrons through J/Ψ as well as semi-leptonic decay channels. We request a Au+Au 200 GeV run to collect 2B minimum bias "good" events and > 1 nb^{-1} sampled luminosity with EMC HT and di-muon triggers within the HFT acceptance (|Vz|<6cm) to perform these measurements.

The HFT-PXL detector planned for Run16 will be equipped with the Aluminum (Al) cable for inner ladders, as the case for run-15, while in Run14, most inner ladders were using Copper (Cu) cables. The material budget for an Al-cable ladder is about 0.37%X0 compared to 0.52%X0 for a Cu-cable ladder. This will significantly reduce the contribution from multiple coulomb scatterings to the pointing resolution, especially for low momentum particles, and thus improve the significance of reconstructed D^0 mesons at low p_T. Figure 4-1 shows the significance ratio between the Al-cable and Cu-cable ladders for D^0 mesons as a function of p_T. The improvement in the significant is about a factor of 1.6 for 1 GeV/c D^0 mesons. In other words, the Figure-Of-Merit (FOM) statistics improvement with the same number of events in Run16 will be a factor of 2.5 for 1 GeV D^0 mesons.

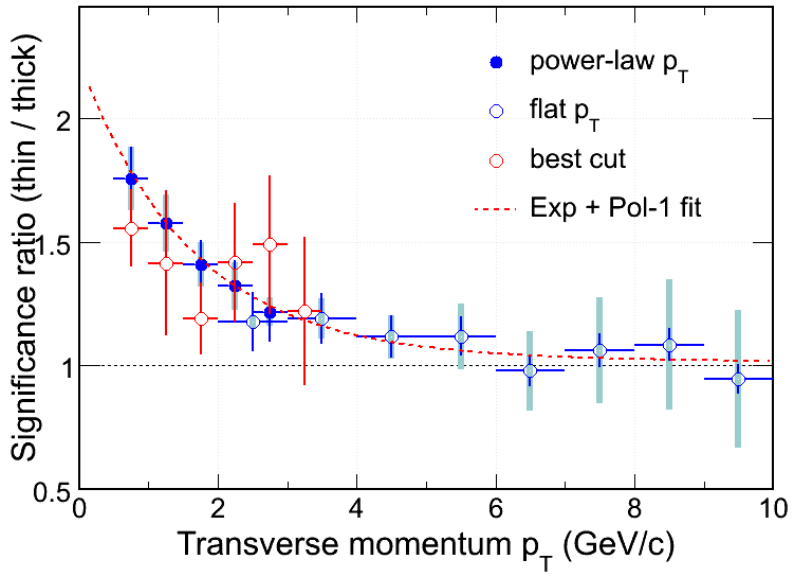

Figure 4-1 The ratio of D^0 meson significances between the Al-cable ladder (thin) and the Cu-cable ladder (thick) as a function of D^0 p_T from simulation

In addition, in Run16, we expect to have the SSD subsystem to participate in the data taking for the full 200 GeV run period as was done for the Run15, while we don't have the SSD in the major HFT data collected in the current Run14. The SSD will improve the track matching and reduce the ghosting rate for the TPC tracks associating with the PXL hits. The improvement is about 10% for the single track efficiency with the additional SSD layer, thus effectively 20% in the D^0-mesons reconstructed with two charged tracks.

We request to collect 2B minimum bias "good" events in Run16. The effective FOM increase considering the above detector configuration improvement is about a factor of 6 for low p_T D^0 when

comparing Run16 with Run14. This is a significant improvement that will allow us to perform more differential studies on charmed hadron production including charm correlations. In the meantime, the improved statistics as well as the pointing resolution for low momentum tracks will make the Λ_c measurement feasible ($c\tau$ of Λ_c ~ 60 μm). Figure 4-2 shows the estimated statistical errors on the Λ_c/D^0 enhancement factor ($R_{cp}(\Lambda_c)/R_{cp}(D^0)$) for two scenarios: no enhancement and the same enhancement as Λ/Ks based on the 2B minimum bias data plus an additional 250M central triggered dataset. With these datasets, we will be able to distinguish these two scenarios with a significance of more than 3σ.

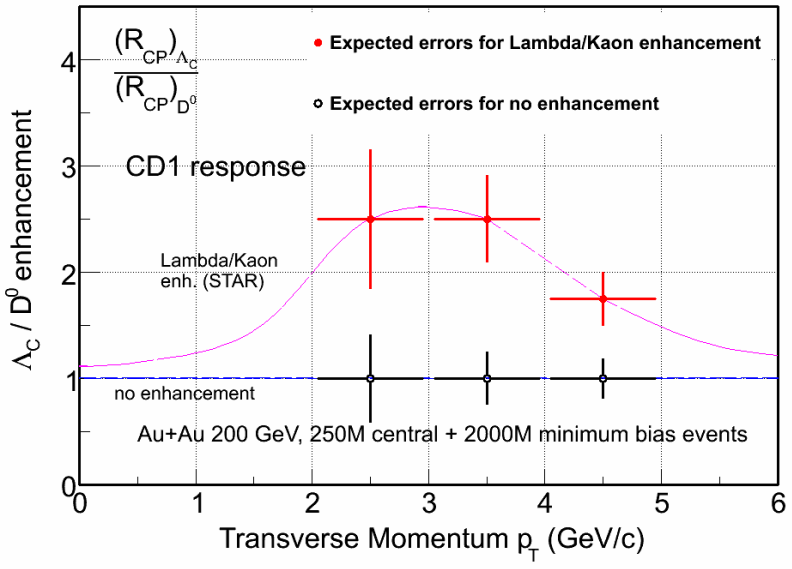

Figure 4-2: Statistical error estimation on the Λ_c/D^0 enhancement factor ($R_{cp}(\Lambda_c)/R_{cp}(D^0)$) measurement for two scenarios: no enhancement and the same enhancement as Λ/Ks with 2B minimum bias events and additional 250M central triggered events in Au+Au 200 GeV.

Another physics goal in Run16 is to sample sufficient luminosity ($1nb^{-1}$ within |Vz|<5cm) with the HFT for the measurements of bottom production. We expect the 56MHz RF will be fully operational in Run16. This will improve the luminosity fraction within |Vz|<5cm from 8% so far in Run14 to about 12% in Run16. With the optimized beam luminosity profile, assuming 60% uptime for the STAR trigger and DAQ and the HFT can take at least 80% of the total available luminosity in the store, we should be able to reach the goal of $1nb^{-1}$ sampled luminosity within |Vz|<5cm within 14 weeks. The physics datasets will be collected through the dimuon trigger from the MTD to measure the displaced J/psi's from bottom decays and the single HT trigger from the EMC to measure the single electrons or di-electrons to form the displaced J/Ψ's. The B->J/Ψ signal is estimated to be 100 with the barrel HT2 triggered data set. Combined with the di-muon trigger from the MTD detector for low p_T region, we would be able to make the first measurement of displaced J/psi from bottom decays over a broad p_T region.

We use pseudo-cτ which serves as a proxy of the true B meson cτ. It is defined as $\vec{L}_{xy} \cdot M_{J/\psi}/|\vec{p}_T|$, where $\vec{L}_{xy} = \vec{L} \cdot \vec{p}_T/|\vec{p}_T|$, $\vec{L}$ represents the path from collision vertex to B meson decay point, $M_{J/\psi}$ and p_T are the mass and transverse momentum of J/ψ , respectively. The p_T of the J/ψ is required to be larger than 1.25 GeV/c for a reliable extraction of the signals. Figure 4-3 shows the pseudo-cτ distributions for prompt and non-prompt J/Ψ using the full GEANT simulation with HFT included. One can see the separation power with HFT between these two components. Figure 4-4 shows the projection on the non-prompt J/Ψ R_{AA} with the recorded Run15 p+p 200 GeV dataset and the request $1nb^{-1}$ Au+Au dataset from Run16. This offers us the first measurement of the bottom suppression factor through this channel with approximately 3σ distinguishing power from unity.

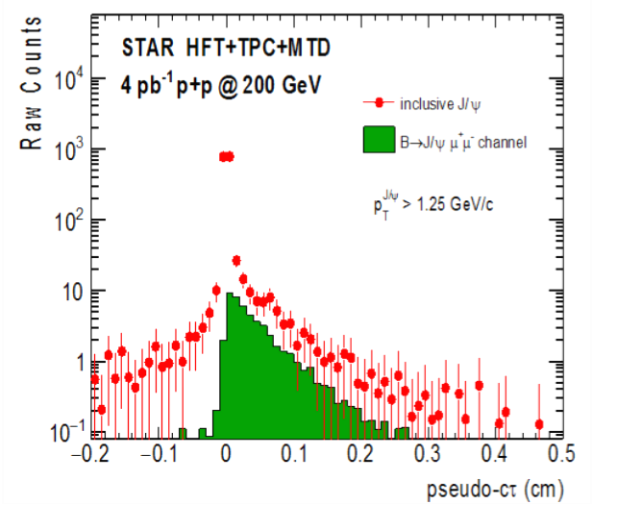

Figure 4-3: Simulated pseudo- cτ distributions with HFT for prompt J/Ψ's and displaced J/psi from bottomed hadron decays.

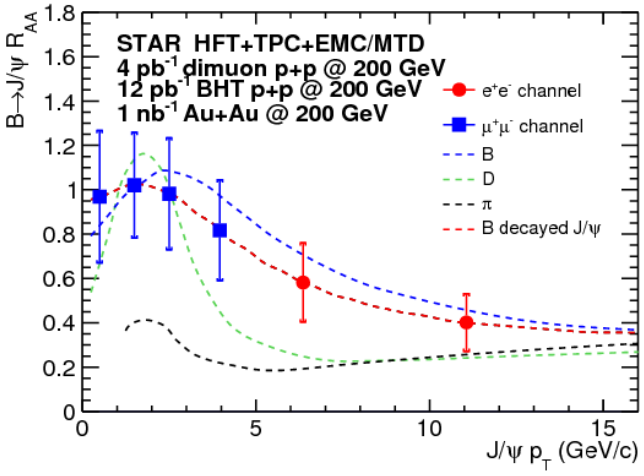

Figure 4-4 Projection for B->J/psi R_{AA}

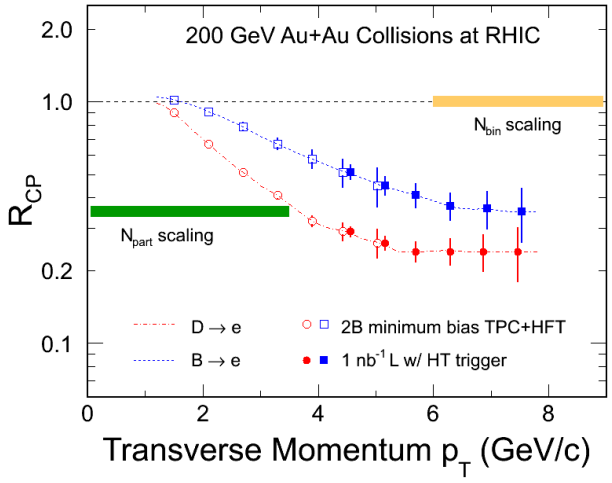

Figure 4-5 Projected statistical uncertainties for the R_{CP} of electrons from charm and bottom decays separately with HFT. The estimate is based on 2B minimum bias event sample plus 1 nb^{-1} sampled luminosity with HT triggers collected within $|V_z|<5$cm.

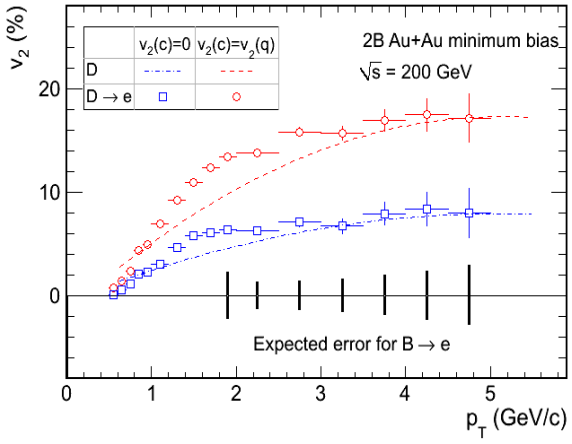

Figure 4-6 Projected statistical uncertainties for charm and bottom decay electron v_2 with 2B minimum bias events.

With the request 2B good minimum bias and $1nb^{-1}$ AuAu datasets, we can also carry out the measurement of charm and bottom decay electrons through the impact parameter method. Figure 4-5 shows the projection on the R_{CP} of charm and bottom decay electrons separately with HFT using the requested dataset in Run16. In Figure 4-6, we show there is a good possibility to measure the v_2 of bottom decay electrons at low and intermediate p_T through this method.

4.1.2 Quarkonia request for Au+Au √s= 200 GeV

A large-area and cost-effective Muon Telescope Detector (MTD) at mid-rapidity was fully installed at STAR for Run 14. The Time-of-Flight system it utilizes is based on multi-gap resistive plate chambers with precise timing and hit position. The technology and method are different from the conventional muon detector, consisting of a sandwich of tracking stations, trigger detectors, and absorbers, in high-energy particle and nuclear physics experiments. Among many exciting perspectives, we will be able to collect a large sample of J/ψ events for spectra and elliptic flow measurements (Figure 4-7 left plot), to separate different Upsilon states (Figure 4-7 right plot) with a clear advantage over electron decay channels due to the reduced Bremsstrahlung radiation and Dalitz decay background, and to provide a unique measurement of $\mu-e$ correlations from heavy-flavor decays.

The open charm production rate is high enough at RHIC that the coalescence process becomes relevant for charmonium production. Knowledge of the total production cross-section for charm quarks is also essential as a baseline for J/ψ measurements. From a precise measurement of the spectra and the production ratios of charm hadron states, we will be able to extrapolate to the total yield for charm quark production. A unique advantage of STAR due to its full azimuthal coverage is the detailed studies of charm-charm correlations. The angular correlation will be modified in heavy ion collisions due to the interactions between the heavy quarks and the medium. Measurements of the direct D-Dbar and e-μ correlations are sensitive to the effect of 'partonic wind' on charm quark correlations in high-energy nuclear collisions and the thermalization in high-energy nuclear collisions. Meanwhile, the semi-leptonic decays of heavy-flavor pairs are important component of dilepton spectra. Only such correlation measurements can provide experimental tool to separate QGP thermal radiation from the heavy-flavor decays in the dilepton spectra.

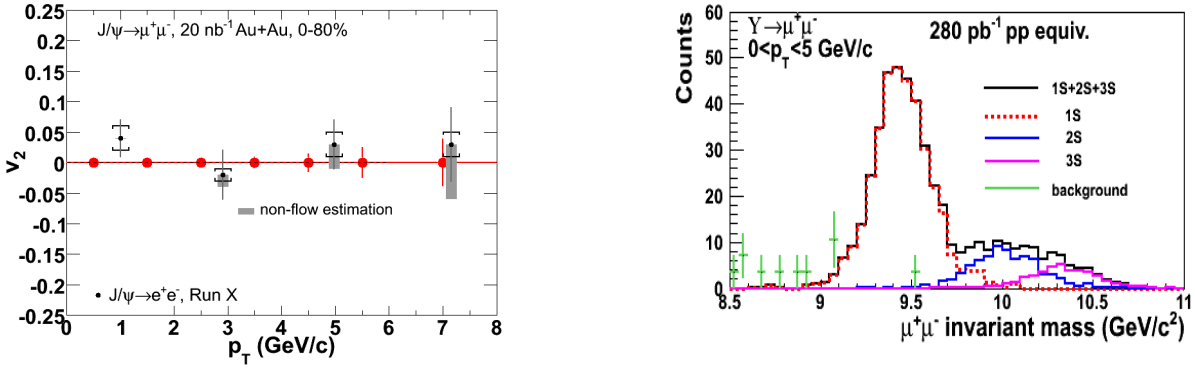

Figure 4-7: (Left) Projection of J/psi (from muon pairs) v_2 measurement from MTD. Data with error bars are from [13]. (Right) Projected Upsilon line-shapes of the 1S, 2S and 3S states and backgrounds measured in the MTD from 280 pb^{-1} Au+Au collisions at RHIC.

Measurements of the in-medium dissociation probability of the different quarkonium states are expected to provide an estimate of the initial temperature of the system. Dissociation of quarkonium in a thermal QCD system would ultimately provide evidence of color screening and free quarks. The J/ψ(1S) is the lightest and most abundantly produced quarkonium state accessible in experiment. However, significant decay contributions from excited states and the final state production via coalescence complicate the situation. Υ(1S, 2S, 3S) states provide a natural thermometer since they are bottomia of three consecutive states. The ground state has a binding energy of 1.1 GeV and is way above the temperature reached at RHIC. However, the 2S and 3S states have binding energy at 0.54 and 0.2 GeV, respectively, and can be dissolved at RHIC. MTD provides the measurements allowing separate these three states at RHIC through the di-muon channel. The separation is made possible by

MTD with reduced Bremsstrahlung radiation and enhanced trigger capability. Comparison of low-p_T J/ψ and Υ yields at RHIC and LHC and study of the J/ψ azimuthal anisotropy could quantitatively further constrain the model interpretation. These requirements call for a comprehensive experimental quarkonium program at RHIC. The combined measurements by HFT and MTD from STAR offer a unique and comprehensive heavy flavor program to explore these exciting physics opportunities.

A transition to a different state is not only characterized by the increase of temperature, but also by the changes of degree of freedom and symmetries. The long-sought signature of such a transition is chiral symmetry restoration. The experimental procedure of detecting signature related to the restoration is to study the in-medium dilepton decay of vector mesons. The spectral function from the remnant hadronic structure should transit to a smooth spectrum of QGP thermal radiation with increasing temperature and density. Great progress has been made in the last decade at SPS and RHIC. It has been experimentally demonstrated that the hadronic spectral function has been greatly modified in the medium. However, a quantitative assessment of its temperature dependence is absent. This requires consistency between thermal radiation at high temperature (dominant at RHIC) and modified hadronic decay (dominant at SPS) close to the phase transition. At RHIC energies and above, such dilepton measurements are hindered by the dominant "irreducible" background from semileptonic decay of open heavy-flavor pairs. STAR has demonstrated its unique capability of di-electron measurement with the combination of large-coverage TPC, EMC and TOF. With HFT and MTD upgrades, contribution to the dilepton spectra from the open heavy-flavor pair correlation is measurable with D-Dbar and e-μ correlation measurements all at mid-rapidity.

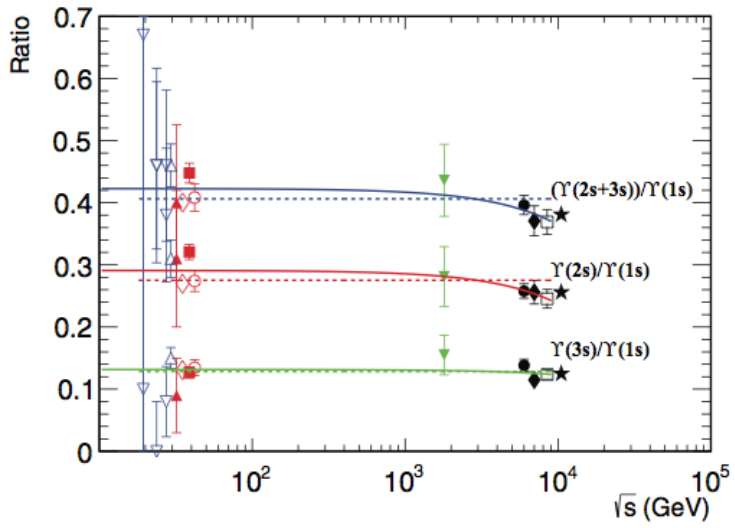

Figure 4-8: Collision energy dependence of the yield ratio of Upsilon states in p+p, p+pbar and p+A collisions. The solid and dashed lines are fit curves.

Run 16 requests: Run 14 kicked off the physics program with the full MTD. The primary focus of this MTD run is on Quarkonia at RHIC energies, using muons to remove the issue of Bremsstrahlung tails in their line-shapes. This is most important in the separation of the Upsilon 1S from the (2S, 3S) states, all three of which are expected to be suppressed differently in the QGP. We sampled 11 nb^{-1} 200 GeV Au+Au luminosities in Run 14 for Upsilon measurements. We would like to request to sample 9 nb^{-1} 200 GeV Au+Au luminosities in Run 2016 to complete the goal. Figure 4-7 shows a projected line-shape with the MTD, showing that the 1S can be clearly separated from the 2S+3S, while the 2S and 3S can be separated statistically assuming a large statistics sample and good control over the line-shape. These measurements require a large integrated luminosity driven by the requirement in p+p reference data. Table 4-1 shows an estimate for the required luminosity for measurements of the 2S+3S and the 3S separately. We have investigated an alternative approach in

obtaining the reference. Many experiments have measured the Upsilon yields and ratios of the three states. We have collected all the experimental results and survey the ratios of $\Upsilon(2S)/\Upsilon(1S)$, $\Upsilon(3S)/\Upsilon(1S)$ and $\Upsilon(2S+3S)/\Upsilon(1S)$. Figure 4-8 shows the results as a function of beam energy for all the p+p, p+pbar and p+A results. A small energy dependence of these ratios are observed within the broad collision energies. The solid line shown in the figure is a linear fit. The dashed line is a constant fit. The linear fit gives a better $\chi 2$/NDF, where NDF is the number of degrees of freedom; therefore we select the linear fit results to determine the nominal values for p + p collisions at $\sqrt{s}$ = 200 GeV. The differences between these two fit results for 200 GeV p + p collisions are considered to be the systematic uncertainties.

$$\Upsilon(2S)/\ \Upsilon(1S) = 0.290 \pm 0.007\ (\text{stat.}) \pm 0.014(\text{syst.})$$
$$\Upsilon(3S)/\Upsilon(1S) = 0.131 \pm 0.005\ (\text{stat.}) \pm 0.003(\text{syst.})$$

The ratios are: for p + p collisions at $\sqrt{s}$ = 200 GeV. Note that the error bars from these measurements are much smaller than that achievable at RHIC. Figure 4-9 shows the projected R_{AA} for all the three separated states, taking into account the p+p reference from the average of the world data.

Collision system	**Mini. lumi. for 10% uncertainty on $\Upsilon(3S)$**	**Mini. lumi. for 10% uncertainty on $\Upsilon(2S+3S)$**
p+p 200 GeV	420 pb^{-1}	150 pb^{-1}
p+p 510 GeV	140 pb^{-1}	50 pb^{-1}
Au+Au 200 GeV	10 nb^{-1}	3.8 nb^{-1}

Table 4-1: Estimated luminosities for $\Upsilon(2S, 3S)$ measurements.

The STAR MTD allows for the measurements of electron-muon correlations, where the electron and muon are both measured at mid-rapidity. The dominant source of these correlations at intermediate mass is from the decay of charm-anticharm pairs, since in thermal production of dilepton pairs electrons are paired with positrons, and muons with antimuons. Figure 4-10 shows the existing minimum bias and central di-electron pair invariant mass distributions normalized by N_{part}. According to the cocktail, the correlated charm contribution dominates the contribution in the intermediate mass range from 1 to 3 GeV/c^2. In this figure, the correlated charm contribution is from PYTHIA, assuming no decorrelation in medium and rescaled to match a charm cross section of 0.8mb. Both of these assumptions introduce a large uncertainty, due to the possibility of charm energy loss and decorrelation in the medium, both of which would decrease the contribution in this mass range. There are hints of suppression in central as compared to minimum-bias data. This uncertainty prevents the extraction of any signal from QGP radiation, which in the absence of decorrelation is approximately an order of magnitude below the charm contribution. The only way to make progress is to directly measure the correlated charm contribution in heavy ion collisions: electron-muon correlations provide one method to do so.

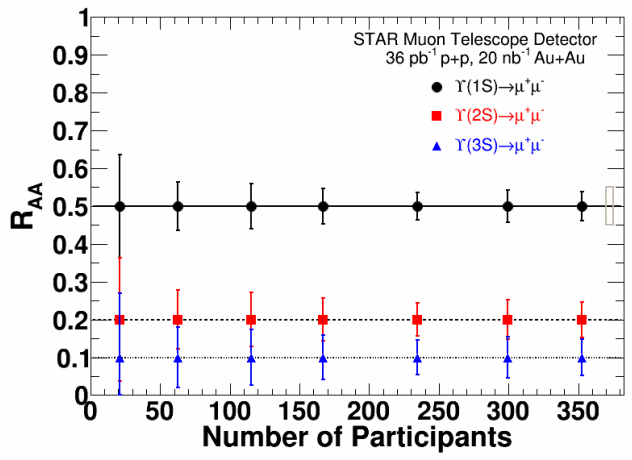

Figure 4-9: Projected errors on R_{AA} of Upsilon 1S+2S+3S measured by the STAR MTD from the 20 nb^{-1} Au+Au and 36pb^{-1} p+p collisions (reference data). The p+p reference data for inclusive Upsilon yield was from run15 with the actual dataset in tape taking into account sampled luminosity and VPD trigger efficiency.

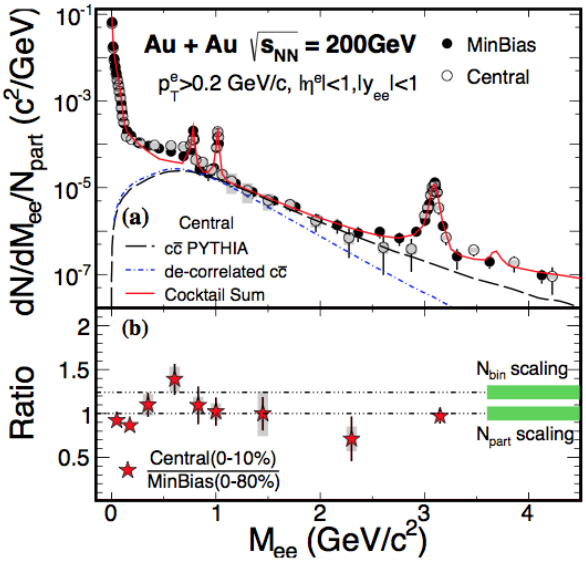

Figure 4-10: Central and minimum bias di-electron invariant mass distributions normalized by N_{part}, from Run 10 Au+Au collisions. Black line shows the cocktail contribution from fully correlated charm-anticharm pairs, assuming a cross section of 0.80 mb. Blue line shows the contribution if charm is angularly decorrelated and momentum distributions softened to match non-photonic electron R_{AA}.

In Run 12 p+p collisions at √s =200 GeV STAR established that we can trigger on electron-muon pairs with one leg in the MTD and the other leg in the Barrel Electromagnetic Calorimeter (BEMC) at a transverse energy threshold of 1.9 GeV. This was a very clean trigger, running at prescale 1 with a very low rate (~10's of Hz) in the p+p collisions. The total sampled luminosity in run 12 was 23 pb^{-1}. However, in Run 14 Au+Au collisions at √s =200 GeV, the trigger on transverse energy threshold of 1.9 GeV was not effective. Instead, we triggered on electron-muon pairs with one leg in the MTD and the other leg in the BEMC at a transverse energy threshold of 3.0 GeV. We sampled 2.6 nb^{-1} 200 GeV Au+Au luminosities in Run 14 for this trigger, which will enable us to do first electron-muon azimuthal correlation measurements in heavy ion collisions. In Run 2016, we can also sample a fraction of the delivered luminosity with a central trigger, which enables the kinematic cuts to be relaxed to allow for lower energy electrons, identified via the ToF and TPC dE/dx.

Figure 4-11 plot shows the projected uncertainty in the electron-muon invariant mass distribution for 250 M central 0-10% Au+Au events, assuming the PYTHIA fully correlated charm contribution. For comparison, the black histogram shows the maximal reduction in the distribution, assuming full angular decorrelation and suppression of the charm singles distribution following measured non-photonic electron R_{AA}. The proposed measurement can clearly distinguish this extreme scenario from the fully correlated PYTHIA scenario. The downside of such triggered datasets is that they select specific regions of the invariant mass vs. p_T plane. The resulting e-μ correlation in the invariant mass distribution has different kinematic acceptance in comparison to that of the dielectron pair. A direct subtraction to obtain the thermal radiation at the intermediate range is not possible with detailed simulations.

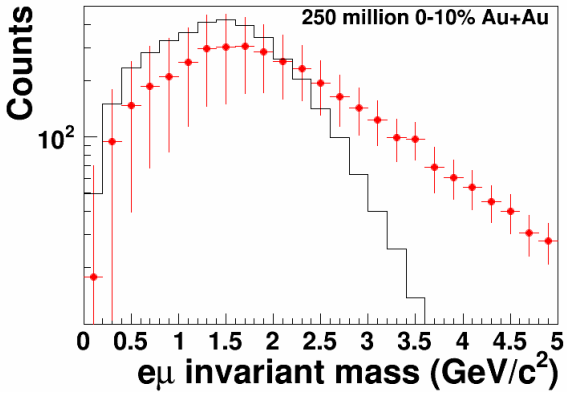

Figure 4-11: Projected electron-muon invariant mass distribution from 250M top 10% central Au+Au events with full MTD coverage. Red points assume full correlation and momentum distributions from PYTHIA while the black histogram assumes full decorrelation and softening of the charm momentum distribution to match non-photonic electron R_{AA}.

4.1.3 Gamma-jet for Au+Au $\sqrt{s}$= 200 GeV

The γ_{dir}-jet coincidence measurements have long been proposed as a powerful tool, i.e. the golden probe of energy loss, to study parton energy loss in the medium [52]. The leading-order production processes of direct photons, quark-gluon Compton scattering ($q+g\rightarrow q+\gamma$) and quark-antiquark annihilation ($q+q\rightarrow g+\gamma$), are free from the uncertainties accompanying fragmentation. The outgoing high-p_T γ balances the p_T of the partner parton separated by π in azimuth ("away-side"), modulo corrections due to parton intrinsic k_T [53] and "resummation" of soft-gluon effects [54,55]. The study of the spectra of the away-side jet particles associated with the high-p_T γ_{dir} can constrain the dependence of ΔE on E. The mean-free path of the γ in the medium is large enough that its momentum is preserved, regardless of the position of the initial scattering vertex. The γ does not suffer from the geometric biases (non-uniform spatial sampling of hadron triggers due to energy loss in the medium) inherent in di-hadron azimuthal correlation measurements. A comparison between the spectra of the away-side particles associated with γ_{dir} vs. with π^0 can constrain the dependence of ΔE on L [56]. Also, comparisons between the associated particle yields for γ_{dir} triggers in- and out-of-plane and in different collision systems are additional probes of the path-length dependence of energy loss.

To leading order and in the asymptotic limit of very large jet energies, the mean multiplicities of quark and gluon jets are predicted to differ by the ratio of Casimir factors (9/4). In p+p, the dominant channel for γ_{dir} production is Compton scattering, in the covered phase space at mid-rapidity at RHIC energy. Thus quarks and gluons are present in different proportions on the away-side of the γ_{dir} and π^0 triggers. A comparison between the associated particle yields associated with γ_{dir} vs. with π^0 can constrain the ΔE dependence of on parton type. It is difficult to disentangle this from the path-length dependence. Therefore, it is important to have as many handles on the path-length dependence as possible (*i.e.* different collision systems as well measurements with respect to the reaction plane).

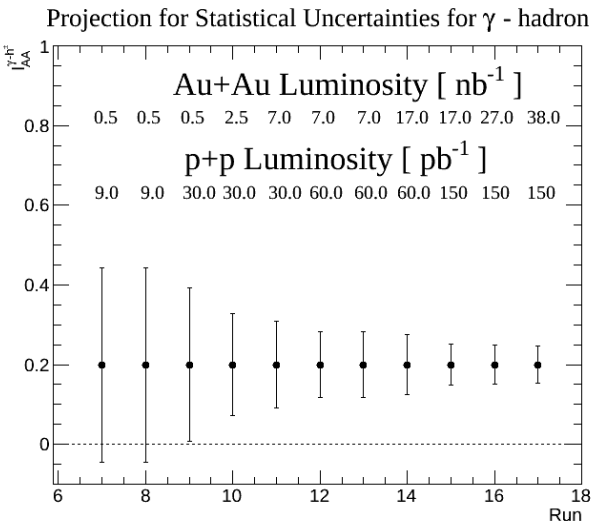

Figure 4-12: Projection for statistical uncertainties in γ-hadron suppression in a scenario of luminosity progression in different years. Projection is for $E_T(\gamma) > 15$ GeV, associated particle p_T from 4-5 GeV/c.

. In STAR experiment the required trigger for the γ_{dir} analysis is well established and has been commissioned and used for Run 7, Run 10 and run 14. The γ_{dir} trigger uses the same algorithm for the different collision systems. Currently we don't have any plan to change the level-2 algorithm of γ_{dir}; however, we may increase the trigger energy threshold.

4.2 Au+Au $\sqrt{s}$= 62 GeV

4.2.1 D^0 v_2, NPE

Analysis of the data collected in Au+Au collisions at $\sqrt{s_{NN}}$ = 62.4 GeV in run 10 revealed a difference in the elliptic flow and nuclear modification factors of electrons from heavy flavor hadrons decays (so called non-photonic electrons, NPE) in Au+Au collisions at $\sqrt{s_{NN}}$ = 62.4 GeV compared to 200 GeV. Previous measurements at RHIC in Au+Au collisions at 200 GeV established a large elliptic flow and significant suppression of heavy quarks[57]. Contrary to results for light hadrons, where a positive v_2 is observed and the difference between 200 GeV and 39 GeV is small, STAR measurements at lower energies (Au+Au collisions at 62.4 and 39 GeV) indicate that the NEP v_2 is consistent with zero and we do not observe suppression for p_T<5 GeV/c. These results indicate that there is a difference in the interactions of the heavy quarks with the surrounding nuclear matter at 200 GeV compared to the two lower energies.

It would be very interesting to explore in detail the interactions of heavy quarks with nuclear matter at $\sqrt{s_{NN}}$ = 62.4 GeV. With 6 week Au+Au 62.4 GeV physics beam, we are expecting to collect on the order of 1B minimum bias events within the HFT acceptance. However, the charm cross-section drops significantly with decreasing energy (a factor of 5 difference from 200 GeV to 62.4 GeV). We used the previous 200 GeV simulation results and extrapolated to 62.4 GeV assuming N_{bin} scaling for D^0 signal and N_{part} scaling for background. Figure 4-13 shows the statistical projection on the D^0 R_{CP} and v_2 with this data set. One can see a decisive measurement on D^0 v_2 to be distinguishable from 200 GeV is challenging, however, we could make a good measurement of D^0 R_{CP} from low to intermediate p_T where we observed an interesting flow bump structure at Au+Au 200 GeV measurement.

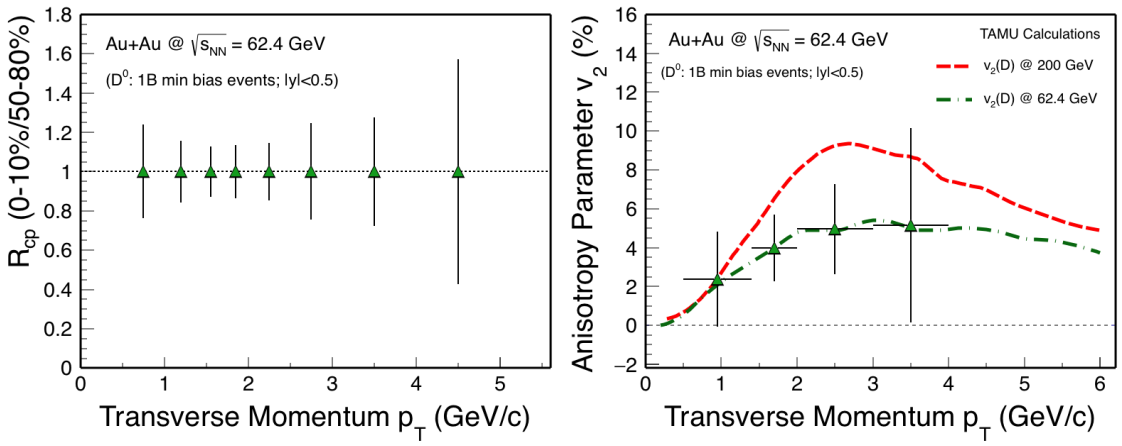

Figure 4-13 Statistical projection on D_0 R_{CP}(0-10%/50-80%) and v2(0-80%) measurements with 1B minimum bias Au+Au 62.4 GeV events with HFT.

For the NPE measurements, we estimate that no significant improvement over Run 10 results can be achieved with the amount of beam time and luminosity available in run 16. Figure 4-14 shows projections for NPE v_2 and R_{CP} (0-10%/40-60%) for 1 B minimum bias events. These estimates are based on pQCD predictions for NPE production at $\sqrt{s_{NN}}$ = 62.4 GeV [58], assuming binary scaling and that the NPE measurement efficiency is the same as in Run 10. Due to larger photonic electron background (factor ~2 increase compared to run 2010), steeply falling charm spectrum and a kinematic shift of NPE p_T towards lower values compared to the parent meson p_T, we will be able to measure suppression and elliptic flow with sufficient precision in the intermediate p_T range (p_T < 3 GeV).

Such data will not allow quantifying if NPE production is suppressed at high p_T (5-10 GeV/c). Moreover, the measurement of the nuclear modification factor R_{AA} at 62.4 GeV suffers from large statistical uncertainties due to lack of a high quality p+p baseline, which cannot be addressed with a short p+p run in Run 16.

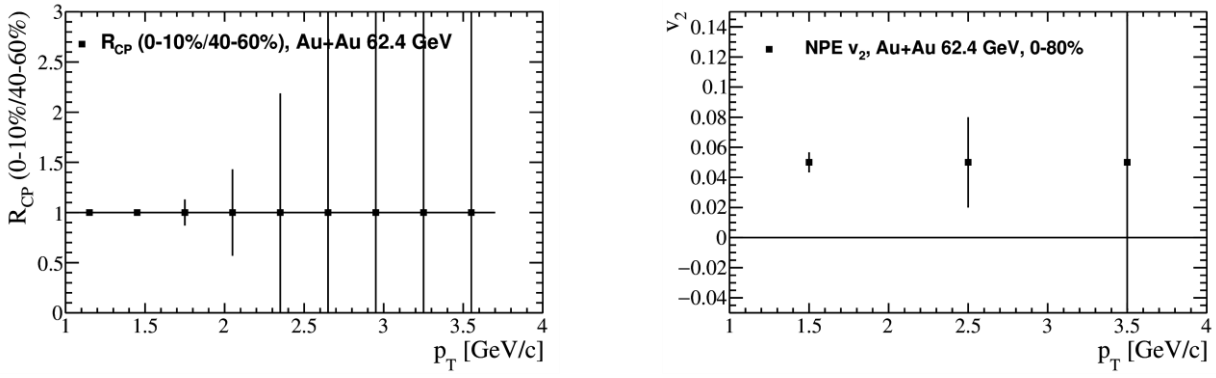

Figure 4-14 Statistical projection on NPE R_{CP}(0-10%/40-60%) and v_2(0-80%) measurements in |η|<1 with 1B minimum bias Au+Au 62.4 GeV.

4.2.2 Jet measurements in Au+Au $\sqrt{s_{NN}}$= 62.4 GeV

In heavy-ion collisions the underlying background due to particles arising from soft (low Q^2 processes) both smears the jet energy and generates fake jets. Recoil jets, which have been widely used in the jet quenching study, are jets reconstructed on the opposite hemisphere in azimuth relative to the trigger hadron. Fake recoil jets overwhelm the number of true hard jets by orders of magnitude and hence hide the signal. This effect makes it especially difficult to reconstruct jets at low collision energies where the jet spectrum is very steep. STAR has recently developed a mixed event technique to precisely subtract the fake jet contribution from the measured recoil jets. With this method recoil jets can be reconstructed with precision and without selection bias based on jet fragmentation patterns, for large R (currently up to R=0.5) and over a very broad kinematic range, including low transverse momenta.

During run 10 STAR recorded 67.3 M good minimum bias (0-80%) Au+Au events at $\sqrt{s_{NN}}$ = 62.4 GeV. A preliminary high p_T (6-20 GeV/c) hadron-triggered recoil jet analysis has been performed utilizing the anti-k_T jet finding algorithm. Figure 4-15 (left) shows the measured recoil jet spectrum corrected for the average background energy density ρ, for charged jets with R=0.3 in mid-central (30%-50%) Au+Au collisions at $\sqrt{s_{NN}}$ = 62.4 GeV (red points). The mixed event distribution is shown as the gray shaded area. A significant signal above the mixed event is seen for p_T > 5 GeV/c. A comparison of the background subtracted distribution to a smeared PYTHIA calculation (~p+p $\otimes$ heavy-ion fluctuations) is shown on the right hand side of Figure 4-15. An average suppression of 0.24 is observed. On both plots an extrapolation to higher jet p_T values is shown, using PYTHIA with an assumed suppression factor of 9 (left) and an exponential fit to data (right). The orange shaded areas show the expected statistical error bars for charged jets with 1.5B minimum bias events which can be collected by STAR in a 6 week data taking period. The kinematic reach in charged jet energy for this dataset is about 20 GeV.

The analysis technique will be extended directly to calorimetric jets once the charged jet results are published. The kinematic reach shown for charged jets for 1.5B events in Figure 4-15 corresponds to about 30 GeV for full calorimetric jets, which should be considered the true physics reach of the measurement. Note this range corresponds to the jet spectrum without the unfolding corrections, which account for the smearing introduced from underlying fluctuations, applied. This analysis will enable the precise study of jet energy loss in a region of significant overlap with measurements at higher collision energies.

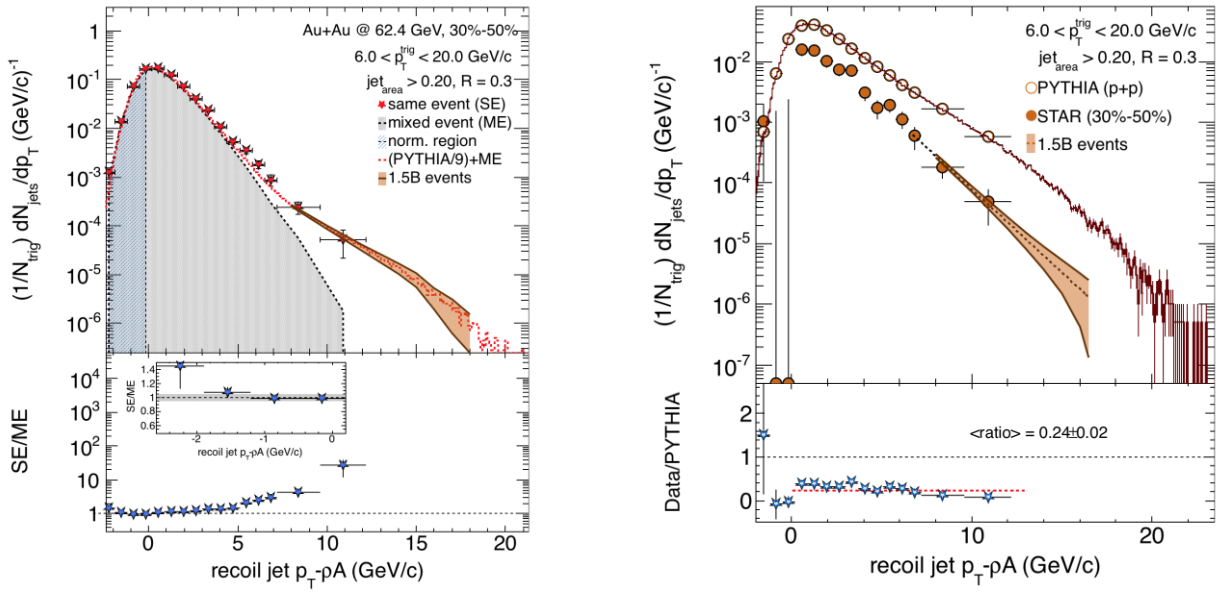

Figure 4-15**:** (left) Recoil jet spectrum for R=0.3 in mid-central (30%-50%) Au+Au collisions at $\sqrt{s_{NN}}$ = 62.4 GeV corrected for the average background energy density ρ, with a charged hadron trigger with p_T > 6 GeV/c and cone radius R = 0.3 (anti-k_T). The gray shaded area depicts the mixed-event distribution, which represents the combinatorial background (see text for details). (right) Background subtracted recoil jet spectrum. In both figures a comparison to PYTHIA calculations is shown and an extrapolation to higher jet p_T values with increased statistics. A suppression factor of 9 was assumed on the left plot for PYTHIA

Figure 4-16 shows the recoil jet spectrum for 0-30% most central Au+Au collisions at $\sqrt{s_{NN}}$ = 62.4 GeV. The statistics of the current dataset are too limited to extract a significant signal. Nevertheless, the central values of the data hint at a significantly larger suppression than at higher energies. With 1.5B minimum bias events we can extend the p_T range for most central collisions to about 25 GeV/c in charged jet energy. Fully reconstructed jets, including the BEMC detector information, will extend this p_T range significantly. The expected statistical errors for 1.5B events are shown as an orange shaded band in Figure 4-16, using PYTHIA with a suppression of 18 to estimate the recoil jet spectrum at higher p_T. If the picture of very strong jet suppression persists, the requested dataset will make constrained measurements at the highest p_T, and provide significant upper limits at lower p_T. Related analyses can be performed for inclusive jet spectra and gamma triggered recoil jet spectra. The gamma triggered analysis has the advantage of being able to utilize an efficient dedicated high p_T trigger using the BEMC detector, as was already successfully demonstrated in run 10.

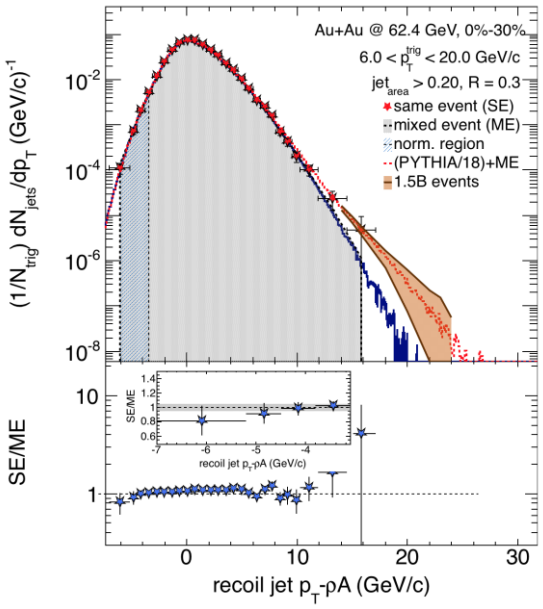

Figure 4-16: Recoil jet spectrum for R=0.3, in the 30% most central Au+Au collisions at $\sqrt{s_{NN}}$ = 62.4 GeV. The gray shaded area and blue histogram depict the mixed event distribution. The red histogram shows a PYTHIA calculation with an assumed jet suppression of 18, which fits the data in the whole p_T range. The orange shaded area is showing the expected statistical error bars for 1.5B recorded minimum bias events.

These measurements are predicted to extend the study of the temperature dependence of $\hat{q}/T^3$ towards values much lower than those achievable at top RHIC and LHC energies [59]. As shown in Figure 4-17, the lever arm of the 62.4 GeV measurements, combined with results from top RHIC energies and from the LHC, will provide crucial insight into the physics of jet-medium interactions.

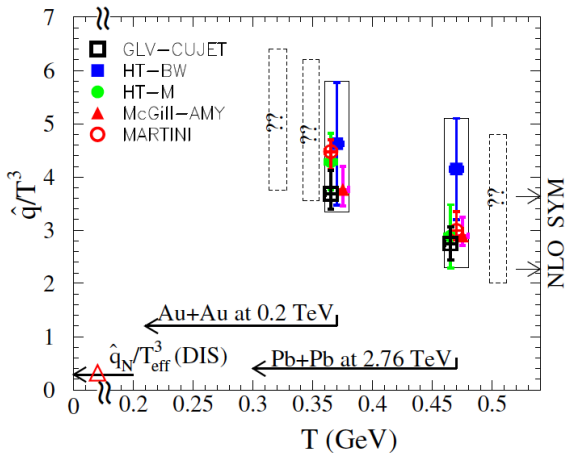

Figure 4-17: $\hat{q}/T^3$ as a function of the temperature T for initial quark jets with energy E = 10 GeV [1]. The dashed boxes show the expected values for $\sqrt{s_{NN}}$ = 63, 130, and 5500 GeV

4.3 d+Au Beam Energy Scan

There is clear evidence that above 62.4 GeV significant energy loss occurs as partons pass through the hot dense medium created in heavy-ion collisions, for instance the R_{CP} of charged hadrons with p_T > 3 GeV/c, Figure 4-18, is significantly less than unity. For lower beam energies the case is less clear due to the well-known Cronin effect [60]. The Cronin effect was discovered in p+A collisions and describes the observed hardening of the p_T spectra of hadrons when compared to p+p data. This effect is stronger for heavier particles and at lower beam energies and sets in around 1-2 GeV/c. Although there are several suggestions as to the origins of this experimental observation, the Cronin effect

remains to be well explained by theory. The most prominent explanation is that the effect arises from multiple scatterings of partons from the proton off partons from the nucleus. As a result the partons undergo a transverse momentum kick shifting their transverse momenta from lower to higher values creating the observed enhancement.

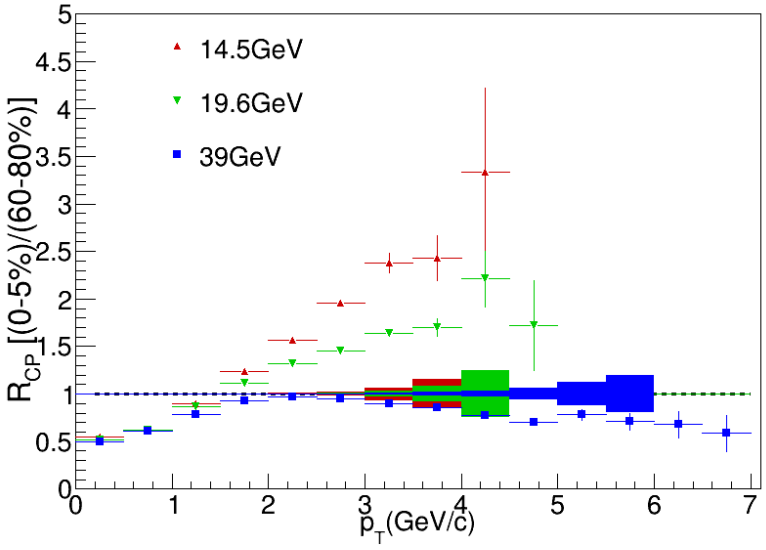

Figure 4-18 The R_{CP} of charged hadrons for $\sqrt{s_{NN}}$ = 14.5, 19.6 and 39 GeV, Shown as the boxes around unity are the estimated errors for R_{dAu} assuming 100M good events at each energy for p+p and d+Au collisions

Since the Cronin enhancement is sizeable the expectation of R_{cp} equal to unity for lower beam energies may be no longer correct. Significant energy loss can still be occurring despite the fact that $R_{cp} >> 1$ for $\sqrt{s} < 20$ GeV. To disentangle these two effects it is therefore critical that we accurately measure the cold nuclear matter effects at these lower collision energies to determine what, if any, energy loss is occurring. By contrasting minimum-bias R_{dAu} measurements to our existing R_{cp} we can resolve where significant loss due to interactions with the hot and dense medium begins. It has been shown that even at LHC energies minimum-bias p+Au data show no significant deviations from unity, i.e. no clear energy loss signals. Some measurements do exist above 27 GeV for p+W collisions for π, K, p but no accurate data exist for strange baryons or at lower beam energies.

To make an estimate of the statistics needed to make decisive R_{dAu} measurements we required that there be a <5% statistical error in the 3.5-4 GeV/c bin for both the p+p and the d+Au data. We assume N_{bin} scaling of the d+Au data i.e. R_{dAu} = 1. For charged particles in d+Au (p+p) this means 50M (260M), 17M (78M) and 3.5M (17M) good events are needed at 14.5, 19.6 and 39 GeV beam energies respectively. Figure 4-18 shows the estimated statistical errors for the charged particle R_{dAu} compared to the current preliminary R_{cp} measurements. To perform the same study for π, K, p requires a factor 10 more statistics. In order to extend these studies further to Λ baryons at the same p_T would require 400M for d+Au at 14.5 GeV and 82 M events at 39 GeV. To have the same reach in p+p at 14.5 GeV would require 2B. Even without such an extended reach in p_T the kaon and Λ measurements are of interest to extract possible strangeness enhancement signals and probe particle production ratios as a function of p_T and contrast to the Au+Au measurements at the same energy.

Finally this d+Au dataset will allow us to probe for the long range $\Delta\eta$ feature known as the ridge that has been observed at RHIC in d+Au collisions and at the LHC in p+Pb collisions. Two prominent theories have emerged to explain this phenomenon. One is hydrodynamic expansion in response to fluctuations in the initial interaction geometry. The second is the color glass condensate,

where small-x gluons are saturated below the saturation scale of Q_s in transverse momentum. At transverse momentum ~Q_s, two-gluon production is enhanced at small $\Delta\varphi$ over a large range in $\Delta\eta$. The two physics mechanisms likely have different beam energy dependences. In order to unravel the underlying physics mechanisms it is therefore important to measure the ridge or the lack thereof over a span of RHIC energies.

Another important prospect for d+Au collisions at low energies is to provide a baseline study of how well the hadron cocktails reproduce the dielectron mass spectra, and whether there is any excess deviated from the cocktail in the low mass range in d+Au collisions due to possible medium effect and flow. Figure 4-19 shows a projection of what statistical error we can achieve with 100 million d+Au collisions at 19.6GeV. The particles yields in ref. [8] are used to extrapolate to d+Au collisions.

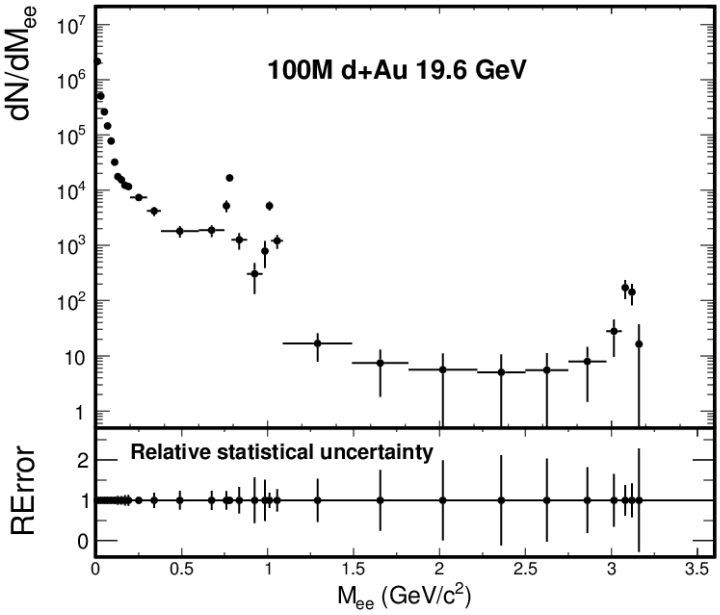

Figure 4-19 Projection of the dielectron invariant mass spectra in d+Au collisions at 19.6 GeV. The signal-to-background ratio is assumed to scale with 1/Npart.

5 Run 17 Request

5.1 Polarized p+p at √s = 500 GeV

Much of our present knowledge of nucleon structure comes from deep-inelastic lepton-nucleon scattering (DIS) experiments, with a great wealth of data on the unpolarized structure of the proton available from HERA [61]. From HERA, we have learned that quarks carry 50% of the momentum of the proton, with the other half carried by gluons, which dominate for x <0.1. Despite all that has been learned through DIS measurements, studying nucleon structure in a wide variety of reactions is essential in order to piece together a complete picture. Hadron-hadron interactions offer several advantages [62]. Direct access to gluons is possible through parton-parton scattering, making the measurement of the spin contribution of the gluon to the spin of the proton a key component of the RHIC program. W-Boson production and the Drell-Yan process are both golden probes to cleanly access antiquark distributions in hadron-hadron collisions. Drell-Yan processes will become an increasingly important part of the future RHIC p+p and p+A program. Comparing observations from DIS and hadronic interactions also allows us to test the assumptions of universality across processes in describing hadron structure and hadronization within the framework of perturbative QCD (pQCD). At high energy, there remain two fundamental aspects of the nucleon partonic structure, which are rather poorly determined by experiment. One is the nature of the nucleon spin; the other is to go beyond our current simple one-dimensional picture of nucleons by correlating the information on the individual parton contribution to the spin of the nucleon with its transverse momentum and spatial distribution inside the nucleon.

5.2 The Sivers function

A natural next step in the investigation of nucleon structure is an expansion of our current picture of the nucleon by imaging the proton in both momentum and impact parameter space. At the same time we need to further our understanding of color interactions and how they manifest themselves in different processes. In the new theoretical framework of transverse momentum dependent (TMD) parton distributions we can obtain an image in both transverse and in longitudinal momentum space (2+1 dimensions). To achieve this, one has to go beyond the conventional collinear parton picture in the hard processes. Two theoretical formalisms have been proposed to explain sizable SSAs in the QCD framework. For a spin dependence in the initial state these are: transverse momentum dependent parton distributions functions, such as the Sivers functions and transverse-momentum integrated (collinear) quark-gluon-quark correlations, which are twist-3 distributions in the initial state proton such as the Efremov-Teryaev-Qiu-Sterman (ETQS) function [63], the Twist-3 analog to the Sivers function.

The Sivers function, $f_{1T}^{\perp}$, describes the correlation of the parton transverse momentum with the transverse spin of the nucleon. A non-vanishing $f_{1T}^{\perp}$ means that the parton distribution will be azimuthally asymmetric in the transverse momentum space relative to the nucleon spin direction. The Sivers function, $f_{1T}^{\perp}$, is correlated with the ETQS functions, $T_{q,F}$, through the following relation:

$$T_{q,F}(x,x) = -\int d^2k_\perp \frac{|k_\perp|^2}{M} f_{1T}^{\perp q}(x,k_\perp^2)|_{SIDIS}$$

In this sense, a measurement constraining the ETQS function indirectly also constrains the Sivers function. An important aspect of the Sivers effect, which has emerged from theory, is its process dependence and the color gauge invariance. In SIDIS, the quark Sivers function is manifested in association with a final state effect from the exchange of (any number of) gluons between the struck quark and the remnants of the target nucleon. On the other hand, for the virtual photon production in the Drell-Yan process, the Sivers asymmetry appears as an initial state interaction effect. As a consequence, the quark Sivers functions are of opposite sign in these two processes and this non-universality is a fundamental prediction from the gauge invariance of QCD. The experimental test of this sign change is one of the open questions in hadronic physics (NSAC performance measure HP13) and will provide a direct verification of QCD factorization. The COMPASS experiment at CERN is pursuing this sign change through Drell-Yan processes using a pion beam and new initiatives have been proposed e.g. at FNAL.

While the required background suppression for a meaningful measurement of asymmetries in Drell-Yan (DY) production are challenging, other channels can be exploited in p+p collisions, which are equally sensitive to the predicted sign change. These include prompt photons, W± and Z bosons, and inclusive jets. These are either already accessible with the existing STAR detector or need only modest upgrades, but all require continued polarized beam operations.

Figure 5-1 shows the predicted A_N for W^- and *DY* **before** [69,68] (left) and after [66] (right) **TMD evolution is taken into account**. Lately, there have been several theoretical predictions for the transverse single-spin asymmetries for DY, $W^{\pm}$ and Z^0 bosons including TMD evolution, for examples see [64,65,66] and references therein. In all cases the asymmetries have been significantly reduced. The TMD evolution equations contain in addition to terms that can be calculated in QCD, non-pertubative terms, whose parameters need to be obtained from fits to data. Unfortunately there is not yet a consensus as to how to obtain and handle the non-pertubative input in the TMD evolution, for details see [67]. This complication leads to large uncertainties in the prediction for the DY, $W^{\pm}$ and Z^0 SSA, **which can only be addressed by future measurements.**

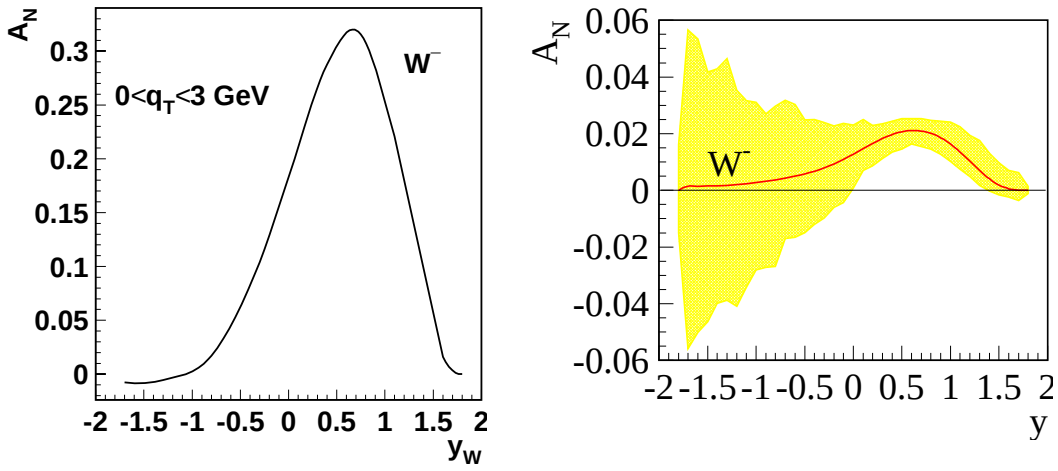

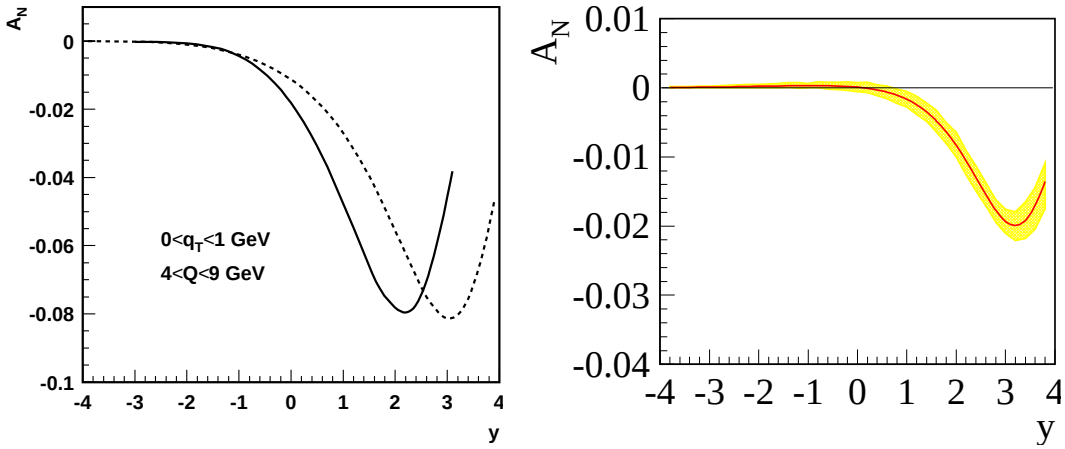

Figure 5-1: upper row: (left) Prediction for Sivers asymmetry A_N as a function of W^- boson rapidity at $\sqrt{s}$=500 GeV [69] **before any TMD evolution is applied.** (right) Theoretical predictions from reference [66] for W^- for 0 GeV $< p_T <$ 3 GeV **after** TMD evolution is applied. The yellow bands represent the uncertainties for the asymmetry. At negative rapidity this is mainly caused by the currently unconstrained sea quark Sivers functions. lower row: (left) Prediction for Sivers asymmetry A_N as a function of *DY* lepton-pair rapidity at $\sqrt{s}$=500 GeV [68] **before any TMD evolution is applied.** (right) Theoretical predictions from reference [66] for DY for 0 GeV $< p_T <$ 1 GeV and 4 GeV < Q < 9 GeV **after** TMD evolution is applied. The yellow bands represent the uncertainties for the asymmetry.

The transversely polarized data set in Run-2011 at $\sqrt{s}$ = 500 GeV allowed STAR to reconstruct the transverse single-spin asymmetries for A_N for $W^{\pm}$ and Z^0 bosons. The measurement of the A_N for $W^{\pm}$ bosons is especially challenging where, contrary to the longitudinally polarized case, it is required to completely reconstruct the W bosons as the kinematic dependences of A_N cannot easily be resolved through the high p_T decay lepton, for details see [69,70]. Due to the large STAR acceptance it was possible to reconstruct the W boson kinematics from the recoil jet, a technique used at D0, CDF and the LHC experiments to reconstruct the W boson kinematics. Figure 5-2 shows the transverse single-spin asymmetries for A_N for $W^{\pm}$ as a function of the W boson rapidity y. The asymmetries have also been reconstructed as a function of the p_T of the W boson. For the Z^0 boson the asymmetry could only be reconstructed in one bin in y with the current limited statistics (25 pb^{-1}). Details for this analysis can be found in [71]. The analysis represents an important proof of principle, similar to the first Run-9 $W^{\pm}$ A_L measurement.

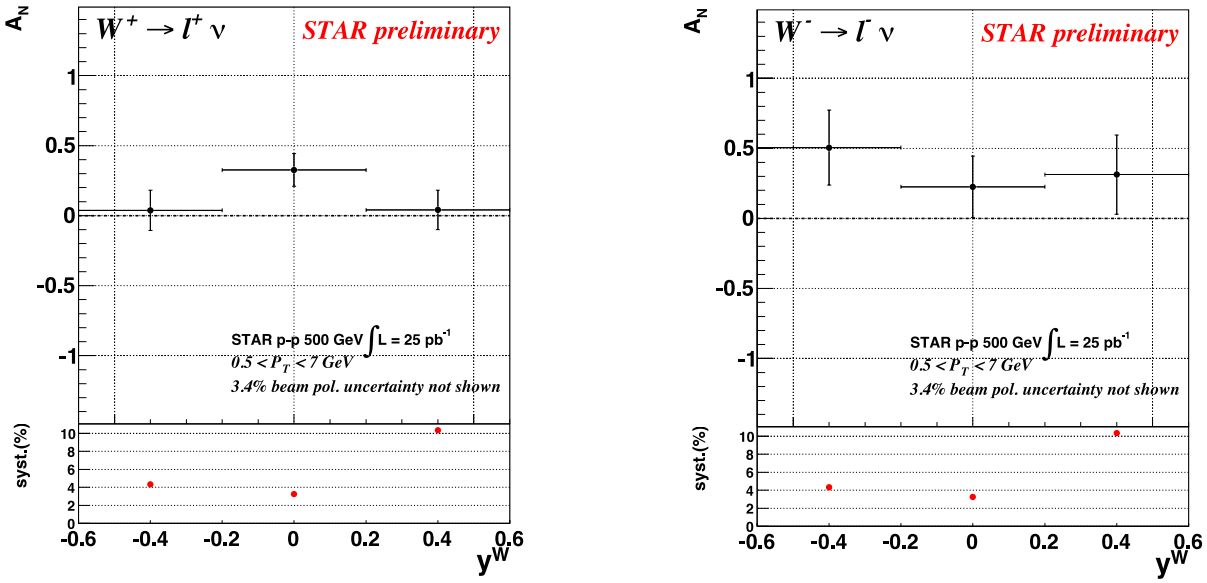

Figure 5-2: The transverse single-spin asymmetries for A_N for $W^{\pm}$ as function of the W boson rapidity y.

$W^{\pm}$ boson production is also the ideal tool to study the spin-flavor structure of sea quarks inside the proton. Such a measurement of the transverse single-spin asymmetry will provide the very first constraint on the sea quark Sivers function in an x-range where the measured asymmetry in the $\bar{u}$ and $\bar{d}$ unpolarized sea quark distribution functions, as measured by E866 [72], can only be explained by strong non-pQCD contributions. At the same time, this measurement is also able to access the sign change of the Sivers function, **if the effect due to TMD evolution on the asymmetries is in the order of a factor of 5 reduction.** Figure 5-3 shows the projected uncertainties for transverse single-spin asymmetries of $W^{\pm}$ and Z^0 bosons as a function of rapidity and p_T for a delivered integrated luminosity of 400 (900) pb^{-1} and an average beam polarization of 55%.

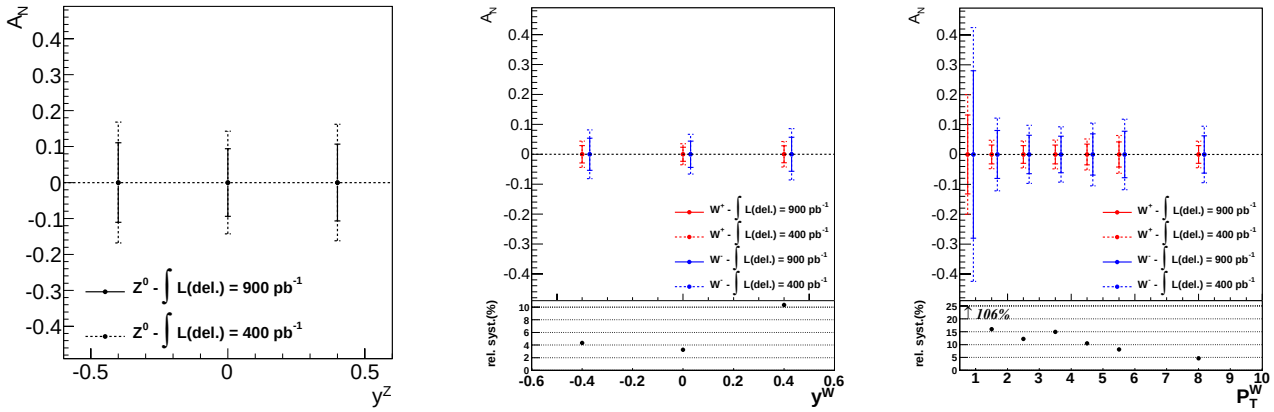

Figure 5-3: The projected uncertainties for transverse single-spin asymmetries of $W^{\pm}$ and Z^0 Bosons as a function of rapidity and p_T for a delivered integrated luminosity of 400 (900) pb^{-1} and an average beam polarization of 55%.

In order to optimize the figure-of-merit for the W-reconstruction the luminosity through out the fill needs to be held at a constant ZDC-rate of 300 kHz, corresponding to a RHIC p+p luminosity of 1.285×10^{32} cm^{-2}s^{-1} (see Figure 5-4). These parameters have been determined from the W-reconstruction efficiencies as function of the raw ZDC rate from the result of the 2011 – 2013 polarized p+p data taking.

An integrated delivered luminosity of 400 pb^{-1} corresponds to a RHIC run of 15 cryo-weeks, if the concept of a dynamic β^* squeeze through the duration of a RHIC fill is utilized. Changing the β^* through the fill by a factor of 2 will result in a 20% change of the luminosity through a fill, resulting in a delivered luminosity of 40 pb^{-1} / week.

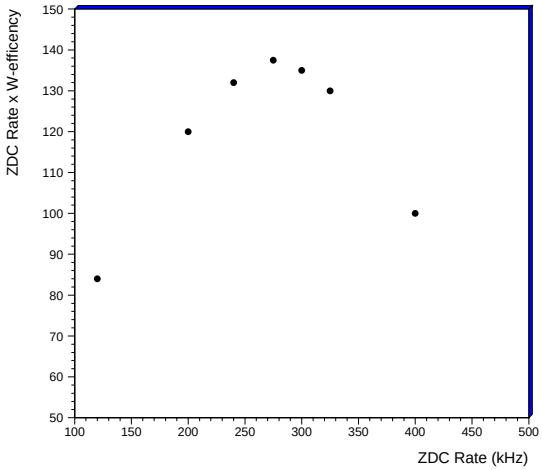

Figure 5-4: The FoM to reconstruct W-bosons in STAR as function of the ZDC raw rate. The W-boson reconstruction efficiency was obtained from the data measured in 2011 to 2013. The highest FoM is reached at a ZDC rate of 300 kHz corresponding to a luminosity of 1.285 x 10^{32} cm^{-2}s^{-1}.

The ultimate test for the TMD evolution and the sign change of the Sivers function would be to measure A_N for $W^{\pm}$, Z^0 boson and DY production simultaneously. To obtain a significant measurement of A_N for DY production, the DY leptons need to be detected between rapidities 2 and 4 for a lepton pair mass of 4 GeV and bigger (see Figure 5-1). This is a highly non-trivial measurement, as backgrounds mainly due to QCD 2→2 processes need to be suppressed by a factor of ~10^6. STAR proposes a measurement of A_N for DY during RHIC run-17, using the FMS, its preshower and a post-shower (for details of the simulation see section 5.2.2). Figure 5-5 shows the achievable statistical precision measuring one point in the rapidity-range 2.5 < η < 4.0 for the asymmetry for a delivered integrated luminosity of 400 pb^{-1} in comparison to the theoretical predicted asymmetry with and without taking TMD evolution into account.

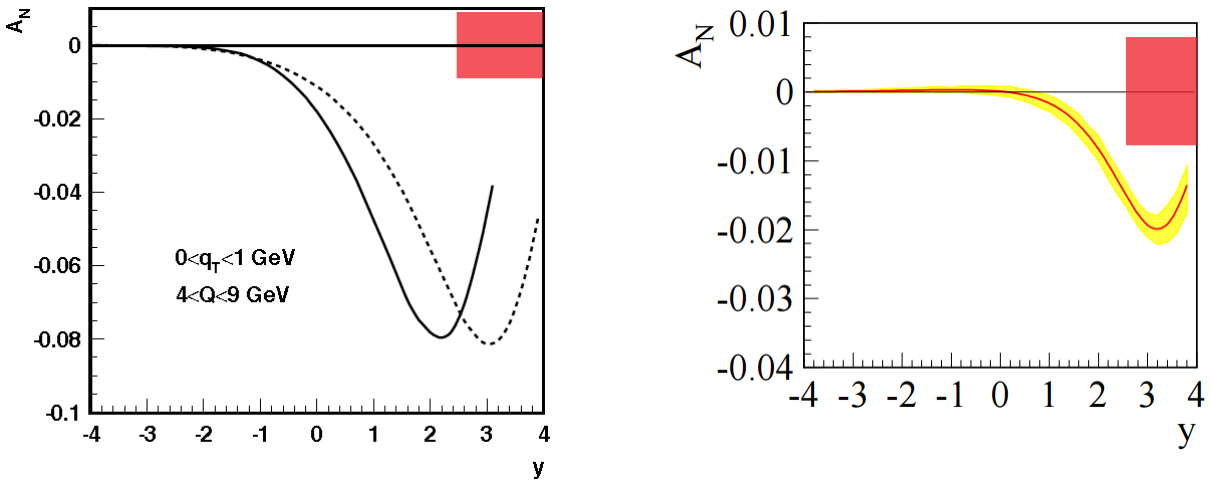

Figure 5-5: The orange square indicates the achievable statistical precision measuring one point in the rapidity-range 2.5 < η < 4.0 for the asymmetry for a delivered integrated luminosity of 400 pb^{-1} in comparison to the theoretical prediction for the Sivers asymmetry A_N as a function of *DY* lepton-pair rapidity at $\sqrt{s}$=500 GeV [73] **before any TMD evolution is applied** (left). Theoretical predictions from reference [66] for DY for 0 GeV <p_T< 1 GeV and 4 GeV < Q < 9 GeV **after** TMD evolution is applied (right). The yellow bands represent the uncertainties for the asymmetry.

5.2.1 The Efremov-Teryaev-Qiu-Sterman function

Transverse single spin asymmetries in direct photon production provide a different path to access this sign change through the formalism utilizing the Twist-3 parton correlation functions. For the 2015 polarized p+p run STAR installed a preshower in front of the forward electromagnetic calorimeters the FMS. This upgrade enabled a measurement of the SSA for direct photons up to x_F ~ 0.7 in Run-2015 at $\sqrt{s}$ = 200 GeV. Figure 5-6 shows theoretical predictions and statistical and systematic uncertainties for a direct photon SSA at $\sqrt{s}$ = 500 GeV. The theoretical predictions represent a calculation based on Twist-3 parton correlation functions, $T_{q,F}$, constrained by the Sivers function obtained from a fit to the world SIDIS data [74]. At $\sqrt{s}$ = 500 GeV the theoretical asymmetries are reduced by a factor 2 due to evolution effects compared to the one at √s = 200 GeV. These evolution effects are currently only based on the well know evolution effects following DGLAP. The comparison of the 200 GeV and 500 GeV results can reveal if also in the case of the Twist-3 formalism evolution effects there are additional evolution effects as for TMDs. Due to the electromagnetic nature of the process the individual parton densities are weighted with the respective quark charge e_q^2, therefore the direct photon asymmetries are mainly sensitive to the u and quark Twist-3 correlation functions.

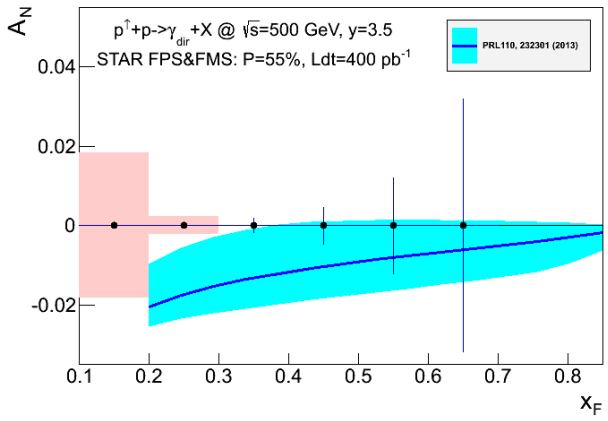

Figure 5-6: Statistical and systematic uncertainties for the direct photon A_N after background subtraction compared to theoretical predictions from Ref. [74] for $\sqrt{s}$ = 500 GeV as measured by STAR. If the correlation between the Twist-3 correlation functions and the Sivers function as described in [Eq.2-1] would be violated the asymmetries would have the same magnitude but being positive.

Table 5-1 summarizes the different observables and their sensitivity to the following main questions to be addressed with the transversely polarized p+p run in 2017:

- Can the non-universality of the Sivers function between SIDIS and DY-production experimentally verified?
- What are the effects due to TMD evolution on A_N?
- Do sea quarks have a significant sea quark sivers function?
- Can the relation between the Sivers function and the twist-3 Efremov-Teryaev-Qiu-Sterman (ETQS) distribution function experimentally verified.
- Can the evolution of the twist-3 Efremov-Teryaev-Qiu-Sterman (ETQS) distribution functions experimentally constrained

Answers to these questions are critical for the effective planning of the physics program of an electron-ion-collider.

	$A_N(W^{+/-},Z^0)$	$A_N(DY)$	$A_N(\gamma)$
Sensitive to Sivers fct. sign change through	Yes	Yes	No

TMDs			
Sensitive to Sivers fct. sign change through Twist-3 $T_{q,F}(x,x)$	No	No	Yes
Sensitive to TMD evolution	Yes	Yes	No
Sensitive to sea quark Sivers function	Yes	Yes	No
Detector upgrade needed	No	Yes FMS post-shower	No
Biggest experimental challenge	Integrated luminosity	Background suppression Integrated luminosity	----

Table 5-1: Summary of all the processes accessible in STAR to measure access the sign change of the Sivers function.

5.2.2 Prospects for measuring Drell-Yan A_N

The difficult task of DY measurements is the suppression of the overwhelming hadronic background which is on the order of $10^5 \sim 10^6$ larger than the total DY cross-section. The probability of mis-identifying a hadron track as e^+/e^- has to be suppressed down to the order of 0.01% while maintaining reasonable electron detection efficiencies. Due to the rarity of Drell-Yan events, the simulation of the both the Drell Yan process and the large QCD background are crucial to understanding how well we can distinguish the signal from the background. We have studied the combined electron/hadron discriminating power of the proposed calorimeter postshower and current calorimeter systems. We found that by applying multivariate analysis techniques to the features of EM/hadronic shower we can achieve hadron rejection powers of 800 to 14,000 for hadrons of 15 GeV to 60 GeV with 90% electron detection efficiency. The hadron rejection power has been parameterized as a function of hadron energy and has been used in a fast simulation to estimate DY signal-to-background ratios.

The rapidity of interest is $2.5 < \eta < 4.0$. The current STAR detectors in this rapidity are the Forward Meson Spectrometer (FMS), a Pb-glass electromagnetic detector with photomultiplier tubes, and the preShower, three layers of scintillator with silicon photomultipliers. The FMS is primarily sensitive to electrons and photons while hadrons will leave as minimum ionizing particles. The preShower, which consists of three layers of scintillator, provides photon and charged particle separation. The first two layers provide x and y positioning. A lead converter precedes the third scintillator causing photons to shower in lead and deposit significant energy in the third scintillator. To suppress photons, the signal should have energy deposition in each layer of the preshower. The threedetector (preShower, FMS and proposed postShower) setup provides photon/particle separation and electron/hadron discrimination.

We have simulated the response of the calorimeter to single electrons and π^-. To discriminate EM shower against hadronic shower we have used the total energy sums in layer 1, 2 and 3 of the preshower, total energy of the EMCal (FMS) and total energy of the postshower (see Figure 5-7). 5 million single particle events were run through the STAR geometry at intervals of 5 GeV ranging from 15 to 60 GeV. For lower energies, 100,000 provided efficient information to parameterize the rejection

of the signal. For higher energies, from 45 to 60 GeV, 1 million events were necessary to parameterize. A parameterized rejection function was established at 90% electron efficiency.

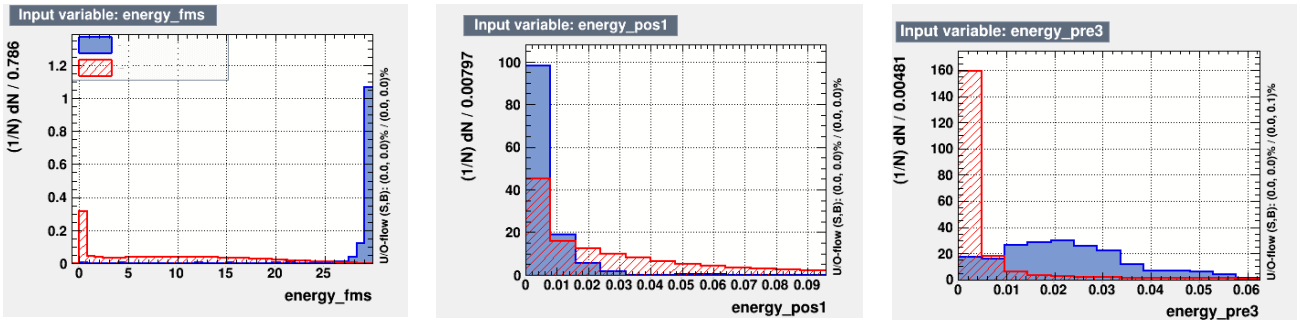

Figure 5-7: Energy from GEANT4 single particle simulations in the STAR geometry. The blue and red are signal and background, respectively, for the FMS, PostShower, PreShower, from left to right,

These energy observables from the three detectors have been used as inputs to a Boosted Decision Trees (BDT) algorithm. The BDT contains 1000 binary decision trees each has a depth of 4 and corresponds to a particular partition of the 4-dimensional feature space into signal (electron) and background (hadron) regions. They are trained sequentially using half of the electron/ π^- samples generated. Mis-identified tracks from the previous decision trees were given a higher weight in training the subsequent trees. In the end each decision tree was given an index representing its performance during the training. In the validation stage the decision on each track identification was made based on the collective response of all of the decision trees, with each of their responses weighted by the performance index. The boosting algorithm takes advantage of using not only the discriminating power of each single observable but also the correlations among them.

To estimate the DY signal to background ratio the e/h discriminating power has been parameterized as a function of the track energy (see Figure 5-8). We have generated 600 million PYTHIA p+p events at 500 GeV with *CKIN(3)* = 3 GeV and a forward filter requiring a total p_T> 3 GeV in any of the four jet-patch-like regions in 2.7 < η < 3.8. All basic QCD 2→2 scatterings as well as heavy flavor channels were enabled. Events were smeared using the simulated detector resolutions of the Forward Meson Spectrometer.

The DY productions through $q\bar{q}$ annihilation and qg scattering processes were separately generated and scaled to the same luminosity. The final background yields as a function of pair masses were then fit by an exponential function and rescaled to a total luminosity of 400 pb^{-1}, the results is shown in Figure 5-9.

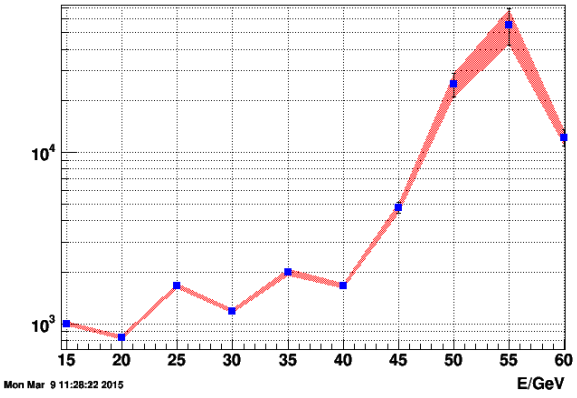

Figure 5-8: Rejection power as a function of energy with connected error bars. A smooth polynomial was fit to the rejection curve.

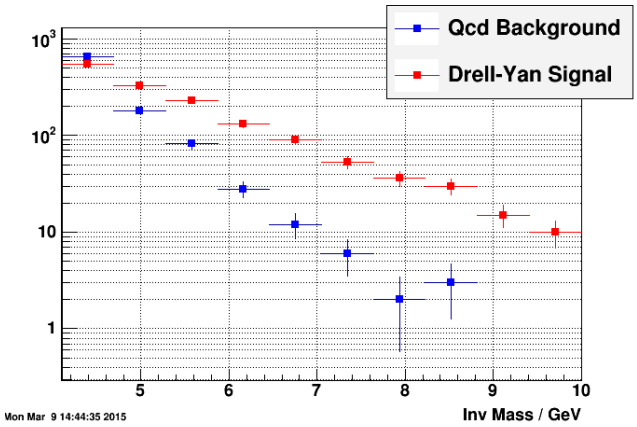

Figure 5-9: Plotting the background after BDT rejection (blue) along with a normalized Drell-Yan signal (red).

5.2.3 Interference Fragmentation, Collins, Collins-like and Sivers Functions

As discussed in Section 2.2.1, significant asymmetries have been measured in the Interference Fragmentation (IFF) and Collins Function channel in the run 11 $\sqrt{s}$ = 500 GeV data. Asymmetries sensitive to the gluon Sivers function and gluon linear polarization (Collins-like) have also been measured for the first time in hadronic collisions. The 25 pb^{-1} data set utilized for these results was initially collected to set systematic error limits for the inclusive jet A_{LL} measurement. As a result the extracted asymmetries are statistically limited. A high luminosity run will provide the opportunity to increase the precision, by at least a factor of two, in all of these channels. The statistical errors on the IFF and Collins asymmetries shown in Figure 2-8 and Figure 2-9 will become comparable or smaller to the errors in the existing $\sqrt{s}$ = 200 GeV data, provide even more compelling tests of evolution and universality. The run 17 statistics will also be sufficient to measure the Collins effect asymmetry for a combined protons and kaon signal with equal or better precision than shown for pions at $\sqrt{s}$ = 500 GeV in Figure 2-9. Finally, a high precision measurement of the gluon Sivers function in the Twist-3 formalism through A_N for inclusive jets will be complementary to the results by the A_NDY collaboration done at $\sqrt{s}$=500 GeV for η>3 [75].

5.3 Isobar (Zr+Zr, Ru+Ru) CME effects

The CME can be further verified, especially for mid-central/mid-peripheral events, with collisions of isobaric nuclei, such as $_{44}{}^{96}$Ru and $_{40}{}^{96}$Zr [76]. Ru+Ru and Zr+Zr collisions at the same beam energy are almost identical in terms of particle production, as illustrated via Monte Carlo Glauber [77] simulations in Figure 5-10. The ratio of the multiplicity distributions from the two cases is consistent with unity everywhere except in the 0-10% most central collisions, where the multiplicity from the deformed Zr (β_2 = 0.2) is lower than that of the spherical Ru (β_2 = 0.05). Even in this case the deviation from unity is only ~2%. The deformation of Zr will be further discussed below. Since this charge separation analysis has already been successfully performed in both Au+Au and Cu+Cu at $\sqrt{s}$=200 GeV and 62.4 GeV we are confident that both isobaric nuclei are sufficiently large to allow for creation of the pertinent physics.

The difference in the initial electric charge between Ru+Ru and Zr+Zr collisions provides us with a handle on the magnetic field, which is mostly produced by the spectator protons. Figure 5-11 presents theoretical calculations of the initial magnetic field ($-eB_y/m^2_\pi$) for the two colliding systems at 200 GeV [78]. For the same centrality bin, Ru+Ru collisions produce a stronger magnetic field than Zr+Zr. The major theoretical uncertainty comes from the modeling of the nuclei, e.g., how to model the electric charge distribution of the proton: treating the proton as a point charge or as a uniformly charged ball or something else. However, for the event averaged $<B_y>$ calculation, this type of uncertainty is small. Another uncertainty involves the Lienerd-Wichert potential used in this calculation, which contains no quantum corrections. At RHIC energies, including the QED correction makes little difference [79]. In addition, the theoretical uncertainties are greatly suppressed when we take the ratio. Panel (b) of Figure 5-11 shows that the B_y ratio of Ru+Ru over Zr+Zr is close to 1.1 for peripheral events, and reduces to 1.07 for central events.

If our observed charge separation is dominated by the CME, ($\Delta H \times N_{part}$) should be roughly proportional to B_y^2. Based on the STAR measurements for Au+Au collisions at $\sqrt{s}$=200 GeV, projections of ($\Delta H^{\kappa=1.2} \times N_{part}$) for Ru+Ru and Zr+Zr collisions at $\sqrt{s}$=200 GeV as functions of centrality are shown in Figure 5-12 (a) assuming 1.2 x10^9 events. The systematic uncertainties in the projections are largely canceled out with the ΔH ratio of Ru+Ru over Zr+Zr, shown in Figure 5-12 (b).

Assuming 1.2 x10^9 events and combining events for 20-60% collisions, the ratio is 5σ above unity. With 4 x 10^8 events for each collision system, this reduces to a 3σ effect. If on the other hand our charge-separation observable is driven by collective flow, the ΔH ratio should closely follow the v_2 or eccentricity ratio, depicted by the blue curve in the panel (b). The ratio of the initial eccentricity comes from the Monte Carlo Glauber simulation, and it is highly consistent with unity for peripheral events and dropping below unity for central collisions owing to the deformation of the Zr nucleus. Since this ratio either stays unity or falls in the opposite direction to the CME-signal ratio, these isobaric collisions will provide a unique test with which to pin down the underlying physics mechanism driving the observed charge separation.

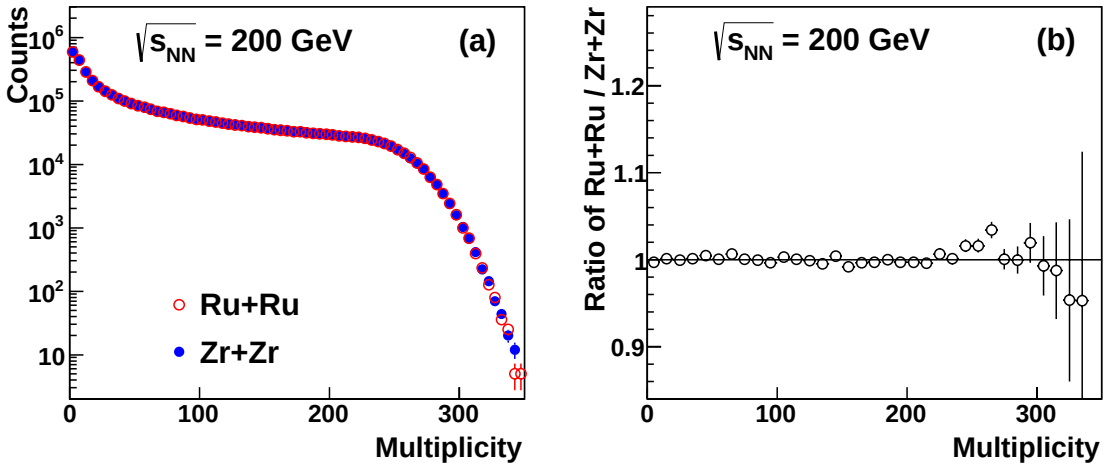

Figure 5-10 The Monte Carlo Glauber simulation of multiplicity for $_{44}{}^{96}$Ru + $_{44}{}^{96}$Ru and $_{40}{}^{96}$Zr+$_{40}{}^{96}$Zr at 200 GeV (a) and the ratio (b).

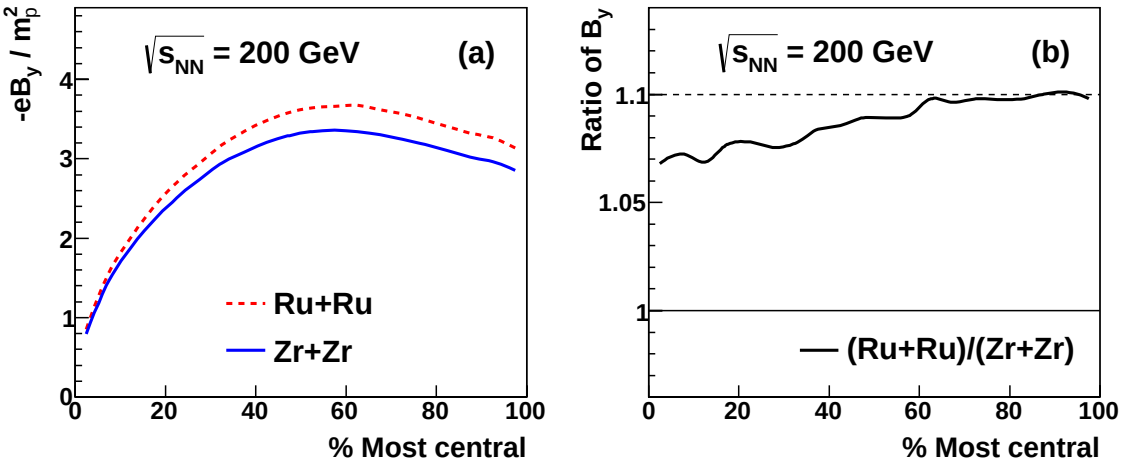

Figure 5-11 Theoretical calculations of the initial magnetic field for $_{44}{}^{96}$Ru + $_{44}{}^{96}$Ru and $_{40}{}^{96}$Zr+$_{40}{}^{96}$Zr at 200 GeV (a) and the ratio (b) vs centrality [79].

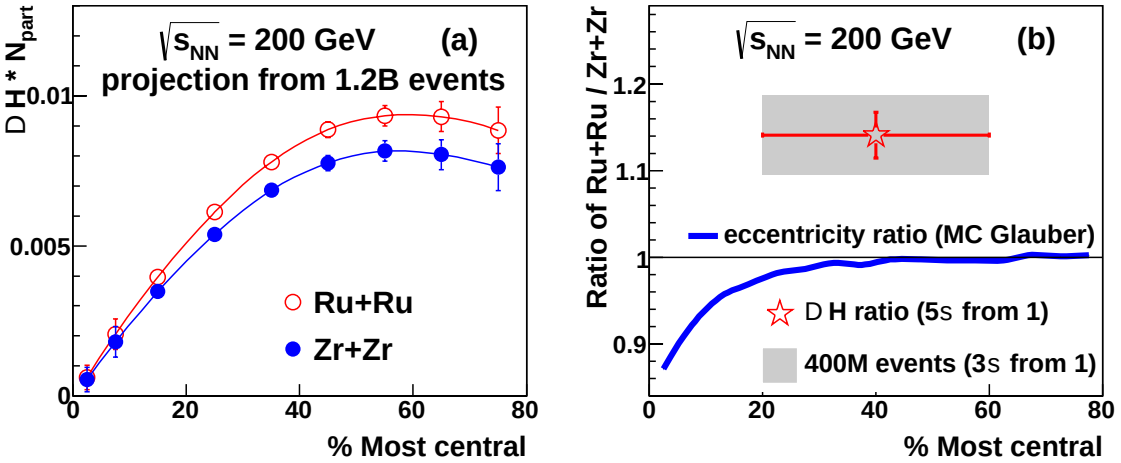

Figure 5-12: Projections of $\Delta H^{\kappa=1.2}$ x N_{part} for $_{44}{}^{96}$Ru + $_{44}{}^{96}$Ru and $_{40}{}^{96}$Zr+$_{40}{}^{96}$Zr at 200 GeV (a) and the ratio (b) vs centrality. The ratio of the initial eccentricity from the Monte Carlo Glauber simulation is also shown in the panel (b).

Observable	$_{44}{}^{96}$Ru + $_{44}{}^{96}$Ru vs $_{40}{}^{96}$Zr + $_{40}{}^{96}$Zr
Flow	≤
CME	>
CMW	>
CVE	=

Table 5-2 The expected relationship between Ru+Ru and Zr+Zr in terms of experimental observables for elliptic flow, CME, CMW and CVE.

Table 5-2 lists the expected relationship between Ru+Ru and Zr+Zr in terms of experimental observables for elliptic flow, CME, CMW and CVE, assuming chiral effects are the dominant physics mechanisms for the corresponding observables. With this assumption for the CMW observable, we have carried out a 1.2B-event projection for the slope parameter, and estimate that the *r* ratio of Ru+Ru over Zr+Zr, to be 1.08±0.08 for 20-60% collisions, which is only a 1σ effect. The CVE does not explicitly depend on the magnetic field, so to 1st-order we expect the same amount of baryon-number

separation for Ru+Ru and Zr+Zr. However, there could be a positive correlation between the charge and baryon-number asymmetries, but further input from theorists is required.

6 Detector Upgrades Relevant to the BUR

6.1 Heavy Flavor performance and future running schemes

In run-14 the HFT data were collected only when the ZDC rate was below ~40kHz to minimize LU rates and to reduce risk for damage of the PXL detector. This allowed to run HFT in a 'safe' mode and at the same time take advantage of the high luminosity in the beginning of a store.

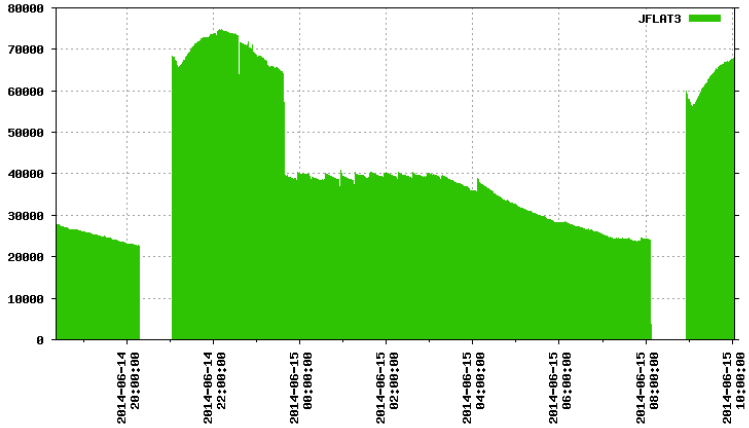

Figure 6-1: Typical delivered luminosity profile for STAR in Run14 Au+Au

For Run-16 the projected maximum luminosity are 1.3-1.5 times larger and implies that STAR cannot sample the full luminosity and at the same time collect re requested 2B minbias sample.

In the C-AD projection document several methods are indicated how to modify the delivered luminosity to experiments.

Several tools exist to adjust the instantaneous luminosity during a store, and create a desired time- dependent luminosity profile. These include:

- the selection of the initial β*,
- a change of β* during the store (as implemented in Run-14),
- a change of vertical separation at the interaction point (also implemented in Run-14), and changes in the cooling rate.

We assume that CA can deliver a flattened beam-profile e.g. as given below in the Figure 6-2, which show corrected ZDC rates i.e. luminosity assuming 10b cross section. The green is a scaled projection of stores delivered in run-14, and the red indicates that what can be delivered in beta* is changed from 1.2 early in the store to 0.5 late in store. It is quite likely that PXL can operate at these luminosities throughout the store, but requires a few tests that can be carried out during Run15.

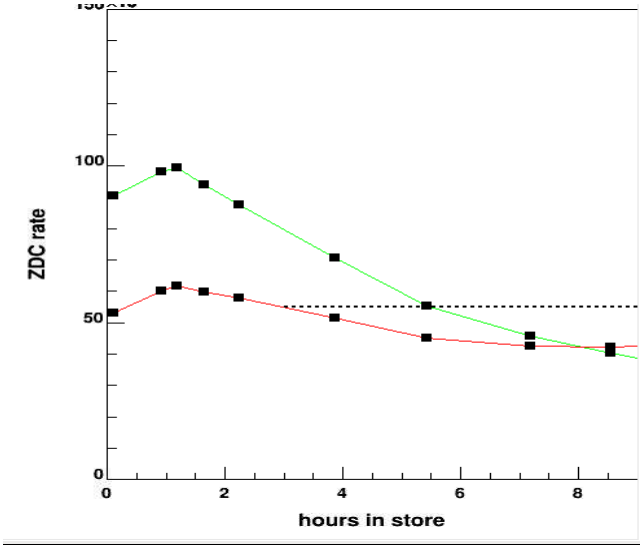

Figure 6-2: ZDC rates for requested beam profile. The green curve shows the scaled ZDC rate (luminosity for 10b cross section) as the expected maximum luminosity, and the red a luminosity profile with a dynamic beta*.

In the proposed scenario the delivered luminosity is 0.17 nb^{-1} per store. In the Run14 Au+Au at 200 GeV the average physics-on hours per day were 13.5 hours i.e. 94.5 per week. Thus RHIC can deliver ~94.5/9*0.17 ~ 1.8 nb^{-1}/week in this running mode. Even though the delivered luminosity is not the maximum that can be delivered, it still allows STAR to reach the proposed goals for both the minimum bias goals and the high luminosity goals.

6.2 Roman Pot performance and future running schemes

Based on our experience a request for data in pp Run 17 $\sqrt{s}$=500 GeV will be determined. The plan is to acquire more data for the Central Exclusive Production process in Run 17. Because of the higher momentum of the beams the invariant mass of the central system will be extended as well as the statistics of four-particle central state will be increased.

6.3 Near terms upgrades (2015-2020)

The STAR Collaboration has recently produced a road map for our future in the form of our decadal plan [80], eSTAR Letter of Intent [81], Beam Energy Scan Whitepaper [1] and pp/pA physics document [82]. We are fully committed to our priorities based on the scientific pillars of studying QGP properties, quantifying nucleon spin structure, searching for critical point in QCD phase diagram and exploring the high-density gluon field in nuclei. In this section, we provide additional details on a few near-term upgrades leading up to the second phase of Beam Energy Scan.

6.3.1 FMS Post-shower

Discussion contained in section 5.2.2.

6.3.2 STAR Inner TPC Sector Upgrade (iTPC)

We plan to upgrade the inner sectors of the STAR TPC (iTPC project) to increase the active pad coverage and optimize the pad size for the inner pad plane and to renew the inner sector wires. The upgrade will provide better momentum resolution, better *dE/dx* resolution, and most importantly it will

provide improved acceptance at high rapidity to $|\eta| < 1.7$ compared to the current TPC configuration of $|\eta| < \sim 1.0$. In the iTPC upgrade, we demonstrate that acceptance at high rapidity is a crucial part of STAR's future as we consider forward physics topics such as *pA*, *eA* and the proposed Phase-II of the Beam Energy Scan program. Unlike the outer TPC sectors, the current inner TPC pad row geometry does not provide hermetic coverage at all radii. The inner pads are 11.5 mm tall yet the spacing between rows is variable but always greater than 5 cm, resulting in "missing rows". Therefore, only 20% of the path length of a charged particles path traversing an inner sector of the TPC is sampled by the current padplane and electronics readout. With this proposal, we would like to increase the path length coverage in the inner sectors to 100%.

Future measurements, motivated by several open physics questions, will be greatly enhanced by the upgraded performance of the iTPC. Searching for the predicted critical point in the QCD phase diagram is one of the major scientific tasks in heavy ion physics. Thus the enhanced measurement capabilities of STAR after the iTPC upgrade are a vital part of the new BES-II effort. The iTPC upgrade extends the rapidity coverage by 50%, a major benefit for many analyses, especially fluctuations (Kurtosis) and baryon $v1$ measurements; it improves the 2nd-order event-plane resolution away from mid-rapidity by a factor of 2, greatly enhancing all elliptic flow measurements; and in the area of dielectron measurements it reduces hadron contamination and acceptance at low p_T as dominant sources of uncertainty (20%) down to much less than the expected statistical uncertainty (10%).

The participating institutions have clearly identified major expertise and strength for such a construction project: Mechanic design, strongback/padplane assembly (LBL), strongback production (UT Austin), electronics (BNL, CTU,NPI/Czech), Wire Chamber assembly (SDU, SINAP and USTC /China). A proposal has been submitted to BNL after STAR Collaboration review (https://drupal.star.bnl.gov/STAR/starnotes/public/sn0619).

6.3.3 Event Plane Detector

The most promising measurements in the search of the critical point and signatures for a phase transition rely either on a centrality measurement (e.g. higher moments of net-protons) or on an event plane (e.g. v1; v2, and azimuthal femtoscopy). Analysis of the BES I data showed that neither the centrality nor the event plane determination was optimized for this purpose. Fluctuation analyses are sensitive to physics correlations between the centrality determination using TPC tracks and the actual measurement itself. These correlations can be reduced by using distinct regions of the TPC for both measurements or by using different particle species. Both procedures are only an approximation to a TPC-independent centrality measurement and do not in practice exclude physics correlations.

Based on these physics requirements we list the essential specifications for the proposed Event Plane and centrality Detector (EPD) in the following:

- Large rapidity gap relative to the TPC to minimize non-flow effects and physics correlations
- Significant radial segmentation to reduce (EP) biases
- Large acceptance to maximize the EP resolution
- Symmetric in pseudo rapidity (east and west side) in order to determine an unbiased EP resolution and to measure as many particles as possible
- Fine granularity (single hit determination) for good EP and centrality resolution

On-going R&D is to support a future proposal for a new dedicated event plane and centrality detector in the forward directions of STAR for Beam Energy Scan (BES) phase II, which is anticipated for the years 2019-2020. The new detector will cover the pseudo-rapidity range between 1.8 and 5, with high radial and azimuthal segmentation. The current baseline detector design utilizes scintillators and silicon photomultipliers. Active participants are LBL, OSU, BNL, and KSU.

6.3.4 Forward Hadronic Calorimeter for event-by-event spectator measurement

A calorimeter is an essential tool for forward particle production because of the high energies and particle density involved. To date, RHIC experiments have had limited instrumentation for detection of particles produced in the forward direction. STAR has successfully implemented a forward meson spectrometer using lead-glass array as an electromagnetic calorimeter to detect forward pion0 and photon yields and correlations in p+p, p+A and d+Au collisions. There is an increasing demand of calorimeter performance with increasing luminosity, rare probes and high statistics. An additional hadronic calorimeter may be able to help us improve hadronic rejection in photon detection, determine longitudinal fluctuation by rapidity correlation of particles and energy deposit in calorimeter, and most importantly, detect spectator in an event-by-event basis for assessing the impact of stopping on Kurtosis analyses in future BES II program.

The E864 collaboration constructed a good calorimeter whose purpose was to detect hadrons [83]. Each cell of this calorimeter has cross sectional area of 10 cm^2 and a length of 117 cm. The showering material is lead. Energy deposition is measured by a 47 × 47 matrix of 1-mm diameter and 117-cm long scintillating fiber embedded in the lead. Scintillation light from a cell was focused through a light guide on to a photomultiplier tube with a 2-inch diameter photocathode. Cockcroft-Walton bases powered the photomultiplier tubes. The E864 calorimeter was originally repurposed to detect spectator protons in d+Au collisions at RHIC by the PHENIX and PHOBOS collaborations. A second repurposing was done at IP2 by the AnDY collaboration. This third implementation was a Research and Development project whose initial purpose was to establish if increased transverse resolution of the calorimeter readout [so-called pixelization] would measure hadronic shower as well as allow for reconstructing neutral pions to high energies. Pixelizing the existing E864 calorimeter into 3.3-cm cells does allow reconstruction of neutral pions to high energy. The FHC was found to be stable through ^{3}He+Au operations, despite regular and significant injection flashes due to the beam orbits as required to collide the beams. The electromagnetic response of the FHC is comparable to a lead-glass calorimeter of comparable (but somewhat coarser) cell size. Radiation hardness of the E864 calorimeter is superior to lead glass, because it samples showers using scintillating fibers. It remains to be worked out how this setup can be used in the future runs including BES II.

6.3.5 Endcap TOF (CBM TOF)

It has become clear that enhanced particle identification behind the extended tracking by iTPC upgrade will greatly expand STAR's physics program in BES II and beyond. The addition of an endcap TOF virtually increases the excellent particle identification at STAR midrapidity by a factor of two. Over the last two years, we propose a several-year program to develop two end-cap annuli of MRPC Time-of-Flight detectors suitable for eSTAR. The effort took a dramatic turn recently with the possibility of using a small fraction of CBM TOF (10%) installed in STAR endcap for BES II and as

test ground for future CBM in FAIR. We have been in the discussion of a plan to carry out test in run 16 and run17 before a complete endcap TOF installation for BES II.

7 BUR charges from ALD

From: Mueller, Berndt

Sent: Tuesday, March 31, 2015 9:58 PM

To: James Nagle; Morrison, David; Xu, Zhangbu; Ernst Sichtermann

Cc: Roser, Thomas; Fischer, Wolfram; Dunlop, James C

Subject: BURs for Run 16 & 17

Dear RHIC Spokespersons:

I am writing again to update my request for the beam use requests for the coming RHIC runs.

In consultation with the Office of Nuclear Physics we have decided to make a change to the future RHIC run schedule. Specifically, we now plan to run RHIC in both FY16 and FY17, followed by one year (FY18) without a RHIC run during which the low energy RHIC electron cooling (LEReC) system will be installed. The high statistics Beam Energy Scan II is then planned for the years FY19 and FY20. The modified plan will allow for a less aggressive schedule of the LEReC project. It will also relax the conflict between the heavy ion and spin physics programs of RHIC that remained unresolved at last year's PAC meeting.

I request that you submit the annual beam use requests by May 19, 2015. The BURs should be for a 22-week RHIC run in FY16, and either a 15-week or a 22-week RHIC run in FY17.

I also ask the STAR Collaboration to present the iTPC proposal to the PAC and to provide an update on experimental efforts aimed at exploring possible phenomenological manifestations of the chiral magnetic effect.

Both collaborations should present a tentative schedule for the release of results from the data taken in runs 13 and 14 (p+p, Au+Au 15, Au+Au 200, 3He+Au).

Thanks, Berndt

References

[1] STAR Beam Energy Scan II: Studying the Phase Diagram of QCD Matter at RHIC https://drupal.star.bnl.gov/STAR/starnotes/public/sn0598
[2] STAR Collaboration, Phys. Rev. Lett. 113 (2014) 142301
[3] STAR Collaboration, Phys. Rev. C 90 (2014) 24906
[4] STAR Collaboration, Phys. Lett. B 739 (2014) 180
[5] STAR Collaboration, Phys. Lett. B 735 (2014) 127
[6] STAR Collaboration, Phys. Rev. Lett. 113 (2014) 22301
[7] STAR Collaboration, Phys. Rev. C 90 (2014) 64904
[8] STAR Collaboration, e-Print Archives (1501.05341)
[9] STAR Collaboration, e-Print Archives (1503.04217)
[10] STAR Collaboration, e-Print Archives (1504.01317)
[11] STAR Collaboration, e-Print Archives (1410.3524)
[12] STAR Collaboration, Phys. Lett. B 743 (2015) 333
[13] STAR Collaboration, e-Print Archives (1502.07652)
[14] STAR Collaboration, Phys. Rev. Lett. 113 (2014) 92301
[15] STAR Collaboration, e-Print Archives (1410.5375)
[16] STAR Collaboration, Phys. Rev. C 91 (2015) 34905
[17] STAR Collaboration, Phys. Rev. Lett. 114 (2015) 22301
[18] STAR Collaboration, e-Print Archives (1504.00415)
[19] B. Abelev et al. (STAR Collaboration) Phys. Rev. Lett. 99 (2007) 142003; L. Adamczyk et al. (STAR Collaboration) Phys. Rev. D 86 (2012) 032006; A. Adare et al. (STAR Collaboration) arXiv:1312.1995.
[20] K. Kanazawa and Y. Koike. Phys. Lett. B720 (2013) 161.
[21] M. Mondal for the STAR Collaboration, PoS DIS 2014, 216 (2014).
[22] E.R. Nocera *et al.* [NNPDF Collaboration], Nucl. Phys. B **887**, 276 (2014)
[23] W.C. Chang and J.C. Peng, Prog.Part.Nucl.Phys. **79** (2014) 95; arXiv: 1406.1260.
[24] D. Kharzeev, Phys. Lett. B 633, 260 (2006) [hep-ph/0406125].
[25] D. Kharzeev and A. Zhitnitsky, Nucl. Phys. A 797,67 (2007).
[26] D. E. Kharzeev, L. D. McLerran and H. J. Warringa, Nucl. Phys. A 803, 227 (2008).
[27] S. A. Voloshin, Phys. Rev. C 70, 057901 (2004) [hep-ph/0406311].
[28] B. I. Abelev et al. (STAR Collaboration), Phys. Rev. Lett. 103, 251601 (2009).
[29] B. I. Abelev et al. (STAR Collaboration), Phys. Rev. C 81, 54908 (2010).
[30] L. Adamczyk et al. (STAR Collaboration), Phys. Rev. C 88 (2013) 064911.
[31] L. Adamczyk et al. (STAR Collaboration), Phys. Rev. Lett. 113 (2014) 052302.
[32] B. I. Abelev et al.[ALICE Collaboration], Phys. Rev. Lett. 110 021301 (2013).
[33] A. Bzdak, V. Koch and J. Liao, Lect. Notes Phys. 871 (2013) 503.
[34] S. Voloshin, Phys. Rev. Lett. 105 (2010) 172301.
[35] Gang Wang (STAR Collaboration), Nucl. Phys A 904 (2013) 248c.
[36] D. T. Son and A. R. Zhitnitsky, Phys. Rev. D 70, 074018 (2004).
[37] M. A. Metlitski and A. R. Zhitnitsky, Phys. Rev. D 72, 045011 (2005).
[38] Y. Burnier, D. Kharzeev, J. Liao and H. Yee, Phys. Rev. Lett. 107 (2011) 052303
[39] L. Adamczyk et al. (STAR Collaboration), submitted to PRL [arXiv:1504.02175].
[40] S.A. Bass et al., Prog. Part. Nucl. Phys. 41, 225 (1998); M. Bleicher et al., J. Phys. G: Nucl. Part. Phys. 25, 1859 (1999).
[41] Y. Burnier, D.E. Kharzeev, J. Liao, H.-U. Yee, arXiv: 1208.2537 (2012); private communication.
[42] Z.W. Lin and C.M. Ko, Phys. Rev. C 65, 034904 (2002); L.-W. Chen, C.-M. Ko, J. Phys. G 31, S49 (2005).

[43] Q.-Y. Shou (STAR Collaboration), Nucl. Phys. A 931 (2014) 758.
[44] D. E. Kharzeev and D. T. Son, Phys. Rev. Lett. 106 (2011) 062301.
[45] Feng Zhao (STAR Collaboration), Nucl. Phys. A 931 (2014) 746.
[46] L. Adamczyk et al., (STAR Collaboration), Phys. Rev. Lett.112, 162301 (2014).
[47] S. A. Bass *et al*., Prog. Part. Nucl. Phys. **41**, 255 (1998);
M. Bleicher *et al*., J. Phys. G **25**, 1859 (1999).
[48] W. Cassing *et al*., arXiv:1408.4313.
[49] STAR Collaboration, Phys. Rev. Lett. **112** (2014) 32302
[50] X. F. Luo, (STAR Collaboration), PoS(CPOD2014)019, arXiv:1503.02558.
[51] M. A. Stephanov, Phys. Rev. Lett. 107, 052301 (2011).
[52] X.-N.Wang, Z. Huang and I. Sarcevic, Phys. Rev. Lett. 77, 231 (1996).
[53] L. Cormell and J. F. Owens, Phys. Rev. D 22, 1609 (1980) and references therin.
[54] A. Kulesza, G. Sterman, and W. Vogelsang, Nucl. Phys. A 721, 591 (2003).
[55] P. Aurenche *et al.*, Phys. Rev. D 73, 094007 (2006).
[56] T. Renk and K. Eskola, Phys. Rev. C 75, 054910 (2007).
[57] Phys. Rev. Lett. 98:172301 (2007)
[58] Phys. Rev. D 79, 034009 (2009); **arXiv:1410.3959**
[59] K. Burke et al, [JET Collaboration], Phys. Rev. C 90 1 (2014) 014909.
[60] Antreasyan et al., Phys. Rev. D 19 (1979) 764; Cronin et al., Phys. Rev. D 11 (1975) 3105;
Straub et al., Phys. Rev. Lett 68 (1992) 452.
[61] H1 Collaboration, F. Aaron *et al.*. JHEP, 01:109, 2010. arXiv:0911.0884.
[62] a case for run16 pp510 (supplementary material):
https://drupal.star.bnl.gov/STAR/starnotes/private/psn0617
[63] A. V. Efremov and O. V. Teryaev, Sov. J. Nucl. Phys. 36, 140 (1982) [Yad. Fiz. 36, 242 (1982)];
Phys. Lett. B 150, 383 (1985).
J.-W. Qiu and G. F. Sterman, Phys. Rev. Lett. 67, 2264 (1991); Nucl. Phys. B 378, 52 (1992);
Phys. Rev. D 59, 014004 (1999)
[64] P. Sun and F. Yuan, Phys. Rev. D. 88 (2013) 114012
[65] P. Sun, J. Isaacson, C.-P.Yuan and F. Yuan aeXiv:1406.3073
[66] M.G. Echevarria, A. Idilbi, Z.-B. Kang and I. Vitev,
Phys. Rev. D 89 (2014) 074013, arXiv:1401.5078
[67] J. Collins, arXiv:1409.5408; J. Collins and T. Rogers, Phys.Rev. D91 (2015) 7, 074020,
arXiv:1412:3820; J. Collins, Talk at DIS 2015,
https://indico.cern.ch/event/341292/session/16/contribution/33/material/slides/0.pdf
[68] Z.-B. Kang and J.-W. Qiu, Phys.Rev.D81:054020,2010, arXiv:0912.1319
[69] Z.-B. Kang and J.-W. Qiu, Phys. Rev. Lett. 103 (2009) 172001, arXiv:0903.3629
[70] A. Metz and J. Zhou, Phys. Lett. B 700 (2011) 11, arXiv:1006.3097
[71] S. Fazio, talk at DIS-2014,
http://indico.cern.ch/event/258017/session/11/contribution/219/material/slides/0.pptx
72 E.A. Hawker et al., Phys. Rev. Lett. 80, 3715 (1998)
[73] Z.-B. Kang and J.-W. Qiu, Phys.Rev.D81:054020,2010, arXiv:0912.1319
[74] L. Gamberg, Z.-B. Kang, and A. Prokudin, Phys. Rev. Lett. 110, 232301 (2013).
[75] L.C. Bland et al. [AnDY Collaboration], arXiv:1304.1454
[76] S. Voloshin, Phys. Rev. Lett. 105 (2010) 172301.
[77] B.B. Back et al., Phys. Rev. C 65, 031901(R) (2002);
K. Adcox et al., Phys. Rev. Lett 86, 3500 (2001); I.G. Bearden et al., Phys. Lett. B 523, 227 (2001);
J. Adams et al. (STAR Collaboration), nucl-ex/0311017.
[78] W. -T. Deng and X. -G. Huang, Phys. Rev. C 85 (2012) 044907;

W. -T. Deng and X. -G. Huang, Phys. Lett. B 742 (2015) 296; private communication.

[79] John Bloczynski, Xu-Guang Huang, Xilin Zhang, Jinfeng Liao, Phys. Lett. B 718, 1529(2013)

[80] STAR Decadal Plan (December 2010)
http://www.bnl.gov/npp/docs/STAR_Decadal_Plan_Final%5b1%5d.pdf

[81] eSTAR Letter of Intent
https://drupal.star.bnl.gov/STAR/starnotes/public/sn0592

[82] A polarized p+p and p+A program for the next years
https://drupal.star.bnl.gov/STAR/starnotes/public/sn0605

[83] T. A. Armstrong et al., Nucl. Inst. Meth. A 406 (1998) 227.